MATCHED FIELD PROCESSING BASED GEO-ACOUSTIC INVERSION IN SHALLOW WATER

A Thesis
Presented to
The Academic Faculty

by

Lin Wan

In Partial Fulfillment
of the Requirements for the Degree
Doctor of Philosophy in the
School of Mechanical Engineering

Georgia Institute of Technology
December 2010

MATCHED FIELD PROCESSING BASED GEO-ACOUSTIC INVERSION IN SHALLOW WATER

Approved by:

Dr. Ji-Xun Zhou, Co-advisor
School of Mechanical Engineering
Georgia Institute of Technology

Dr. Peter H. Rogers, Co-advisor
School of Mechanical Engineering
Georgia Institute of Technology

Dr. Jianmin Qu
School of Mechanical Engineering
Georgia Institute of Technology

Dr. Laurence J. Jacobs
School of Civil Engineeing
Georgia Institute of Technology

Dr. Mohsen Badiey
College of Earth, Ocean, & Environment
University of Delaware

Date Approved: July 1, 2010

To my parents and my wife
for their love, support and encouragement

ACKNOWLEDGEMENTS

First of all, I would like to express my sincere gratitude to my advisors, Dr. Ji-Xun Zhou and Dr. Peter H. Rogers, for their guidance, patience, encouragement and support through my Ph.D. study, which has been a life changing experience. They introduced me to the world of shallow water acoustics and showed me how to be a great scientist with their expertise and scientific attitude. It is my great honor to be their student. Their constant trust and invaluable suggestions about my academic research will be forever highly appreciated from the bottom of my heart.

I am also grateful to my reading committee members: Dr. Jianmin Qu, Dr. Laurence J. Jacobs and Dr. Mohsen Badiey for their effort in reviewing this work and their valuable input to this thesis.

This work was sponsored by the Office of Naval Research, including an Office of Naval Research (ONR) Ocean Acoustics Graduate Traineeship Award. I would like to express my great appreciation to Dr. Ellen Livingston (ONR) and Dr. Benjamin Reeder (ONR). As an ONR graduate trainee in the past six years, I benefitted a lot from their support, and helpful comments.

I would like to thank the crew abroad the R/V Sharp, especially the science crew: Dr. Mohsen Badiey, Dr. Boris Katsnelson (Voronezh University, Russia), Dr. Jie Yang (University of Washington), Jing Luo (University of Delaware), Georges Dossot (University of Rhode Island), Steve Crocker (URI), Lauren Brown (UD), Jeremie Largeaud (UD), Jakob Siegel (UD), for their help during the Shallow Water ’06 experiment.

I wish a special thanks to Dr. David P. Knobles (University of Texas at Austin) for providing the data of two SWAMI arrays and insightful suggestions on our collaborative spatial coherence paper in 2009. I also thank Dr. Aijun Song (UD) and Arthur Newhall (Woods Hole Oceanographic Institution) for providing acoustic data, which are used in this thesis.

I want to give my thanks to my colleagues and officemates at Georgia Tech: Dr. Jie Yang, Dr. Yunhyeok Im, Dr. Peter Cameron, Kenneth Marek and Zohra Ouchiha for their kind help.

Finally, I would like to express my great appreciation to my parents and my wife for their love, understanding and encouragement. Without their spiritual support throughout the years at Georgia Tech, I would not be here.

TABLE OF CONTENTS

LIST OF TABLES

LIST OF FIGURES

LIST OF SYMBOLS

α_b	Seabed attenuation
c_b	Seabed sound speed
ρ_b	Seabed density
f	Frequency
T	Temperature
S	Salinity
M_Z	Mean grain size
p	Acoustic pressure
ρ	Density
c	Sound speed
z_s	Source depth
$k_{n,c}$	Complex wave number of nth mode
$H_0^{(1)}$	Zero order Hankel function of the first kind
k_n	Horizontal wave number of nth mode
β_n	Modal attenuation coefficient of nth mode
V_g^n	Group velocity of nth mode
V_p^n	Phase velocity of nth mode
R_{n1}	Modal amplitude ratio of the nth mode to the first mode
S_n	Cycle distance of the nth normal mode
Ψ_n	Mode depth function of nth normal mode

r	Range
Δr	Range step
C	Cross-spectral density matrix
τ	Time delay
λ	Wavelength
$\rho_{vertical}$	Vertical coherence length
$\rho_{longitudinal}$	Longitudinal horizontal coherence length
θ_{eff}	Effective grazing angle
Q	Bottom reflection loss factor

LIST OF ABBREVIATIONS

3D	Three dimensional
AOK TFR	Adaptive Optimal-Kernel Time-Frequency Representation
BP	Bubble Pulses
CSDM	Cross-Spectral Density Matrix
CSS	Combustive Sound Source
CTD	Conductivity-Temperature-Depth
GA	Genetic Algorithm
GMT	Greenwich Mean Time
HLA	Horizontal Line Array
KRAKEN	normal mode program
LF	Low frequency
MFP	Matched Field Processing
PE	Parabolic Equation
RAM	Range-dependent Acoustic Model
RD	Receiver Depth
RV	Research Vessel
SD	Source Depth
SNR	Signal to Noise Ratio
SSP	Sound Speed Profile
SVD	Singular Value Decomposition
SW	Shock Wave
SW ’06	Shallow Water '06 experiment

TL	Transmission Loss
UTC	Coordinated Universal Time
VLA	Vertical Line Array
YS ’96	Yellow Sea '96 experiment

SUMMARY

Shallow water acoustics is one of the most challenging areas of underwater acoustics; it deals with strong sea bottom and surface interactions, multipath propagation, and it often involves complex variability in the water column. The sea bottom is the dominant environmental influence in shallow water. An accurate solution to the Helmholtz equation in a shallow water waveguide requires accurate seabed acoustic parameters (including seabed sound speed and attenuation) to define the bottom boundary condition. Direct measurement of these bottom acoustic parameters is excessively time consuming, expensive, and spatially limited. Thus, inverted geo-acoustic parameters from acoustic field measurements are desirable.

Because of the lack of convincing experimental data, the frequency dependence of attenuation in sandy bottoms at low frequencies is still an open question in the ocean acoustics community. In this thesis, geo-acoustic parameters are inverted by matching different characteristics of a measured sound field with those of a simulated sound field. The inverted seabed acoustic parameters are obtained from long range broadband acoustic measurements in the Yellow Sea ’96 experiment and the Shallow Water ’06 experiment using the data-derived mode shape, measured modal attenuation coefficients, measured modal arrival times, measured modal amplitude ratios, measured spatial coherence, and transmission loss data. These inverted results can be used to test the validity of many seabed geo-acoustic models (including Hamilton model and Biot-Stoll model) in sandy bottoms at low frequencies. Based on the experimental results in this thesis, the non-linear frequency dependence of seabed effective attenuation is justified.

CHAPTER 1

INTRODUCTION

1.1 Background and Motivation

Around 70% of the Earth's surface is covered by ocean. Sound waves can travel through the ocean over a distance of many hundreds of kilometers. Because of its relative ease of propagation, underwater sound has been applied to a variety of purposes in the use and exploration of the ocean.

Shallow water acoustics is one of the most challenging areas of underwater acoustics. It is a stimulating and exciting discipline for physicists, oceanographers, and underwater acousticians. Shallow water environments are found on the continental shelf, a region which is important to human activities such as shipping, fishing, oil production etc. In shallow water, with boundaries framed by the surface and bottom, the typical depth-to-wavelength ratio is about 10–100. That ratio makes the propagation of shallow water acoustic waves analogous to electromagnetic propagation in a dielectric waveguide (Kuperman and Lynch, 2004). In contrast to deep-water propagation, where purely waterborne paths predominate, shallow water acoustics deals with strong sea bottom and surface interactions and multipath propagation, and it often involves complex variability in the water column (Zhang and Zhou, 1997). Therefore, it is difficult to predict sound propagation in shallow water, which is an amazingly complex waveguide environment (Frisk, 1991).

Differences between one shallow-water region and another are primarily driven by differences in the composition of the sea bottom. Thus the sea bottom is the dominant environmental influence in shallow water. An accurate solution to the Helmholtz

equation in a shallow water waveguide requires accurate seabed acoustic parameters (including sediment sound speed, density, and attenuation) to define the bottom boundary condition. Direct measurement of these bottom properties, e.g. coring, is excessively time consuming, expensive and spatially limited. The small amount of sound attenuation in sediments at low frequencies precludes laboratory measurement, because the distances required to achieve a detectable amount of sound attenuation are at least hundreds or thousands of meters. That is why there are no direct measurements of attenuation below 1000 Hz. Thus, inversion methods based on acoustic field measurements which can rapidly and accurately estimate the bottom properties are very desirable (Tolstoy, 2002).

In the sections which follow, background information about geo-acoustic modeling of the sea bottom and matched field processing is presented.

1.2 Introduction to Geo-acoustic modeling of the Sea Bottom

Geo-acoustic models of the sea floor are basic to underwater acoustics and to marine geological and geophysical study of the earth's crust. A "geo-acoustic model" is defined as a model of the sea floor with emphasis on measured, extrapolated, and predicted values of the properties important in underwater acoustics and the aspects of geophysics involving sound transmission (Hamilton, 1980).

The geo-acoustic properties (Hamilton, 1980) are (1) bottom type; (2) thickness and shape of the bottom layers; (3) compressional wave (sound) speed and attenuation; (4) Shear wave speed and attenuation; (5) density. Among those properties, compressional sound velocity and attenuation play the dominant role in a shallow water environment (Stoll, 1994; Zhou *et al.,* 2009). The frequency and depth dependence of these parameters are of importance in any geo-acoustic model.

The most well-known geo-acoustic models of sea bottom are the Hamilton visco-elastic model (Hamilton, 1980) and the Biot-Stoll poro-elastic model (Biot, 1956[1,2], 1962; Stoll, 1985).

Hamilton classified the sediments in continental zones into nine types shown in Table 1.1. In his model, the geo-acoustic and geophysical properties such as porosity, permeability and grain size of the sediments are empirically related. His model suggests that the sound speed is approximately independent of frequency, and the attenuation increases linearly with frequency over the full frequency range. The Hamilton model shows a good agreement with experimental data at high frequencies or for finer-grained bottom with a high porosity.

In the Biot-Stoll model, the sediment's geo-acoustic properties and geophysical properties are related on the basis of physical principles. Several representative data sets for Biot geophysical parameters in sandy bottoms are summarized by Zhou *et al.* (2009) and listed in Table 1.2. TCCD was used by Tattersall *et al.,* (1993)*;* TY was used by Turgut and Yamamoto (1990); WJTTS was used by Williams *et al.*, (2002); Historical was used by Stoll (1998). Based on those Biot geophysical parameters, the Biot-Stoll model predicts that the sound speed should exhibit a strong non-linear dispersion and the acoustic attenuation should exhibit a non-linear frequency dependence, particularity in sandy and silty bottoms at low frequency (Biot, 1956, 1562; Stoll, 1977, 1980, 1985).

Because of a lack of convincing experimental data to confirm the validity of either the Hamilton model or the Biot-Stoll model in sandy bottoms at low frequencies, the debate on the sound speed dispersion and the frequency dependence of sound attenuation in the seabed has persisted for decades (Zhou *et al.*, 2009).

Table 1.1 Continental terrace environments and their properties (Hamilton and Bachman, 1982)

Sediment type	Mean grain size (mm)	Density (g/cm^3)	Porosity (%)	Sound speed ratio (compressional)
Coarse sand	0.5285	2.034	38.6	1.201
Fine sand	0.1638	1.962	44.5	1.152
Very fine sand	0.0988	1.878	48.5	1.120
Silty sand	0.0529	1.783	54.2	1.086
Sandy silt	0.0340	1.769	54.7	1.076
Silt	0.0237	1.740	56.2	1.057
Sand-silt-clay	0.0177	1.575	66.3	1.036
Clayey silt	0.0071	1.489	71.6	1.012
Silty clay	0.0022	1.480	73.0	0.990

Table 1.2 Input parameters to Biot model (Zhou *et al.*, 2009).

Symbols	Units	TCCD	TY	Historical	WJTTS
			Bulk properties		
(1) Porosity, β		0.43	0.44	0.36–0.47	0.385(0.415)
(2) Grain density, ρ_s	(kg/m^3)	2650	2650	2650	2690
(3) Fluid density, ρ_f	(kg/m^3)	1024	1000	1000	1023
(4) Grain bulk modulus, K_s	(Pa)	3.6×10^{10}	3.6×10^{10}	$(3.6–4.0)\times10^{10}$	3.2×10^{10}
(5) Fluid bulk modulus, K_f	(Pa)	2.38×10^{10}	2.3×10^{9}	$(2.0–2.3)\times10^{9}$	2.395×10^{9}
			Fluid motion		
(6) Viscosity, η	kg/m s	0.001 01	0.001	0.001	0.001 05
(7) Permeability, κ_s	(m^2)	1.25×10^{-11}	1.75×10^{-11}	$(0.65–10.0)\times10^{-11}$	2.50×10^{-11}
(8) Pore size, a	(m)	3.0×10^{-5}	5.2×10^{-5}	$(1.00–5.00)\times10^{-5}$	
(9) Tortuosity of sediment, α_0		1.75	1.25	1.00–1.25	1.35 (1.12)
			Frame response		
(10) Frame shear modulus, $\mu0$	(Pa)	5.0×10^{7}	2.4×10^{7}	$(2.61–11.9)\times10^{7}$	2.92×10^{7}
(11) Shear log decrement, δ_s		0.02	0.0477	0.00–0.15	0.0616
(12) Frame bulk modulus, K_0	(Pa)	5.0×10^{7}	5.2×10^{7}	$(4.36–43.6)\times10^{7}$	4.36×10^{7}
(13) Bulk log decrement, δ_b		0.02	0.0477	0.00–0.15	0.0477

1.3 Introduction to Matched Field Processing

In recent years, a signal processing technique known as matched-field processing (MFP) has been applied to obtaining shallow water bottom properties by inversion. MFP involves comparing measured acoustic-array data with model predictions for such data. It is assumed that the 'best' fit should correspond to the 'truest' model, where 'best' fit is usually defined as occurring at the minimum value of some cost functions measuring the discrepancy between the measured and modeled acoustic fields (Tolstoy, 2000). Figure 1.1 illustrates the typical MFP steps used when trying to estimate seabed sound speed and attenuation. There are generally four components to MFP: (1) Measured acoustic array data obtained from at-sea experiments. A detailed description of at-sea experiments used in this research will be given in Chapter 2. (2) A sound propagation model used to generate simulated acoustic data. Two sound propagation modeling methods (a normal mode method and a parabolic equation method) are used in this thesis and are presented in Chapter 3. (3) A cost function used to calculate the difference between the measured and modeled acoustic field. (4) An efficient search algorithm for searching the model parameter space.

1.3.1 Cost Function

MFP requires a suitable cost function quantifying the discrepancy between the measured and modeled acoustic fields. The minimum value of the cost function indicates a good match between the data and the model. It can be found by examining graphic 'misfit surfaces', showing a collection of cost function values. The red region on the misfit surface in Fig. 1.1 indicates the lowest value of cost function.

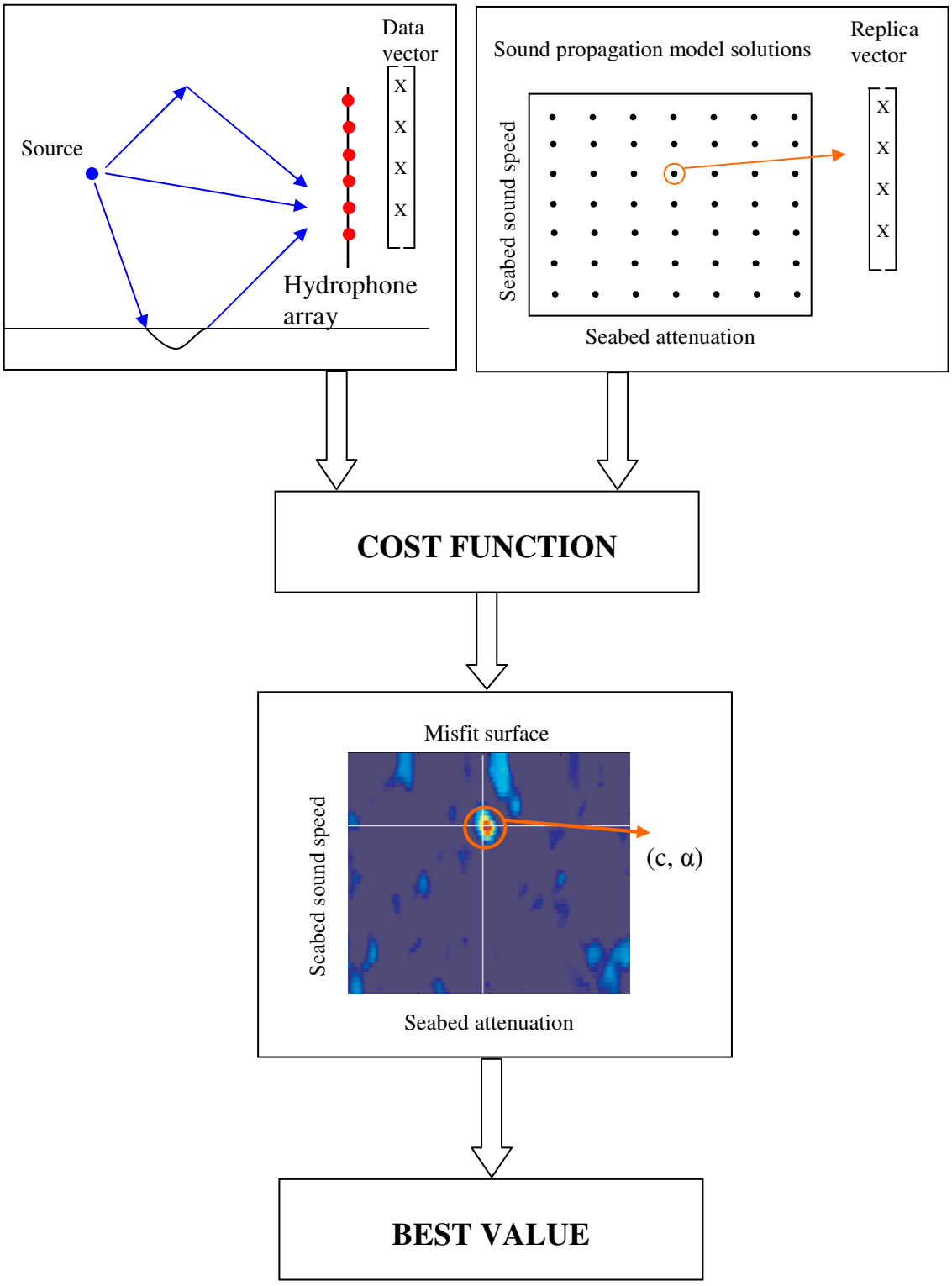

Figure 1.1 Typical MFP steps used when trying to estimate seabed sound speed and attenuation

Many different characteristics of the acoustic field can be used to construct a cost function. The complex sound pressures of the acoustic fields on an array of hydrophones are the most frequently used (Lindsay *et al.,* 1993; Li *et al.,* 2004; Huang, *et al.,* 2008). Numerous other characteristics of the sound field have also been applied such as normal mode depth functions (Hursky *et al.,* 2001; Wan *et al.,* 2006, 2010), modal arrival times (Zhou 1985, 1987; Potty *et al.,* 2000, 2003.; Peng *et al.,* 2004), Transmission Loss (Zhou 1985, 1987; Peng *et al.,* 2004; Wan *et al.,* 2006, 2010), broadband signal waveform (Li *et al.,* 2000, Knobles *et al.,* 1996), vertical coherence of propagation and reverberation (Zhou *et al.,* 2004).

1.3.2 Optimization Algorithms

Geo-acoustic inversion is an optimization problem: search the model parameter space to find the bottom parameters that minimize the cost function. In order to perform an effective search and to reduce the computational load, both local optimization methods (Gauss-Newton method and Levenberg-Marquardt algorithm) and global optimization methods (Simulated Annealing and Genetic Algorithms) have been used in the estimation of sea bottom properties (Gauss-Newton: Gerstoft, 1995; Levenberg-Marquardt: Neilsen*.,* 2000; Simulated Annealing: Lindsay *et al.,* 1993; Genetic Algorithms: Gerstoft, 1994, 1995; Siderius *et al.,* 1998 and Taroudakis, *et al* 1997, 1998, 2000). In this thesis, Genetic Algorithms are used in the multiple parameter geo-acoustic inversion problems.

A genetic algorithm (GA) is a biologically motivated approach to optimization (Goldberg, 1989). A simple GA consists of three operations: Selection, Genetic Operation, and Replacement. A typical GA cycle is shown in Fig. 1.2. A simple GA starts with an initial population, which was randomly generated. The population comprises a

group of chromosomes, from which candidates can be selected for the solution of a problem (Tang, 1996). The fitness of each chromosome is obtained by calculating the value of the cost function for that chromosome. Then the parents are selected from the population based on the fitness of the individuals. The parents are combined in pairs to generate the offspring by the genetic operations, which are traditionally crossover and mutation operations. Finally, the offspring replace part of the current population to get a more fit population. Such a GA cycle is repeated until a desired termination criterion is reached. For example, the GA cycle stops if there is no improvement in the fitness for a predefined number of generations. In the final population, the best member can become a highly evolved solution to the problem (Tang, 1996).

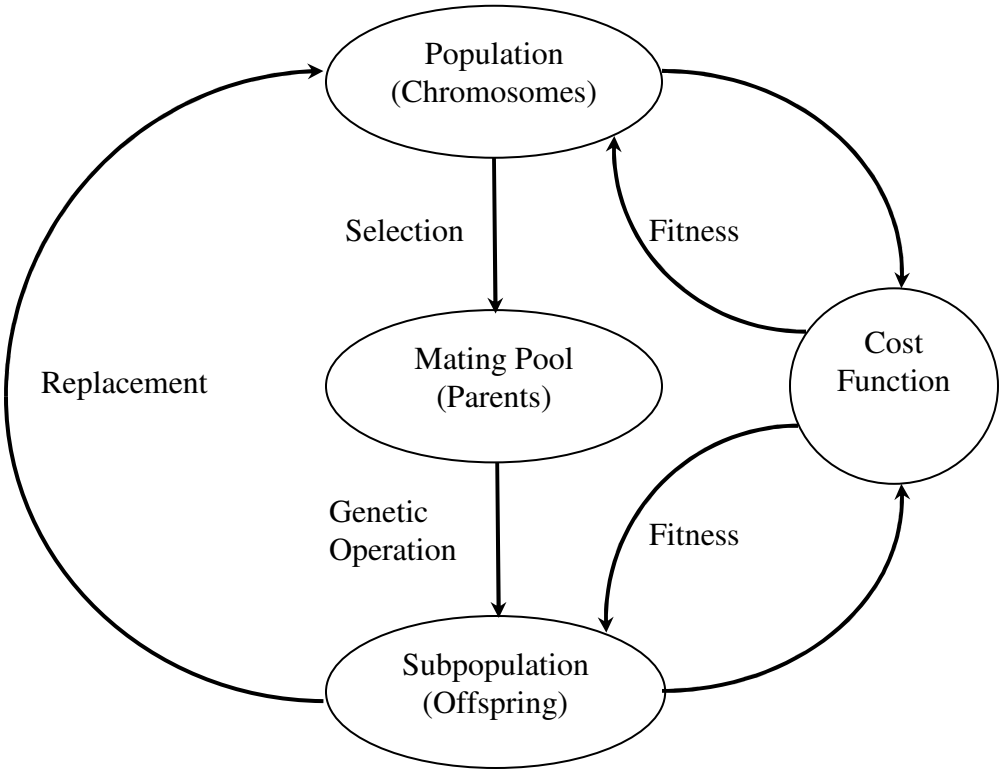

Figure 1.2 A typical genetic algorithm cycle (Tang, 1996)

1.4 Objectives

When low-frequency sound of sufficient energy goes into the sea floor, it loses energy through many causes: (1) intrinsic attenuation due to conversion of energy into heat; (2) transmission through reflectors; (3) reflector roughness and curvature; (4) scattering by inhomogeneities within the sediment, and so on (Hamilton, 1980).

In this thesis, the inverted seabed attenuation was obtained from long-range acoustic field data for which the surficial sediment layer with a thickness on the order of a few wavelengths plays the dominant role. When "attenuation" is used, it refers to the energy lost upon transmission of a compressional wave from all above causes and is thus "effective attenuation". For many purposes of underwater acoustics, it is effective attenuation that is desired for computations (Hamilton, 1976).

In general, compressional seabed attenuation may exhibit frequency dependence over a frequency band. The attenuation can approximately be expressed by an empirical form of a power law.

$$\alpha_b = k_b f^n \tag{1.1}$$

Where, α_b is attenuation in dB/m. k_b and n are empirically derived constants and f is frequency in KHz.

As is mentioned in part 1.2 of this chapter, Hamilton (1976) reported that effective attenuation is approximately related to the first power of frequency in most sediments from a few Hz to 1 MHz, i.e., n=1. But Stoll (1985) claimed that the assumption of an attenuation α_b that depends on the first power of frequency is unacceptable in the case of nearly all marine sediments, i.e., that in general, $n \neq 1$. Using the Biot-Stoll model with parameters, which are interpreted as the average acoustic

properties of an effective medium equivalent to sandy bottoms, seabed attenuation is predicted and shows a nonlinear frequency dependence (Zhou *et al.*, 2009).

In short, controversy lies in whether and under what conditions, the seabed effective attenuation has a linear frequency dependence. This research provides more high quality attenuation estimates over a frequency band of 63 Hz-1000 Hz. It is proposed that the non-linear frequency dependence of seabed effective attenuation could be justified using data from long-range broadband acoustic measurements.

This research will be accomplished by achieving the following specific objectives:

(1). Designing and performing an at-sea sub-experiment in the Shallow Water '06 experiment;

(2). Analyzing acoustic data collected from the Yellow Sea '96 experiment and the Shallow Water '06 experiment conducted off the New Jersey coast;

(3). Applying several characteristics of sound fields to matched field processing based geo-acoustic inversion, and performing single-parameter or multi-parameter inversions by optimization methods, such as genetic algorithms;

(4). Validating the resultant geo-acoustic parameters in the Shallow Water '06 experiment using spatial coherence data and TL data, which are independent of the data used in the estimation of geo-acoustic parameters.

(5). Discussing the geo-acoustic parameter sensitivity and studying the uncertainty of the geo-acoustic parameter estimates.

The completion of this research will help clarify the geo-acoustic model for certain sea bottoms and improve geo-acoustic inversion methodology.

1.5 Thesis Outline

The thesis is organized as follows. Descriptions of the Yellow Sea ’96 experiment and the Shallow Water '06 experiment conducted off the New Jersey coast are given in Chapter 2. In Chapter 3, the sound propagation modeling methods are introduced. In Chapter 4, seabed sound speed and attenuation are estimated using several single-parameter inversion techniques. Geo-acoustic parameter sensitivity and the uncertainty of geo-acoustic parameter estimates are discussed. In Chapter 5, multi-parameter inversions by optimization methods, such as genetic algorithms are utilized. The resultant geo-acoustic parameters from Chapter 5 are validated using spatial coherence data and TL data. Finally, Chapter 6 contains the summary of this research and suggests future research directions.

CHAPTER 2

EXPERIMENTS

In this research, acoustic data from the Yellow Sea '96 experiment (YS ’96) and Shallow Water '06 experiment (SW ’06) conducted off the coast of New Jersey are analyzed.

2.1 At-sea Experiment in the Yellow Sea: YS ’96

The Yellow Sea ’96 experiment was a shallow-water acoustics experiment conducted from August 22, 1996 to August 25, 1996 near the geographic center of the Yellow Sea (37^{o}N, 124^{o}E). The satellite picture of the experimental site is shown in Fig. 2.1. The experimental site has a very flat bottom. The depth of the water is 75 m with a deviation of ±1 m. About 315 broadband explosive sources (three hundred 38-g TNT and fifteen 1-kg TNT) were deployed at varying distances from the source ship (research vessel Shi Yan 2). The path of the source ship and the deployment points for the explosive sources are shown in Fig. 2.2. The source ship traveled along two straight lines (QA and QG) up to 57.2 km and along a quarter circle (BC) of radius 34 km. The Q-to-A track was taken from 12:10 to 19:55 UTC on August 22, 1996. The B-to-C track was taken from 23:00 UTC on August 22, 1996 to 05:34 UTC on August 23, 1996. The Q-to-G track was taken from 10:49 to 17:49 UTC on August 23, 1996.

The measurements were made with a 2-element vertical line array and a 32-element vertical line array. The 32-element vertical line array had an element spacing of 2 meters. The hydrophones of the 2-element vertical line array were deployed at depths of 7 m and 50 m, respectively. These two vertical line arrays were deployed from

research vessel Shi Yan 3, which held stationary at Q as shown in Fig 2.3. The sensor depths for the 32-element vertical line array are shown in Fig. 2.4.

Figure 2.1 Satellite picture of the experimental site for YS '96

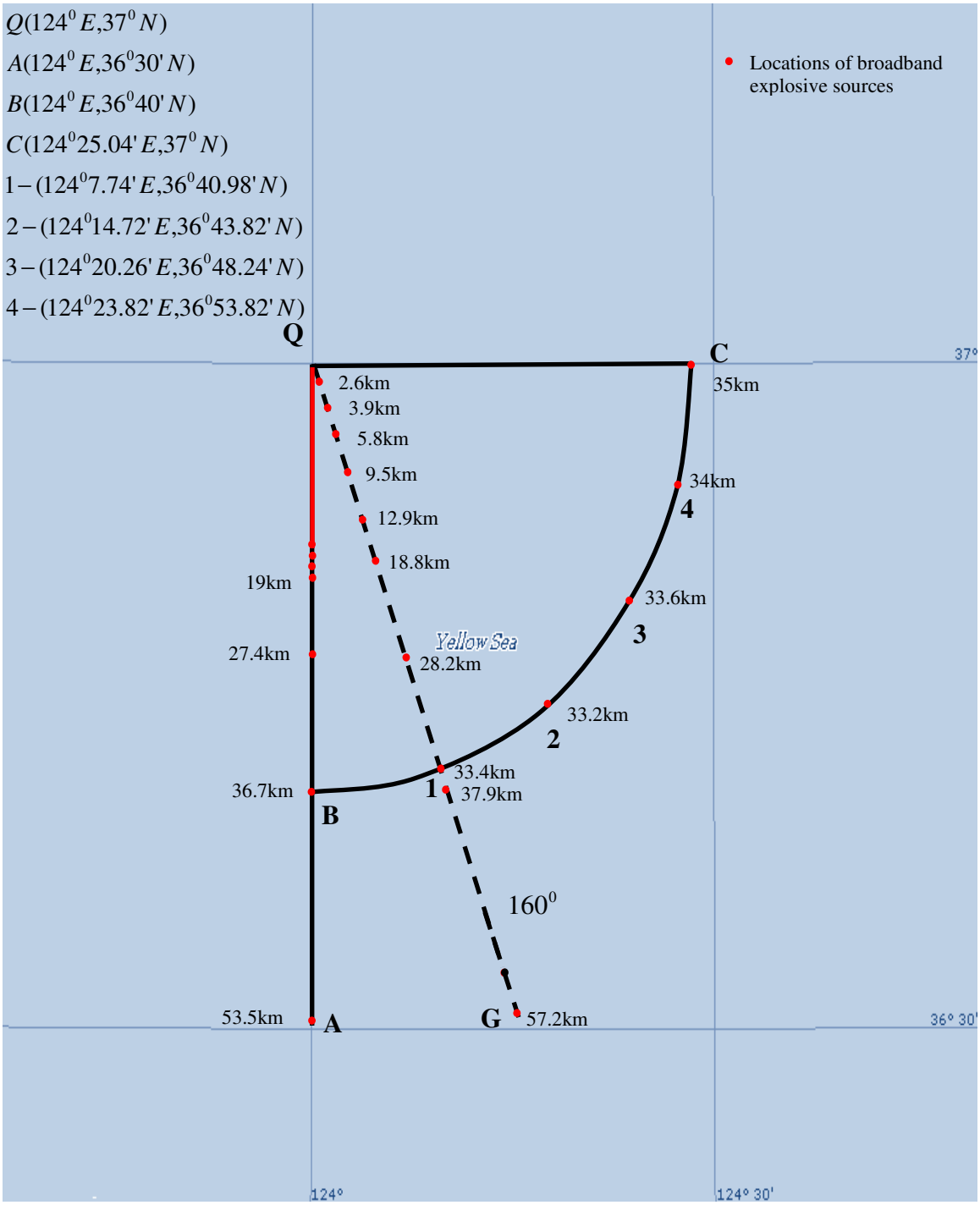

Figure 2.2 Path of the source ship (Shi Yan 2). Q is the location of receiving ship (Shi Yan 3).

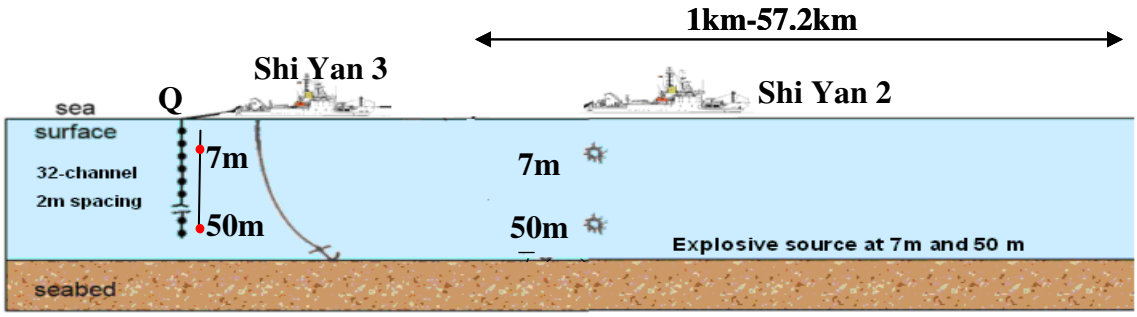

Figure 2.3 Experimental configuration for the Yellow Sea '96 sound propagation study.

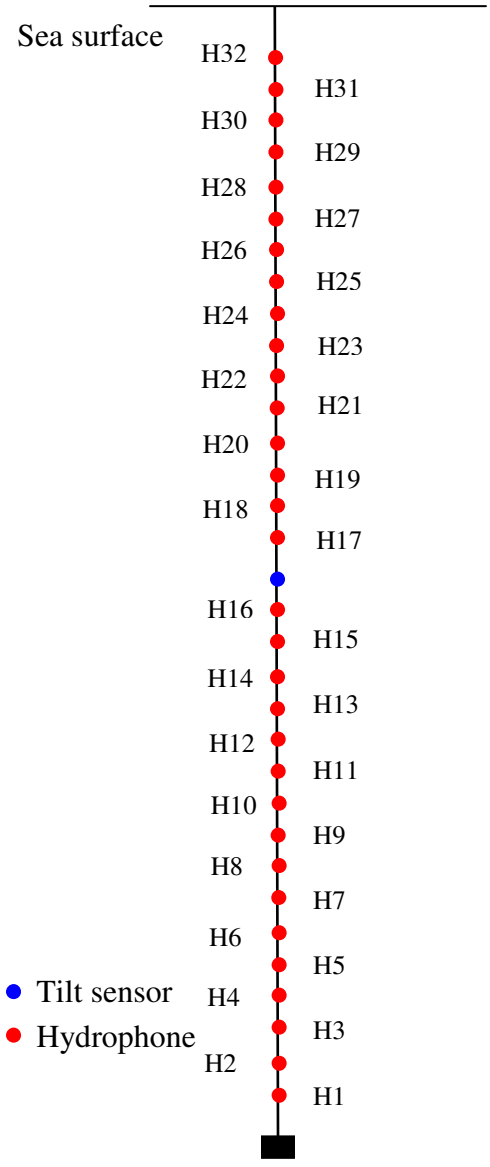

Hydrophone Number	Depth	Hydrophone number	Depth
H32	4m	H16	38m
H31	6m	H15	40m
H30	8m	H14	42m
H29	10m	H13	44m
H28	12m	H12	46m
H27	14m	H11	48m
H26	16m	H10	50m
H25	18m	H9	52m
H24	20m	H8	54m
H23	22m	H7	56m
H22	24m	H6	58m
H21	26m	H5	60m
H20	28m	H4	62m
H19	30m	H3	64m
H18	32m	H2	66m
H17	34m	H1	68m

Figure 2.4 Depth information for the 32-element vertical line array.

Water temperature, salinity and density as a function of depth were measured during the experiment. The sound speed in water can be calculated using Eq. (2.1) (Jensen *et al*., 2000).

$$c(z) = 1449.2 + 4.6T - 0.055T^2 + 0.00029T^3 + (1.34 - 0.01T)(S - 35) + 0.016z \quad (2.1)$$

where, T is temperature in degrees centigrade; S is salinity in parts per thousand; z is depth in meters(m).

The water column sound speed profile (SSP) was determined from the conductivity-temperature-depth data. Figure 2.5 shows sixteen measured SSPs as dashed lines and the averaged SSP as a solid line. The measured SSPs were obtained hourly at location Q from 12:58 to 19:58 UTC on August 22, 1996 and from 10:57 to 17:58 UTC on August 23, 1996. The SSP had a near-linear thermocline connecting a warm surface isothermal layer to a cooler isothermal bottom layer. These SSPs show a strong and sharp thermocline with temperature differences exceeding 15 degrees centigrade occurring over 15 meters of depth between 14 m and 29 m. The nominal depths of the source detonations were 7 m and 50 m, which were above and below the thermocline, respectively. Just prior to the Yellow Sea '96 experiment, bottom core data were taken by the South China Sea Institute of Oceanology. The density of the seabed was reported to be 1.85g/cm^3. The grain size distributions from two locations are listed in Table 2.1. The averaged mean grain diameter of the sediment was 0.0764 mm (3.71 ϕ). According to the Hamilton semi-empirical geo-acoustical model (Hamilton and Bachman, 1982), the surface sediments in this area can be described as a "very fine sand" or "silty sand". The seabed sound speed is affected by both mean grain size and porosity (Hamilton and Bachman, 1982), but no porosity information is available for this experiment. The ratio of

the seabottom sound speed to the sound speed in water column near the seabed is calculated, based solely on the mean grain size, using Jackson and Richardson's empirical relations (2006).

$$Ratio = 1.190 - 0.03956 M_Z + 1.9476 \times 10^{-3} M_Z^{\,2} \qquad (2.2)$$

where, M_Z is the mean grain size in ϕ. Substituting $M_Z = 3.71\,\phi$ into Eq. (2.2), the speed ratio is 1.07. Figure 2.5 shows that the sound speed in the water column near the seabed is around 1480 m/s. Thus, the seabottom sound speed is around 1584m/s. A similar result is obtained by Dahl and Choi (2006).

Table 2.1. The grain size distributions from two locations at the YS '96 site

No.	Location	Mean grain size		Gravel	Sand	Silt	Clay
		mm	ϕ	%	%	%	%
1	37°N, 124°05'E	0.0769	3.70	0.9	72.5	17.7	8.9
2	37°04'N, 124°E	0.0759	3.72	1.3	70.4	15.9	12.4

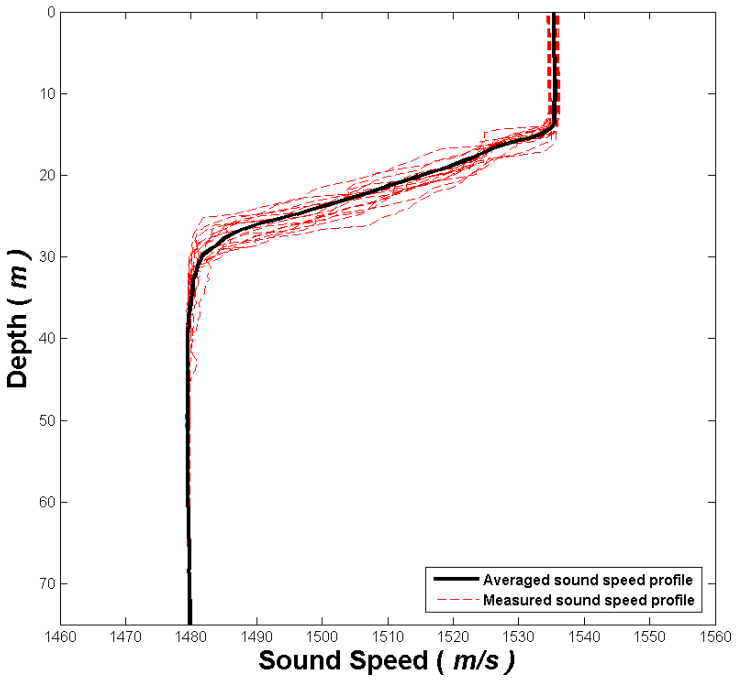

Figure 2.5 Sound speed profiles at location Q, showing a strong and sharp thermocline.

2.2 Shallow Water ’06 Experiment Conducted Off the New Jersey Coast: SW ’06

The Shallow Water ‘06 experiment was a comprehensive ocean acoustics and physical oceanography experiment conducted over seven weeks in the summer of 2006. This experiment was focused on a 40-by-50-kilometer patch of ocean about 100 miles east of Atlantic City, N.J (See figure 2.6). This large scale experiment included six research vessels (R.V.s), more than 50 scientists from 12 institutions, 62 moorings, 350 assorted oceanographic sensors, an airplane, space satellites, and robotic undersea gliders (See figure 2.7). Figure 2.8 shows the six research vessels. In this thesis, the acoustic signals transmitted by R.V. Knorr and R.V. Sharp are analyzed.

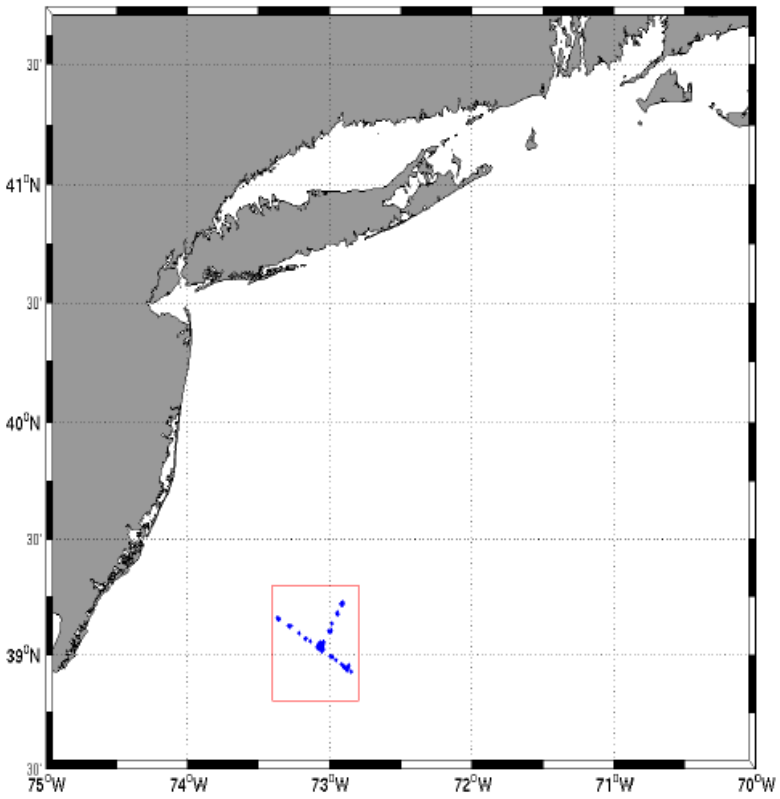

Figure 2.6 SW ’06 experiment area directly east of Atlantic City, NJ. (Newhall *et al.*, 2007)

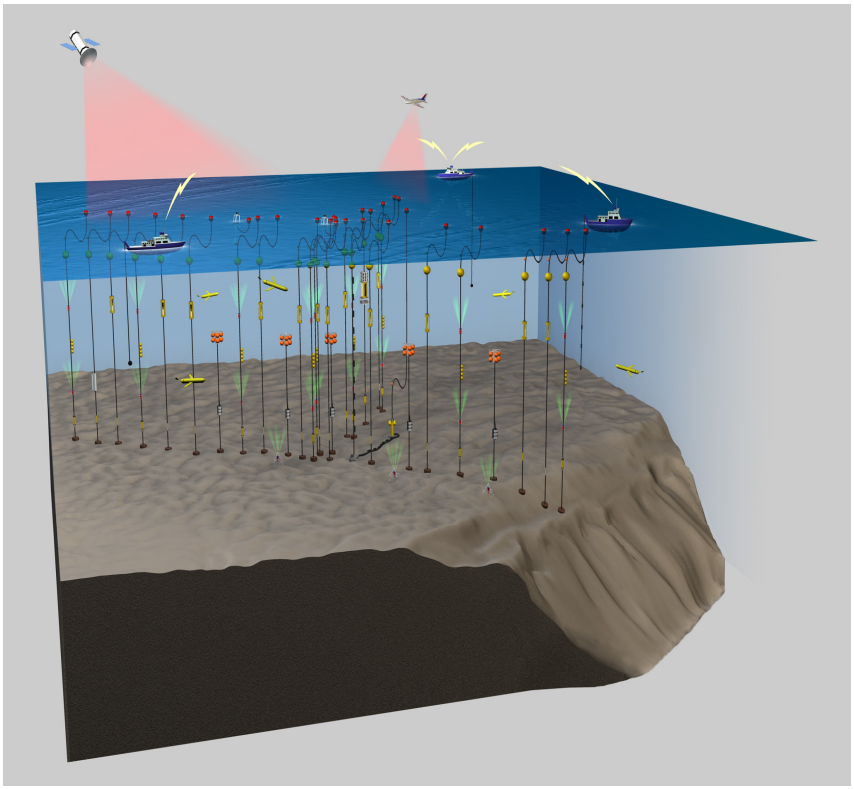

Figure 2.7 SW ’06 experiment area cartoon. (Nevala and Lippsett, 2007)

R/V Tioga

R/V Knorr

R/V Quest

R/V Oceanus

R/V Sharp

R/V Endeavor

Figure 2.8 The six research vessels used in the Shallow Water ’06 experiment

2.2.1 Sub-experiment One in SW '06

As part of the Shallow Water '06 experiment, one 52-element L-shaped array (SWAMI52) and one 32-element L-shaped array (SWAMI32) were deployed at site A (39^o 12'N, 72^o 57.97'W) and site B (39^o 3.6'N, 73^o 7.90'W) respectively (shown in Fig.9). The water depth was about 75 m.

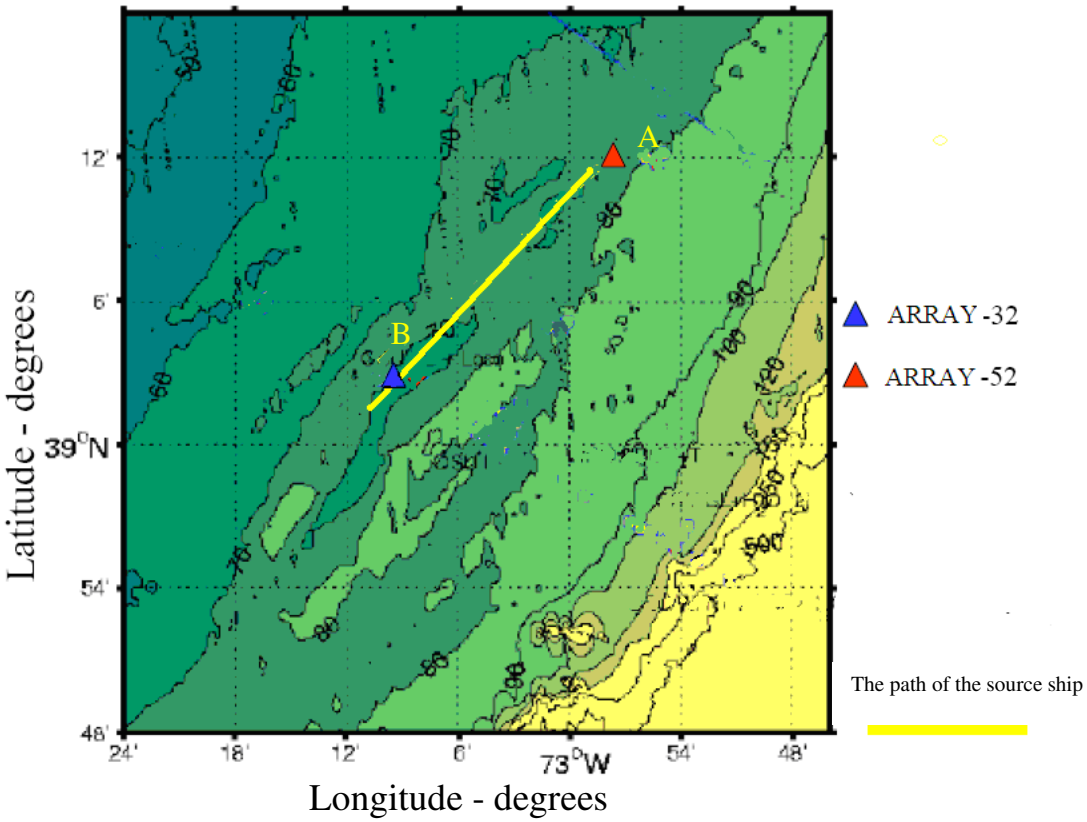

Figure 2.9. The path of the source ship (R/V Knorr) and the locations of the two L-shaped arrays

The vertical line array (VLA) portion of SWAMI52 had 16 elements with an element spacing of 4.37 m. The VLA portion of SWAMI32 had 12 elements with an element spacing of 5.95 m. The VLA portion of both SWAMI52 and SWAMI32 covered most of the water column. The horizontal line array (HLA) portions of SWAMI52 and SWAMI32 had 36 elements and 20 elements respectively and were laid on the sea

bottom. The HLA portion of SWAMI52 had a length of 230 m and the HLA portion of SWAMI32 had a length of 256.43 m. The constructions of SWAMI32 and SWAMI52 are shown in Figs. 2.10 and 2.11 respectively. Hydrophone location details are listed in Table 2.2.

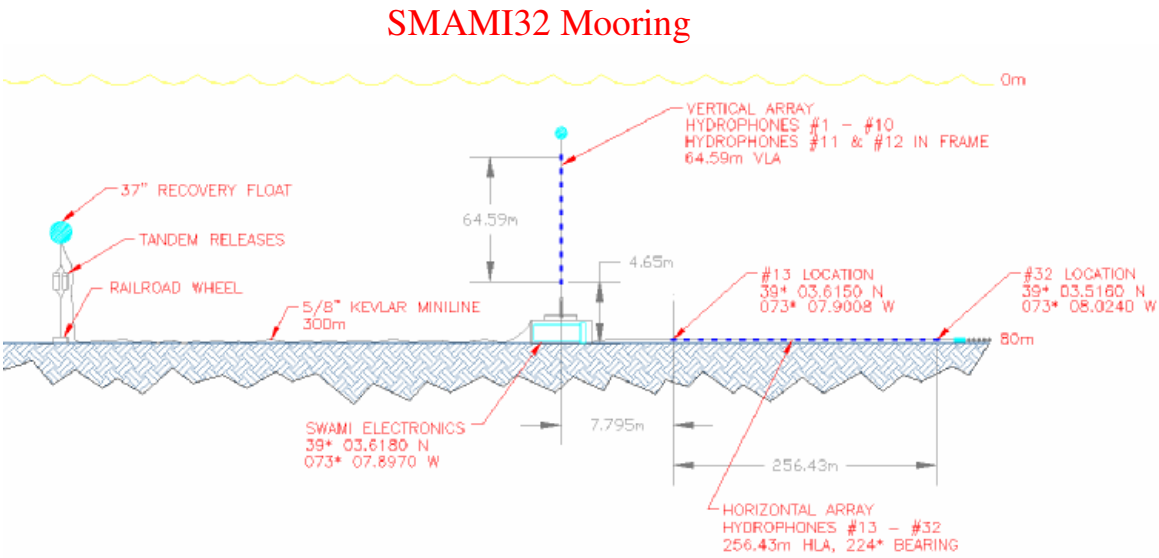

Figure 2.10. The construction of SWAMI32

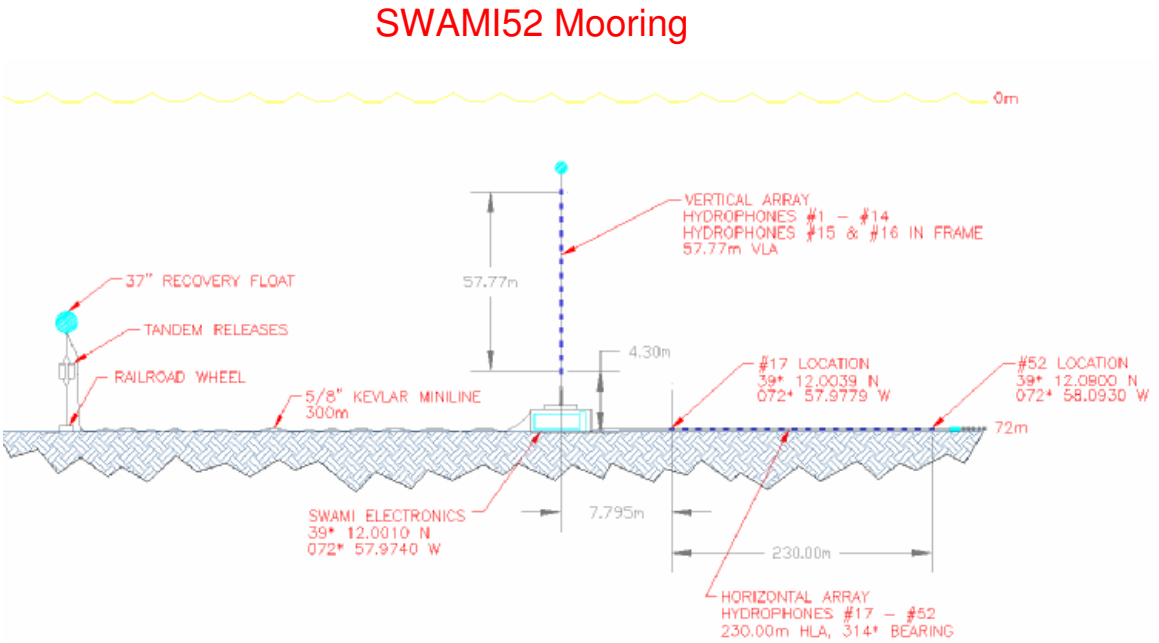

Figure 2.11. The construction of SWAMI52

Table 2.2a Depth information for VLA portion of SWAMI32

Hydrophone Number	Spacing (m)	From top (m)	Element depth (m)
1		1.00	11.00
2	5.95	6.95	16.95
3	5.95	12.91	22.91
4	5.95	18.86	28.86
5	5.95	24.82	34.82
6	5.95	30.77	40.77
7	5.95	36.72	46.72
8	5.95	42.68	52.68
9	5.95	48.63	58.63
10	5.95	54.59	64.59
11	5.95	60.54	70.54
12	5.95	66.49	76.49

Table 2.2b Position information for HLA portion of SWAMI32

Hydrophone Number	Spacing (m)	From Hydrophone #13 (m)
13		0.00
14	20.32	20.32
15	19.34	39.66
16	18.40	58.06
17	17.51	75.57
18	16.67	92.24
19	15.86	108.10
20	15.10	123.20
21	14.37	137.57
22	13.67	151.24
23	13.01	164.25
24	12.38	176.63
25	11.79	188.42
26	11.22	199.64
27	10.67	210.31
28	10.16	220.47
29	9.67	230.14
30	9.20	239.34
31	8.76	248.10
32	8.33	256.43

Table 2.2c Depth information for VLA portion of SWAMI52

Hydrophone Number	Spacing (m)	From top (m)	Element depth (m)
1		1.00	11.00
2	4.37	5.37	15.37
3	4.37	9.73	19.73
4	4.37	14.10	24.10
5	4.37	18.47	28.47
6	4.37	22.83	32.83
7	4.37	27.20	37.20
8	4.37	31.57	41.57
9	4.37	35.93	45.93
10	4.37	40.30	50.30
11	4.37	44.67	54.67
12	4.37	49.03	59.03
13	4.37	53.40	63.40
14	4.37	57.77	67.77
15	4.37	62.13	72.13
16	4.37	66.50	76.50

Table 2.2d Position information for HLA portion of SWAMI52

Hydrophone Number	Spacing (m)	From Hydrophone #17 (m)	Hydrophone Number	Spacing (m)	From Hydrophone #17 (m)
17		0.00	39	3.44	128.53
18	15.84	15.84	40	3.73	132.26
19	13.64	29.48	41	4.04	136.30
20	11.73	41.21	42	4.37	140.67
21	10.11	51.32	43	4.73	145.40
22	8.68	60.00	44	5.12	150.52
23	7.49	67.49	45	5.55	156.07
24	6.45	73.94	46	6.44	162.51
25	5.54	79.48	47	7.48	169.99
26	5.12	84.60	48	8.70	178.69
27	4.73	89.33	49	10.10	188.79
28	4.37	93.70	50	11.73	200.52
29	4.04	97.74	51	13.64	214.16
30	3.73	101.47	52	15.84	230.00
31	3.44	104.91			
32	3.18	108.09			
33	2.94	111.03			
34	2.72	113.75			
35	2.50	116.25			
36	2.72	118.97			
37	2.94	121.91			
38	3.18	125.09			

From August 29, 2006 to September 4, 2006, about 170 light bulb implosion sources and 8 combustive sound sources (CSS) were deployed at different distances between the source ship (R/V Knorr) and the two SWAMI arrays. The path of the source ship is shown in Fig. 2.9. The source ship traveled along the straight line connecting points A and B. The track was perpendicular to the HLA portion of SWAMI52 and parallel to the HLA portion of SWAMI32 (see Fig. 2.12).

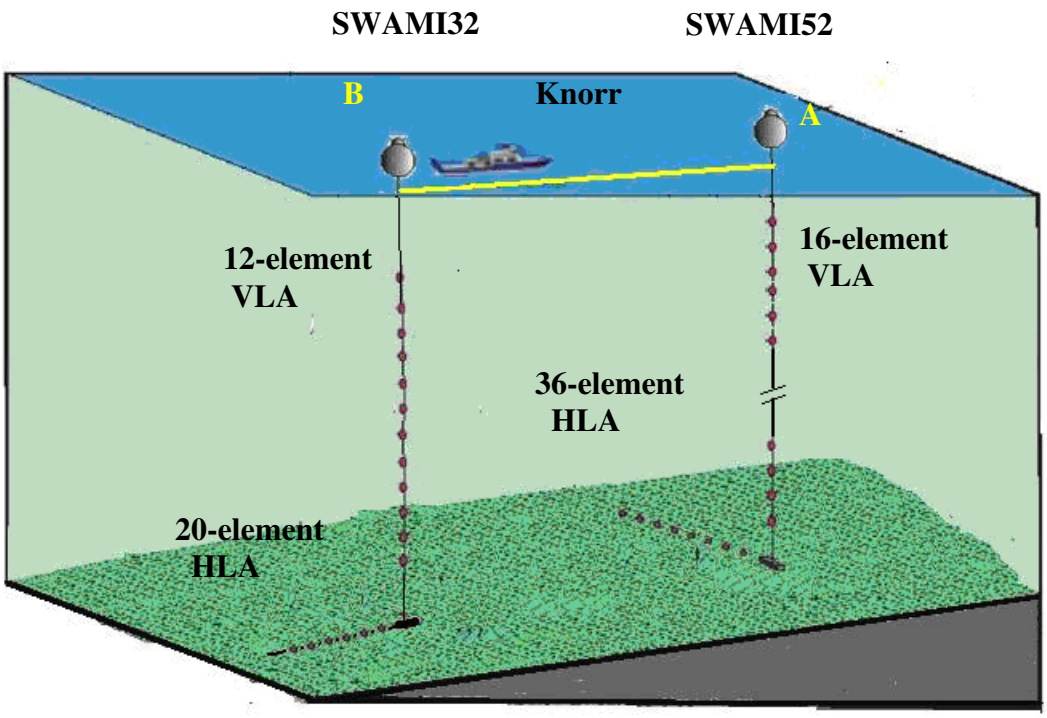

Figure 2.12. Sub-experiment one configuration

Water column sound speed profiles were determined from conductivity-temperature-depth (CTD) data. Figure 2.13 shows the average sound speed profile measured on September 4, 2006 (GMT). The wind speed was less than 3 m/s on September 4, 2006 (GMT).

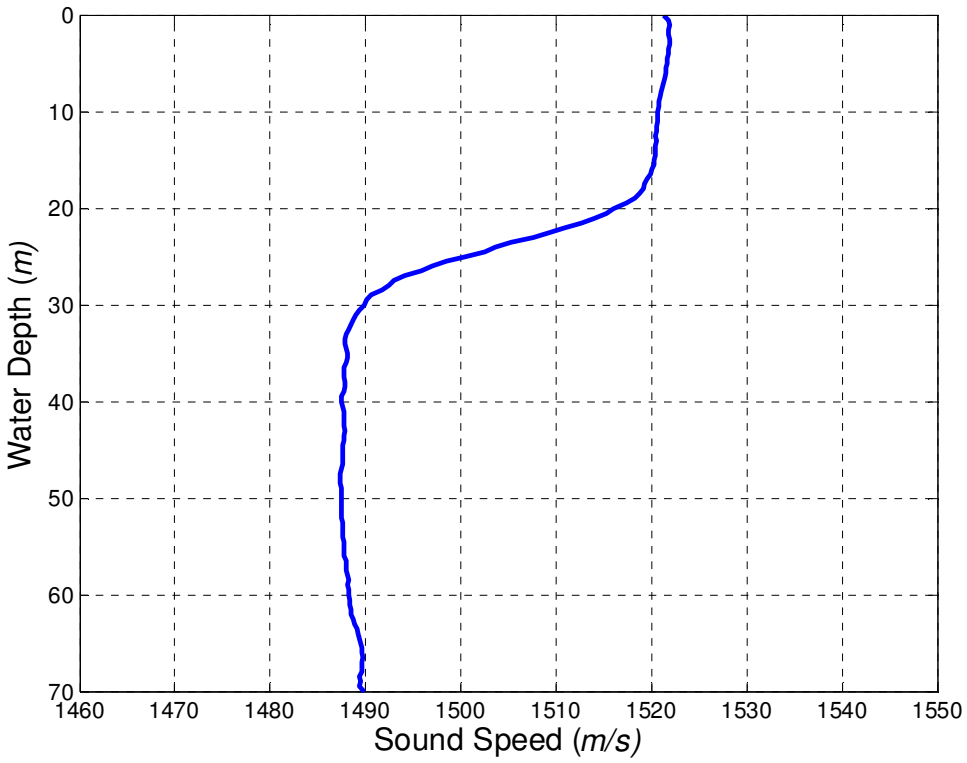

Figure 2.13 Averaged sound speed profile on September 4, 2006

2.2.2 Sub-experiment Two in SW '06

During the Shallow Water '06 experiment, another L-shaped array (Shark), shown in Fig. 2.14, was deployed by Woods Hole Oceanographic Institution at site O (39^{o} 01.25'N, 73^{o} 02.98'W). The water depth was about 80 m.

The vertical line array (VLA) portion of Shark had 16 elements and spanned the water column between 13.5 m and 77.25 m depth. The horizontal line array (HLA) portion of Shark had 32 elements and was laid on the sea bottom. The Shark mooring diagram is shown in Figs. 2.15. The locations of hydrophones on the Shark array are listed in Table 2.3.

Figure 2.14 Shark electronics battery sled (Newhall *et al.*, 2007)

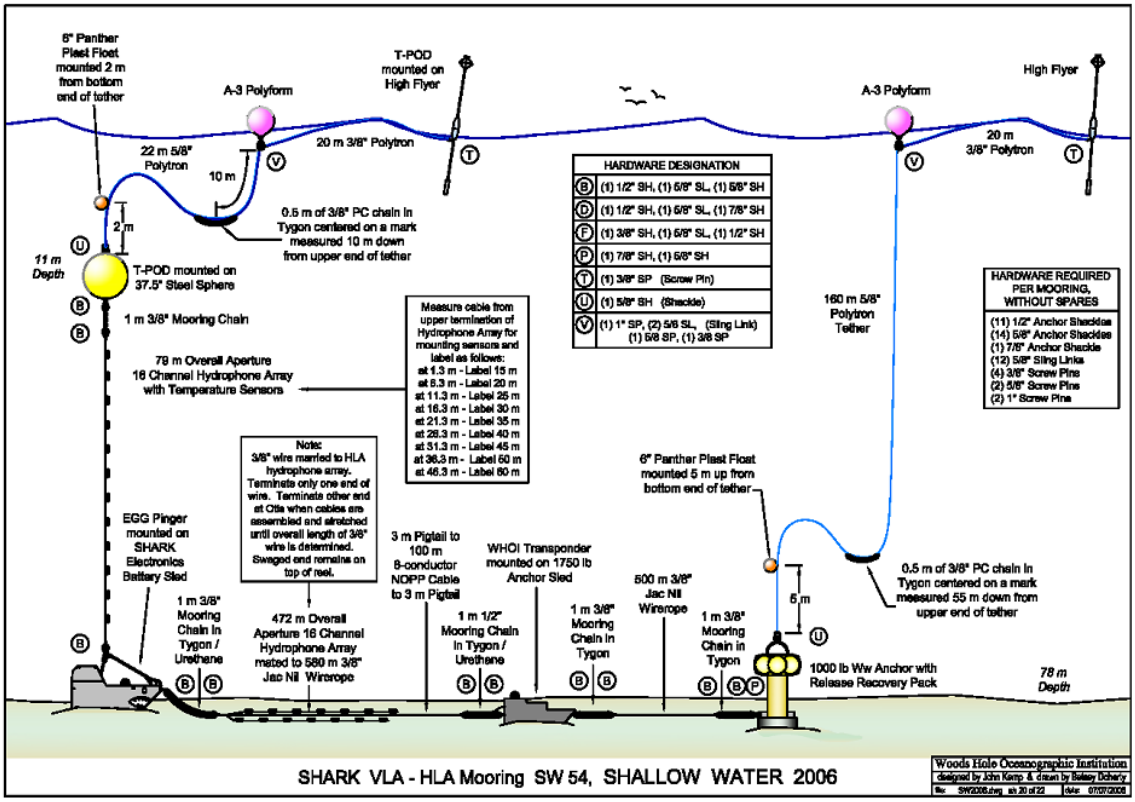

Figure 2.15 Shark mooring diagram (Newhall *et al.*, 2007)

Table 2.3a Depth information for VLA portion of Shark

Hydrophone Number	Spacing (m)	Element depth (m)
0		13.50
1	3.75	17.25
2	3.75	21.00
3	3.75	24.75
4	3.75	28.50
5	3.75	32.25
6	3.75	36.00
7	3.75	39.75
8	3.75	43.50
9	3.75	47.25
10	7.50	54.75
11	7.50	62.25
12	7.50	69.75
13	0	77.25
14	0	77.75
15	0	77.75

The VLA was shortened prior to deployment since the water depth was shallower than the VLA was originally designed for. The lower hydrophones, numbers 13, 14, and 15, were wrapped together to reduce its length.

Table 2.3b Locations of hydrophones on the HLA portion of Shark

Hydrophone Number	Location	Distance from Shark Body (m)
16	39 01.5156(N) 73 02.9804(W)	468
17	39 01.5074(N) 73 02.9807(W)	453
18	39 01.4993(N) 73 02.9809(W)	438
19	39 01.4912(N) 73 02.9812(W)	423
20	39 01.4831(N) 73 02.9815(W)	408
21	39 01.4750(N) 73 02.9817(W)	393
22	39 01.4669(N) 73 02.9820(W)	378
23	39 01.4588(N) 73 02.9823(W)	363
24	39 01.4507(N) 73 02.9825(W)	348
25	39 01.4426(N) 73 02.9828(W)	333
26	39 01.4345(N) 73 02.9831(W)	318
27	39 01.4264(N) 73 02.9833(W)	303
28	39 01.4183(N) 73 02.9836(W)	288
29	39 01.4102(N) 73 02.9839(W)	273
30	39 01.4021(N) 73 02.9841(W)	258
31	39 01.3940(N) 73 02.9844(W)	243
32	39 01.3859(N) 73 02.9847(W)	228
33	39 01.3778(N) 73 02.9849(W)	213
34	39 01.3697(N) 73 02.9852(W)	198
35	39 01.3616(N) 73 02.9855(W)	183
36	39 01.3535(N) 73 02.9857(W)	168
37	39 01.3454(N) 73 02.9860(W)	153
38	39 01.3373(N) 73 02.9863(W)	138
39	39 01.3292(N) 73 02.9865(W)	123
40	39 01.3211(N) 73 02.9868(W)	108
41	39 01.3129(N) 73 02.9871(W)	93
42	39 01.3048(N) 73 02.9873(W)	78
43	39 01.2967(N) 73 02.9876(W)	63
44	39 01.2886(N) 73 02.9879(W)	48
45	39 01.2805(N) 73 02.9881(W)	33
46	39 01.2724(N) 73 02.9884(W)	18
47	39 01.2643(N) 73 02.9886(W)	3

Several geo-acoustic inversion tracks were designed and are shown in Fig. 2.16. From August 11, 2006 to August 15, 2006, the source ship (R/V Sharp) traveled along those geo-acoustic inversion tracks. Chirp signals were transmitted at different distances between the source ship (R/V Sharp) and the Shark array.

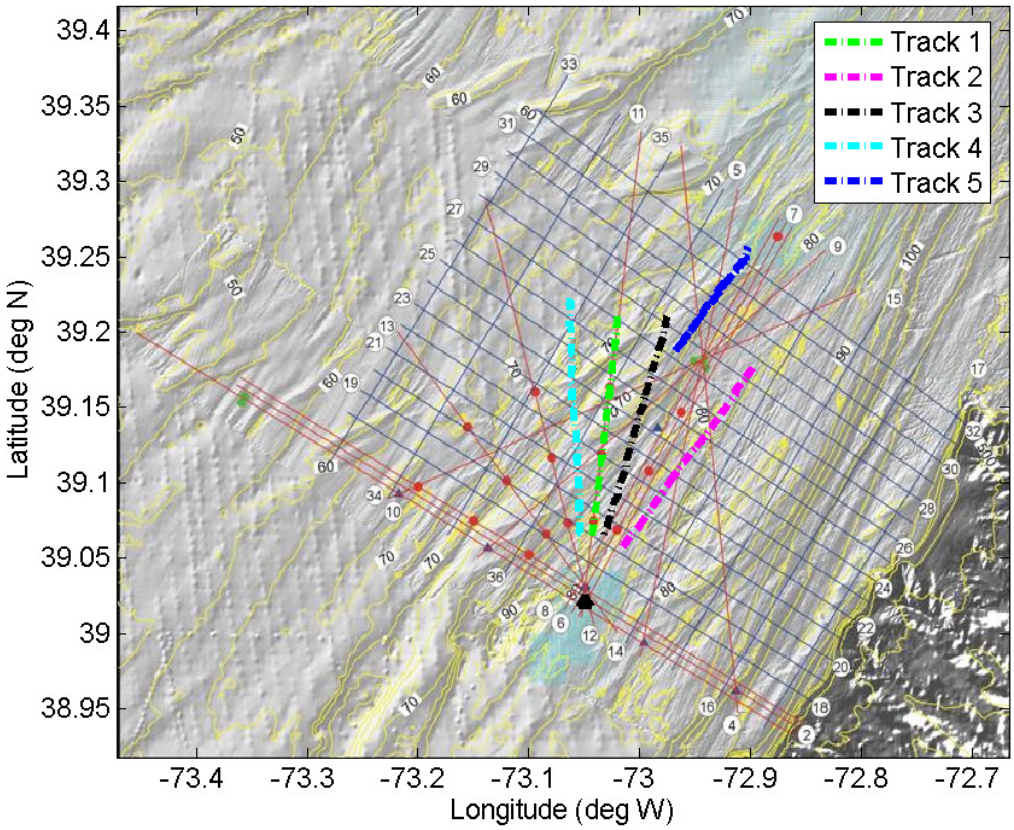

Figure 2.16 Geo-acoustic inversion tracks.
The location of Shark array is shown by the black triangle.

CHAPTER 3

SOUND PROPAGATION MODELS

3.1 Normal Mode Method

Sound propagation in the ocean is governed by the wave equation, with parameters and boundary conditions descriptive of the ocean environment. Normal mode theory is a widely used approach for modeling sound propagation in shallow water. One of the earliest normal mode papers was published in 1948 by Pekeris (Perkeris, 1948) who developed the theory for a simple two-layer model (ocean and sea bottom) with constant sound speed in each layer. Its mathematical derivation based on separation of variables can be found in Jensen's book (Jensen *et al*., 2000).

The Helmholtz equation, which is the frequency-domain wave equation, can be derived from the wave equation by use of the frequency-time Fourier transform pair. The Helmholtz equation, rather than the wave equation, forms the theoretical basis in ocean acoustic applications, because ocean acoustic experiments are characterized by hundreds or thousands of interactions with any single boundary (Jensen *et al*., 2000).

3.1.1 Normal Modes for Range-Independent Environments

The inhomogeneous Helmholtz equation in cylindrical coordinates is given by:

$$\frac{1}{r}\frac{\partial}{\partial r}(r\frac{\partial p}{\partial r})+\rho(z)\frac{\partial}{\partial z}(\frac{1}{\rho(z)}\frac{\partial p}{\partial z})+\frac{\omega^2}{c^2(z)}p\approx-\frac{\delta(z-z_s)\delta(r)}{2\pi r} \tag{3.1}$$

where p is acoustic pressure, ρ is density, c is sound speed, z_s is source depth (Jensen *et al*., 2000).

The technique of separation of variables is used to solve the Helmholtz equation. The right hand side of Eq. (3.1) is set to zero, to obtain the unforced Helmholtz equation:

$$\frac{1}{r}\frac{\partial}{\partial r}(r\frac{\partial p}{\partial r})+\rho(z)\frac{\partial}{\partial z}(\frac{1}{\rho(z)}\frac{\partial p}{\partial z})+\frac{\omega^2}{c^2(z)}p\approx 0 \tag{3.2}$$

Application of separation variables ($p(r,z)=R(r)\Psi(z)$) into Eq. (3.2), yields

$$\frac{1}{R}\left[\frac{1}{r}\frac{d}{dr}(r\frac{dR}{dr})\right]+\frac{1}{\Psi}\left[\rho(z)\frac{d}{dz}\left(\frac{1}{\rho(z)}\frac{d\Psi}{dz}\right)+\frac{\omega^2}{c^2(z)}\Psi\right]=0 \tag{3.3}$$

In Eq. (3.3), the component in the first bracket is a function of *r* only and the component in the second bracket is a function of *z* only. Equation (3.3) is satisfied only if each component is equal to a constant. The separation constant is defined as k_c^2. Using the component in the second bracket of Eq. (3.3), yields

$$\rho(z)\frac{d}{dz}\left(\frac{1}{\rho(z)}\frac{d\Psi(z)}{dz}\right)+\left(\frac{\omega^2}{c^2(z)}-k_c^2\right)\Psi(z)=0 \tag{3.4}$$

In a shallow water waveguide, the boundary condition at the pressure release surface:

$$\Psi(z)\big|_{z=0}=0 \tag{3.5}$$

The boundary condition of continuity of sound pressure and normal velocity at the bottom interface:

$$\Psi(z)\big|_{z=H^+}=\Psi(z)\big|_{z=H^-} \tag{3.6}$$

$$\frac{1}{\rho}\frac{d\Psi(z)}{dz}\bigg|_{z=H^+}=\frac{1}{\rho}\frac{d\Psi(z)}{dz}\bigg|_{z=H^-} \tag{3.7}$$

where *H* is the water depth; the notation $z\to H^+$ denotes the limit as z tends to the boundary from the bottom layer; the notation $z\to H^-$ denotes the limit as z tends to the boundary from the water.

The general solution of Eq. (3.4) in the seabottom (z>H) can be written as

$$\Psi(z)\big|_{z>H} = B1e^{-\gamma_b z} + B2e^{\gamma_b z} \tag{3.8}$$

where, $\gamma_b \equiv \sqrt{k_c^2 - \left(\frac{\omega}{c_b}\right)^2}$ (3.9)

and c_b is the seabed sound speed. If γ_b is assumed to be positive, then $B2 = 0$ because of the bounded solution at infinity.

The boundary conditions (3.6) and (3.7) become

$$\Psi(H) = B1e^{-\gamma_b H} \tag{3.10}$$

$$\frac{1}{\rho}\frac{d\Psi(H)}{dz} = -B1\frac{\gamma_b e^{-\gamma_b H}}{\rho_b} \tag{3.11}$$

where, ρ_b is the seabed density. By dividing Eqs. (3.10) and (3.11), the boundary condition is obtained:

$$\Psi(H) + \frac{\rho_b}{\rho\sqrt{k_c^2 - \left(\frac{\omega}{c_b}\right)^2}}\frac{d\Psi(H)}{dz} = 0 \tag{3.12}$$

Equation (3.4) with boundary conditions (3.5) and (3.12) is a Sturm-Liouville eigenvalue problem with eigenvalues $k_{n,c}$ and eigenfunction $\Psi_n(z)$, where *n* is the mode number (Katsnelson and Petnikov, 2002). This Sturm-Liouville eigenvalue problem is singular, because the boundary condition Eq. (3.12) involves the eigenvalue in a square root function and introduces a branch cut in the eigenvalue plane.

Jensen *et al*. (2000) obtain the solution to the Helmholtz equation:

$$p(r,z) = \frac{i}{4\rho(z_s)}\sum_{n=1}^{M}\Psi_n(z_s)\Psi_n(z)H_0^{(1)}(k_{n,c}r) - \int_{C_{EJP}} \tag{3.13}$$

where, $H_0^{(1)}(k_{n,c}r)$ is the zero order Hankel function of the first kind and $\int_{C_{EJP}}$ is the branch cut integral (Ewing, Jardetzky, and Press, 1957), which is introduced by the boundary condition (3.12).

Equation (3.13) includes a mixed spectrum composed of a discrete and a continuous part. The discrete spectrum involves a sum of modes while the continuous spectrum involves an integral over a continuum of points in the eigenvalue plane. The contribution of the integral can generally be neglected at comparatively long distances (Jensen *et al*., 2000; Katsnelson and Petnikov, 2002). Equation (3.13) becomes

$$p(r,z) \approx \frac{i}{4\rho(z_s)} \sum_{n=1}^{M} \Psi_n(z_s)\Psi_n(z) H_0^{(1)}(k_{n,c}r) \tag{3.14}$$

The Hankel function can be approximated to its asymptotic form shown in Eq. (3.15) if $k_{n,c}r >> 1$

$$H_0^{(1)}(k_{n,c}r) \approx \sqrt{\frac{2}{\pi k_{n,c}r}} e^{-i\frac{\pi}{4}} e^{ik_{n,c}r} \tag{3.15}$$

Combining (3.14) and (3.15) together, the following solution to the Helmholtz equation is obtained.

$$p(r,z) \approx \frac{i}{\rho(z_s)} \sqrt{\frac{1}{8\pi}} e^{(-i\pi/4)} \sum_{n=1}^{M} \Psi_n(z_s)\Psi_n(z) \frac{e^{ik_{n,c}r}}{\sqrt{k_{n,c}r}} \tag{3.16}$$

In Eq. (3.16), eigenvector $\Psi_n(z)$ is also named as mode depth function and it has the orthogonality property:

$$\int_0^{\infty} \Psi_m(z)\Psi_n(z)/\rho(z)dz = \delta_{mn} \tag{3.17}$$

where, the integral interval includes the water column and the sediment.

The eigenvalue $k_{n,c}$ is a complex number:

$$k_{n,c} = k_n + i\beta_n \tag{3.18}$$

where, k_n is the horizontal wave number and β_n is the modal attenuation coefficient. The horizontal wave number can be used to define the group and phase velocity. The group velocity of the nth mode is:

$$V_g^n = \frac{d\omega}{dk_n} \tag{3.19}$$

The phase velocity of the nth mode is:

$$V_p^n = \frac{\omega}{k_n} \tag{3.20}$$

The group velocity represents the energy transport velocity of a mode, and the phase velocity represents the horizontal velocity of a particular phase in the plane wave representation of a mode (Jensen *et al.*, 2000).

To compute the sound field using normal mode theory, the eigenvector $\Psi_n(z)$ and eigenvalue $k_{n,c}$ need to be found. For a known environment, $\Psi_n(z)$ and $k_{n,c}$ can be obtained using a normal mode model, such as KRAKEN (Porter, 1992). KRAKEN, developed by Michael Porter, is a normal mode propagation code. It uses a fast finite difference method to accurately determine the eigenvector $\Psi_n(z)$ and eigenvalue $k_{n,c}$. It consists of a combination of several numerical procedures, such as bisection method and Richardson extrapolation (Porter and Reiss, 1984). As an example, figure 3.1 shows the first four mode shapes in YS '96 at 200 Hz obtained using KRAKEN with the range-independent averaged sound speed profile of figure 2.5.

Normally, transmission loss (TL) rather than the complex pressure field is used to study the sound propagation. TL is defined by Eq. (3.21)

$$TL = -20\log\left|\frac{p(r,z)}{p_0(r=1)}\right| \tag{3.21}$$

$p_0(r=1)$ is the sound pressure at 1 m from the source.

Substituting Eq. (3.17) into Eq. (3.21), yields

$$TL(r,z) \approx -20\log\left|\frac{\sqrt{2\pi/r}}{\rho(z_s)}\sum_{n=1}^{M}\Psi_n(z_s)\Psi_n(z)\frac{e^{ik_{n,c}r}}{\sqrt{k_{n,c}}}\right| \tag{3.22}$$

The incoherent TL is defined by:

$$TL^{Inc}(r,z) \approx -20\log\frac{\sqrt{2\pi/r}}{\rho(z_s)}\sqrt{\sum_{n=1}^{M}\left|\frac{\Psi_n(z_s)\Psi_n(z)}{\sqrt{k_{n,c}}}\right|^2} \tag{3.23}$$

In some shallow water problems, where the modes are bottom-interacting, a simulated TL obtained by using an incoherent modal summation is compared with measured experimental data that is averaged over frequency. The detailed interference fine structure predicted by the coherent TL calculation is not always physically meaningful (Jensen *et al.*, 2000).

Figure 3.2 shows the comparison between coherent and incoherent TL as a function of range using the range-independent averaged sound speed profile in figure 2.5. The source depth is 50 m, the receiver depth is 7 m and the frequency is 100Hz.

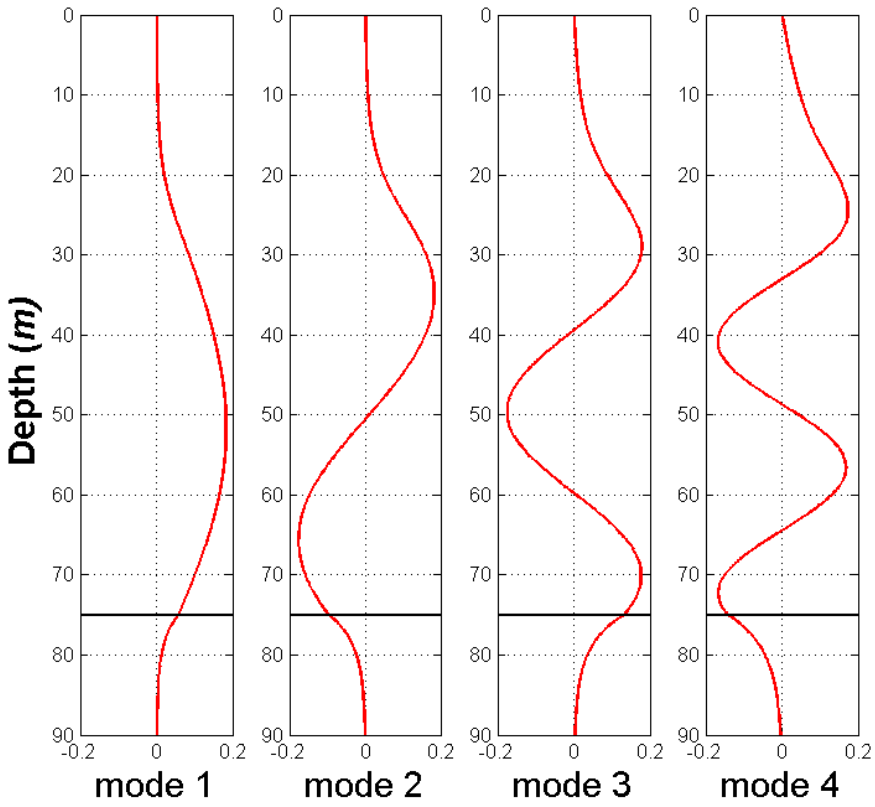

Figure 3.1 First four mode shapes at the YS ’96 site (200 Hz) using range-independent sound speed profile.

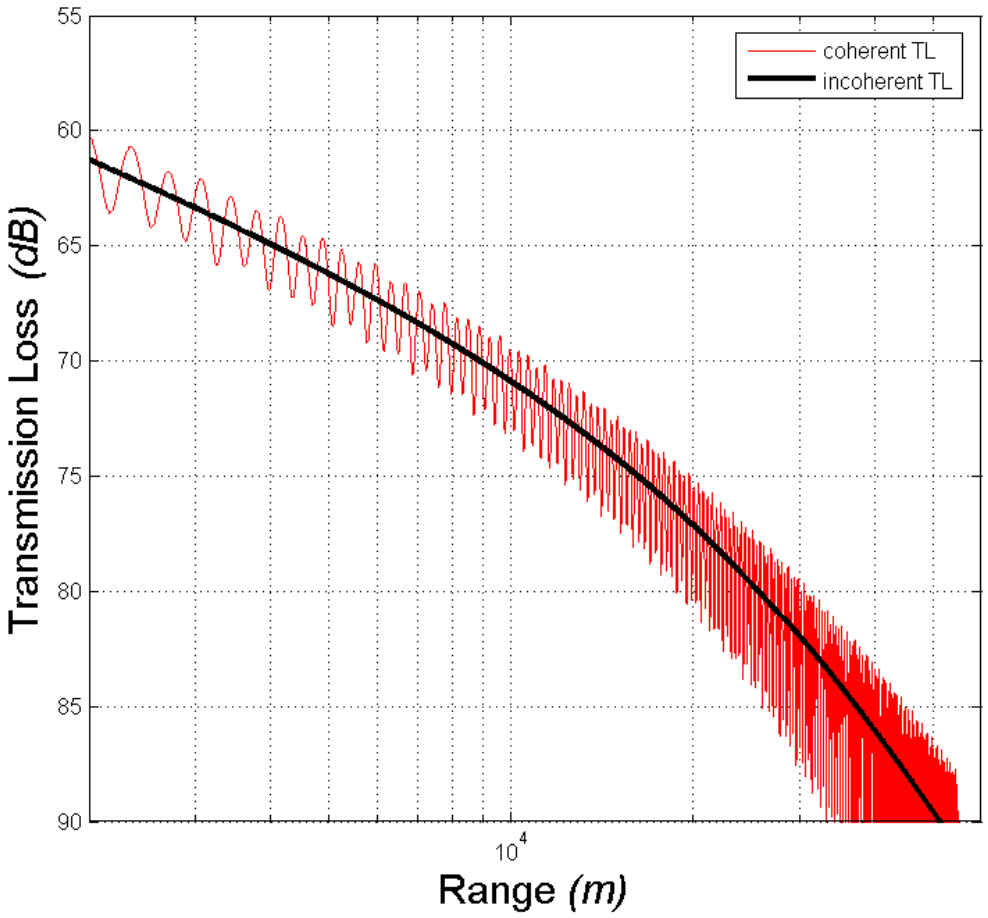

Figure 3.2 Transmission Loss as a function of range at 100 Hz

3.1.2 Normal Modes for Range-Dependent Environments

The Normal mode method is primarily suitable for range-independent environments. However, it can also solve range-dependent problems by dividing the range axis into a number of segments and approximating the field as range-independent within each segment. The boundary condition at the interface of two segments is satisfied by the continuity of sound pressure and normal velocity. Finally, the range-independent solution within each segment is 'glued' together to solve the range-dependent problem (Jensen *et al*., 2000).

Figure 3.3 shows that the range-dependent problem is divided into M segments in range. The general solution in the *j*th segment can be written as follows (Evans, 1983):

$$p^j(r,z) = \sum_{n=1}^{N} \left[a_n^j \hat{H}1_n^j(r) + b_n^j \hat{H}2_n^j(r) \right] \times \Psi_n^j(z) \tag{3.24}$$

where, $\hat{H}1_n^j(r) = \dfrac{H_0^{(1)}(k_{n,c}^j r)}{H_0^{(1)}(k_{n,c}^j r_{j-1})} \approx \sqrt{\dfrac{r_{j-1}}{r}} \exp(ik_{n,c}^j (r - r_{j-1}))$ (3.25)

$$\hat{H}2_n^j(r) = \frac{H_0^{(2)}(k_{n,c}^j r)}{H_0^{(2)}(k_{n,c}^j r_{j-1})} \approx \sqrt{\frac{r_{j-1}}{r}} \exp(-ik_{n,c}^j (r - r_{j-1})) \tag{3.26}$$

$$\begin{bmatrix} a_n^{j+1} \\ b_n^{j+1} \end{bmatrix} = \begin{bmatrix} R1_n^j & R2_n^j \\ R3_n^j & R4_n^j \end{bmatrix} \begin{bmatrix} a_n^j \\ b_n^j \end{bmatrix} = \begin{bmatrix} R1_n^j & R2_n^j \\ R3_n^j & R4_n^j \end{bmatrix} \cdots \begin{bmatrix} R1_n^1 & R2_n^1 \\ R3_n^1 & R4_n^1 \end{bmatrix} \begin{bmatrix} a_n^1 \\ b_n^1 \end{bmatrix} \tag{3.27}$$

Equations (3.25) and (3.26) are the scaling of the Hankel functions. This can avoid overflow for the modes, which involve growing and decaying exponentials. Equation (3.27) shows a recursive relation, R is the propagator matrix.

$$R1_n^j = \frac{1}{2}(\tilde{C}_n^j + \hat{C}_n^j) H1_n^j; \tag{3.28}$$

$$R2_n^j = \frac{1}{2}(\tilde{C}_n^j - \hat{C}_n^j)H2_n^j; \tag{3.29}$$

$$R3_n^j = \frac{1}{2}(\tilde{C}_n^j - \hat{C}_n^j)H1_n^j; \tag{3.30}$$

$$R4_n^j = \frac{1}{2}(\tilde{C}_n^j + \hat{C}_n^j)H2_n^j \tag{3.31}$$

where, $\tilde{C}$ is the matrix with entries $\tilde{c}_{\ln} = \int \frac{\Psi_l^{j+1}(z)\Psi_n^j(z)}{\rho_{j+1}(z)}dz$ (3.32)

$\hat{C}$ is the matrix with entries $\hat{c}_{\ln} = \frac{k_{n,c}^j}{k_{l,c}^{j+1}} \int \frac{\Psi_l^{j+1}(z)\Psi_n^j(z)}{\rho_j(z)}dz$ (3.33)

The boundary condition as $r \to \infty$: $b_n^M = 0$ for $n = 1 \cdots N$; (3.34)

The source condition at $r = 0$: $a_n^1 = \frac{i}{4\rho(z_s)}\Psi_n(z_s)H_0^{(1)}(k_{n,c}^1 r_1) + b_n^1 \frac{H_0^{(1)}(k_{n,c}^1 r_1)}{H_0^{(2)}(k_{n,c}^1 r_1)}$ (3.35)

Combining (3.27), (3.34), and (3.35) yields all the a_n^j and b_n^j. Thus, Eq. (3.24) is the two-way coupled mode solution of range-dependent problem.

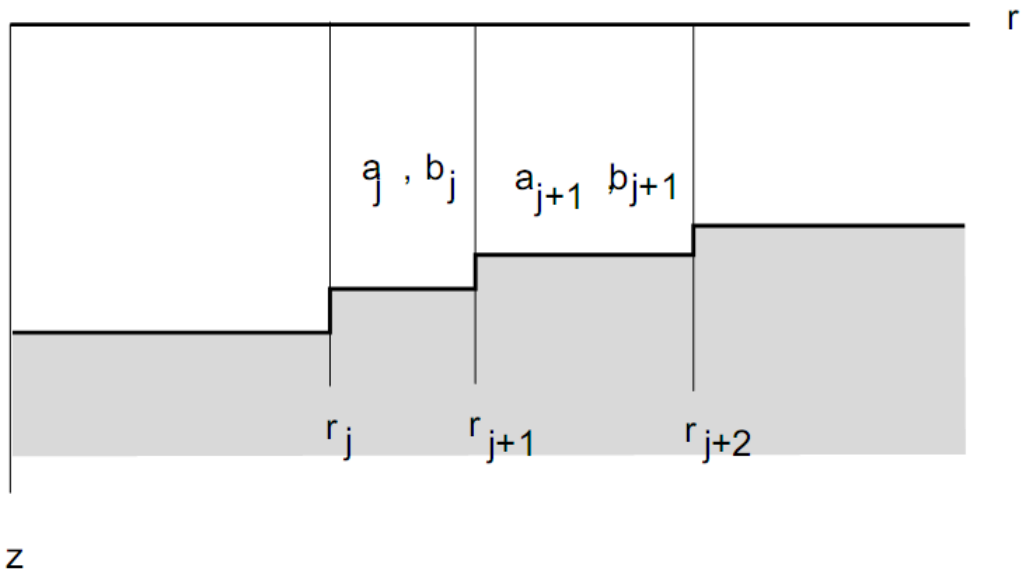

Figure 3.3 Segmentation for coupled mode formulation (Jensen *et al.*, 2000)

The full two-way coupled mode formulation can be simplified to the single scatter formulation which treats each interface in range as an independent process, thus neglecting the higher-order multiple-scattering terms (Jensen *et al.*, 2000). This approach is referred as the one-way coupled mode formulation. In the one-way coupled mode approach, the incoming wave in the left segment is assumed to be given, the solution is purely outgoing in the right segment, i.e. $b_n^{j+1} = 0$. Using Eq. (3.27), gives

$$b_n^j = -\left(R4_n^j\right)^{-1} R3_n^j a_n^j \text{ and } a_n^{j+1} = (R1_n^j - R2_n^j\left(R4_n^j\right)^{-1} R3_n^j)a_n^j$$

and the field in any given segment can be computed.

A range-dependent example is calculated by the one-way coupled mode method. The sound speed profiles of this range-dependent example are shown in figure 3.4. Sediment properties and bathymetry are range independent. The water depth is 75 m and the source depth is 50 m. The calculated TL for this range-dependent example is shown in Figure 3.5.

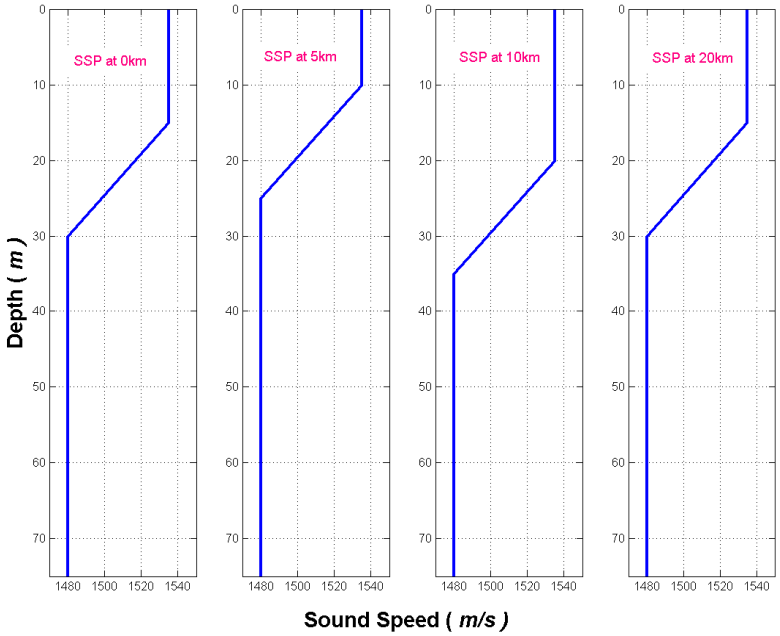

Figure 3.4 Sound speed profiles used in the range-dependent example

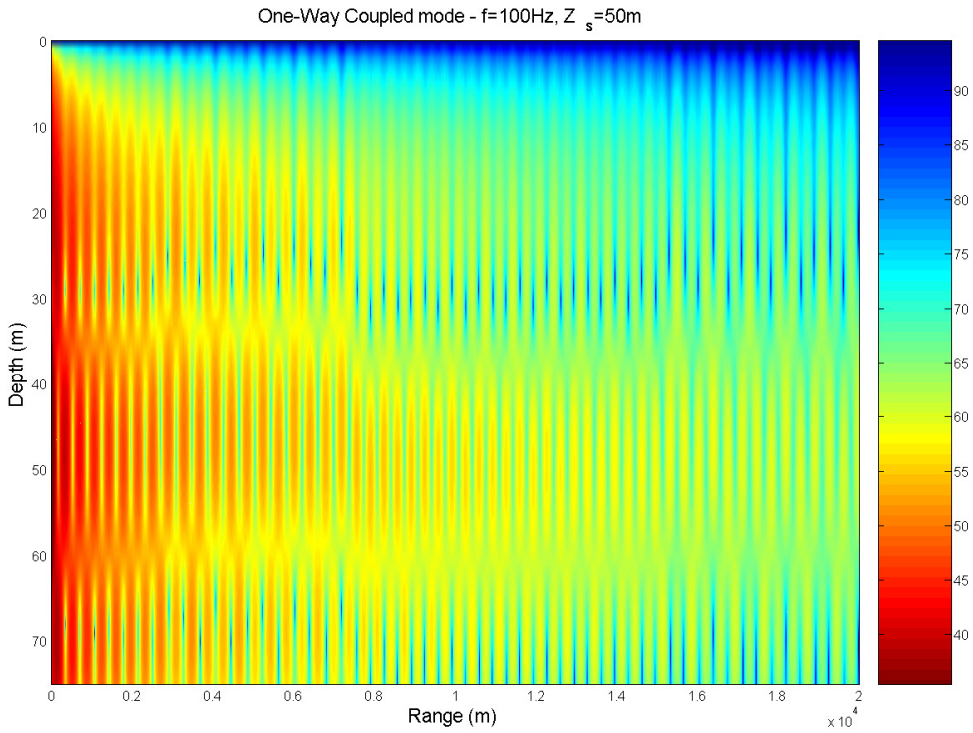

Figure 3.5 Transmission Loss using One-way coupled mode (100 Hz)

3.2 Parabolic Equation Method

The parabolic equation (PE) method (Leontovich and Fock, 1946; Fock, 1965; Tappert, 1977; Jensen *et al.* 1994) is used to find a marching type of solution for range-dependent sound propagation problems. Range dependence is handled by approximating the medium as a sequence of range-independent regions. In the PE method, it is assumed that outgoing energy dominates back-scattered energy. An outgoing wave equation is obtained by factoring the operator in the frequency-domain wave equation. Then, a function of an operator is approximated using a rational function to obtain an equation that can be solved numerically (Collins, 1997).

Starting from the Helmholtz equation,

$$\frac{\partial^2 p}{\partial r^2} + \frac{1}{r}\frac{\partial p}{\partial r} + \rho \frac{\partial}{\partial z}\left(\frac{1}{\rho}\frac{\partial p}{\partial z}\right) + k^2 p = 0 \tag{3.36}$$

where, $k^2 = \dfrac{\omega^2}{c^2(z)}$ is a complex wave number.

The second term $\left(\frac{1}{r}\frac{\partial p}{\partial r}\right)$ of the Helmholtz equation is neglected due to the far-field approximation. Thus, sound pressure p satisfies the following far-field equation in each range-independent region (Collins, 1993):

$$\frac{\partial^2 p}{\partial r^2} + \rho \frac{\partial}{\partial z}\left(\frac{1}{\rho}\frac{\partial p}{\partial z}\right) + k^2 p = 0 \tag{3.37}$$

Factoring the operator in eq. (3.37), yields

$$\left(\frac{\partial}{\partial r} + ik_0(1+X)^{1/2}\right)\left(\frac{\partial}{\partial r} - ik_0(1+X)^{1/2}\right)p = 0 \tag{3.38}$$

$$k_0^2 X = \rho \frac{\partial}{\partial z}\frac{1}{\rho}\frac{\partial}{\partial z} + k^2 - k_0^2 \tag{3.39}$$

where, $k_0 = \dfrac{\omega}{c_0}$ and c_0 is a representative phase speed.

The outgoing wave equation is then:

$$\frac{\partial p}{\partial r} = ik_0(1+X)^{1/2} p \tag{3.40}$$

The solution of the outgoing wave equation is

$$p(r+\Delta r, z) = \exp(ik_0 \Delta r(1+X)^{1/2})\, p(r,z) \tag{3.41}$$

where, Δr is the range step.

The exponential function in Eq. (3.41) is approximated by an n-term rational function. Thus, Eq (3.41) becomes

$$p(r+\Delta r,z)=\exp(ik_0\Delta r)\prod_{j=1}^{n}\frac{1+\alpha_{j,n}X}{1+\beta_{j,n}X}p(r,z) \tag{3.42}$$

Expanding the rational function in Eq. (3.42) by partial fractions, yields

$$p(r+\Delta r,z)=\exp(ik_0\Delta r)\left(1+\sum_{j=1}^{n}\frac{\gamma_{j,n}X}{1+\beta_{j,n}X}\right)p(r,z) \tag{3.43}$$

The product representation (3.42) is not as useful for computation as the equivalent sum presentation (3.43) because it does not permit parallel processing.

The Range-dependent Acoustic Model (RAM by Collins, 1997) is an efficient PE algorithm based on Eqs. (3.42) and (3.43). It is developed to solve the range-dependent sound propagation problems. A range-dependent example is calculated by RAM. In this example, sediment properties are range-independent. The sound speed profiles along track 1 of sub-experiment two in SW ’06 (see figure 3.6) and the bathymetric change along track 1 of sub-experiment two in SW ’06 (see figure 3.7) are used in the calculation. The source depth is 43 m. The calculated TL for this range-dependent example is shown in Figure 3.8.

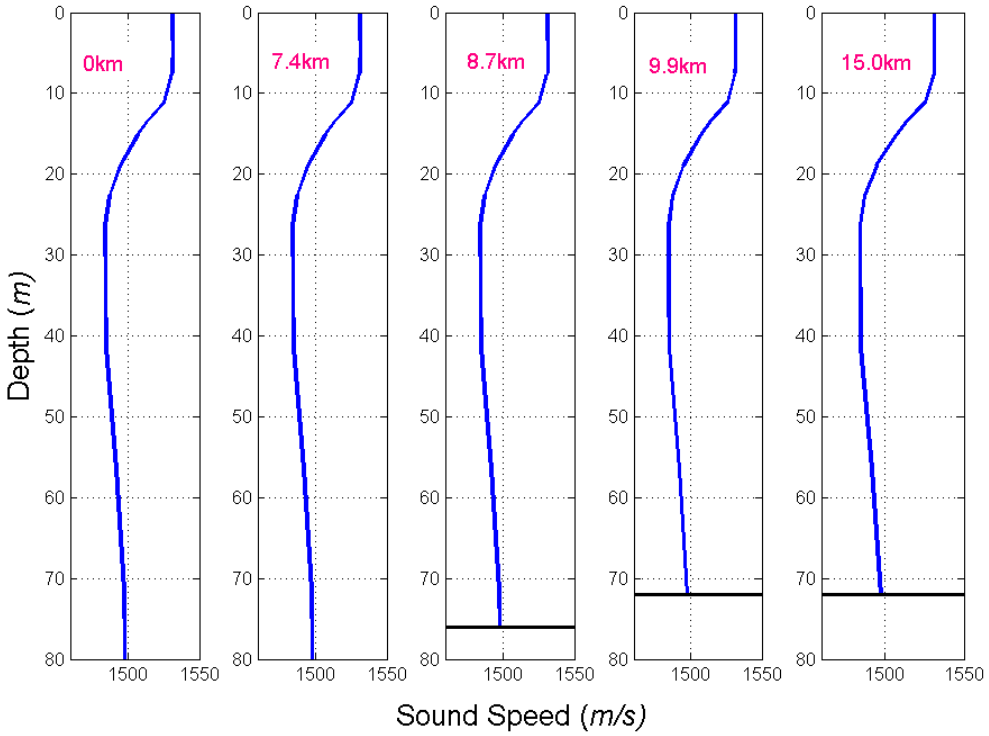

Figure 3.6 Sound speed profiles used in PE method

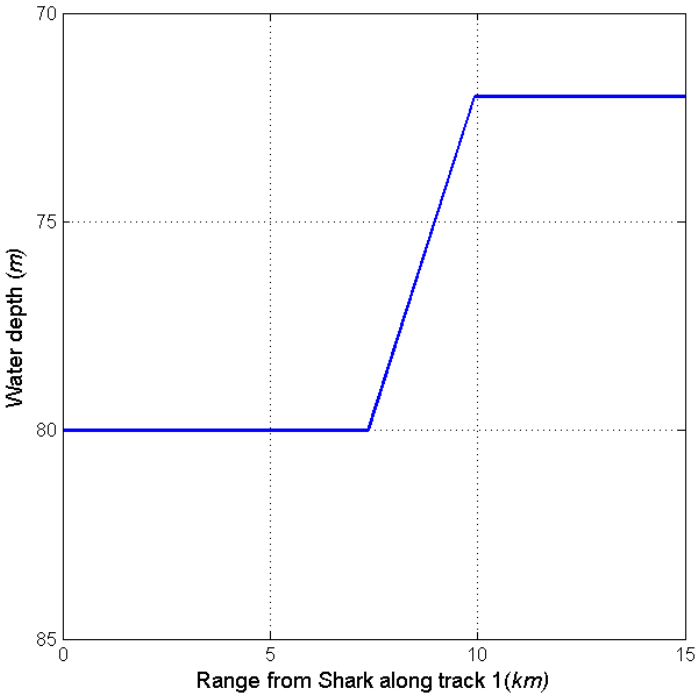

Figure 3.7 Bathymetric change used in PE method

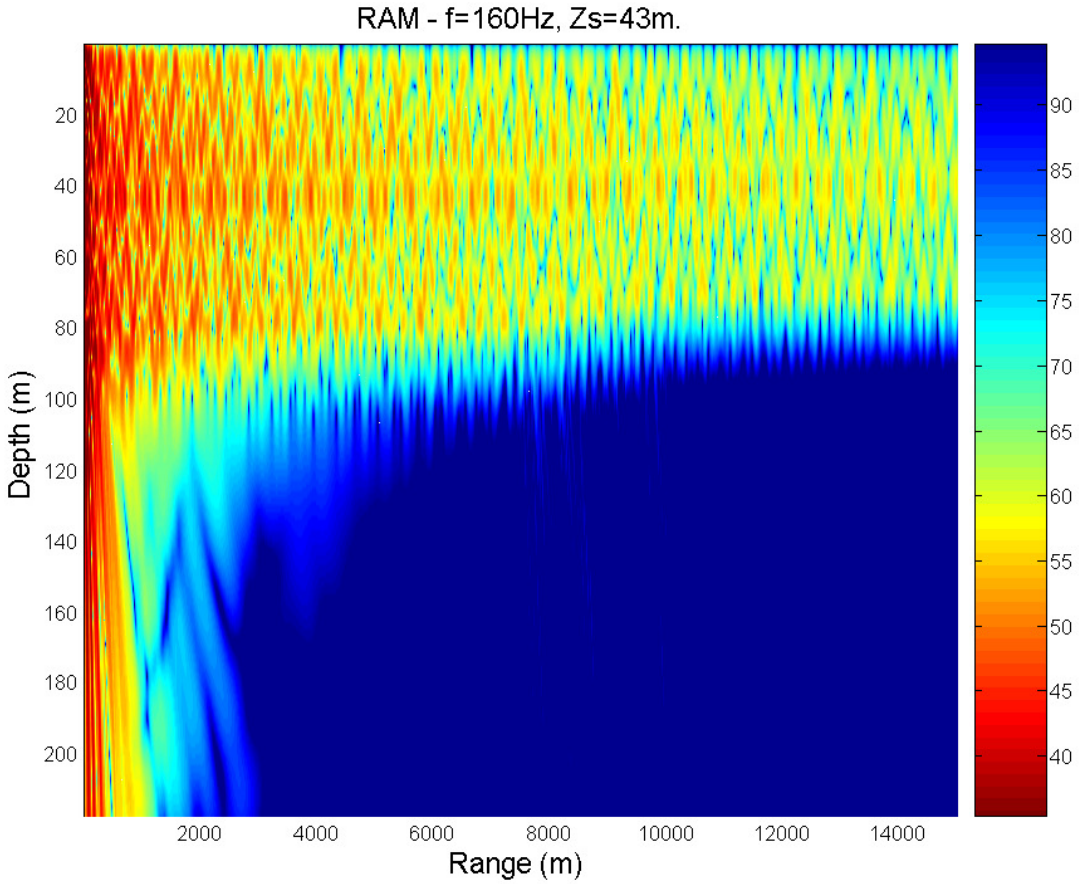

Figure 3.8 Transmission Loss using PE method (160 Hz)

CHAPTER 4

SEABED SOUND SPEED AND ATTENUATION INVERSION FOR THE YELLOW SEA '96 EXPERIMENT

4.1 Introduction

In this chapter: (1) modal characteristics of broadband explosive sound signals from YS '96 are analyzed; (2) Transmission loss as a function of range, frequency, and depth is obtained; (3) the results are used to obtained sound speed and attenuation in the seabottom by inversion.

The geo-acoustic properties of the seabottom are of great importance in determining how the seabottom influences sound propagation in the ocean. Researchers have developed many inversion techniques to estimate broadband seabottom sound speed and attenuation. These broadband inversion techniques involve dispersion analysis of broadband signals (Potty *et al.*, 2000 & 2003; Li *et al.*, 2007), measurements of modal attenuation coefficients (Ingenito, 1973; Zhou, 1985), measurements of modal amplitude ratios (Potty *et al.*, 2003; Tindle, 1982; Zhou *et al.*, 1987), *TL* measurements (Peng *et al.*, 2004; Rozenfeld *et al.*, 2001; Dediu *et al.*, 2007), broadband signal waveform matching (Li and Zhang, 2000; Knobles *et al.*, 2006 & 2008), matched field processing (Li and Zhang, 2004; Li *et al.*, 2004), vertical coherence of reverberation and propagation (Zhou *et al.*, 2004), and Hankel transform methods (Holmes *et al.*, 2006).

As discussed by Chapman (2001), inversion techniques are divided into two types. Inversions of the first type estimate the geophysical properties of the seabottom as precisely as possible and construct a true picture of the seabed layering and composition. Such detail however may be unnecessary for some sonar applications. The second type of

inversion seeks a simpler "effective seabed" model that is adequate for predicting the acoustic field. This research specifically considers the second type of inversion. In this chapter, only long-range propagation at frequencies in the 80-1000 Hz range is examined. Steep bottom-penetrating acoustic waves contribute little to the long-range acoustic field in the water. A site survey did not find any apparent layer structure in the bottom at the YS'96 site (Li *et al.*, 1991). Thus, a half-space bottom model (with an effective sound speed, attenuation and density) is used.

In this chapter, two inversion schemes are used to obtain the effective sound speed in the seabottom. The first scheme is based on normal mode depth functions, which are extracted from the cross-spectral density matrix (CSDM). The CSDM is defined by Eq.(4.1),

$$C = PP^H \tag{4.1}$$

where, P is the pressure matrix and P^H is the conjugate transpose of the matrix P. This extraction technique is accomplished without using numerical models to obtain solutions of a sound field and without *a priori* knowledge of the environment. This extraction approach has been discussed by Wolf *et al.* (1993), Neilsen and Westwood (2002), Hursky *et al.* (1995 & 2001), Smith (1997) and Badiey *et al.* (1994). In Wolf's paper, the source-receiver distance was fixed and the CSDM was formed by averaging the outer products of measured sound pressure spectra over multiple frequency bins in a narrow band. In Neilsen's paper, the source traversed a significant range interval and the CSDM was obtained by averaging over time. In Hursky's paper, the CSDM was constructed by using ambient noise from the ocean surface. In the present study, I use a method for extracting normal mode depth functions from broadband signals received by a

vertical line array at a fixed propagation distance from the explosive source. CSDM-derived mode depth functions have been used as a basis for further data analysis. The horizontal wave numbers and seabed sound speed are inverted by finding the best match between the extracted normal mode depth functions and the theoretical ones. The details of this estimation process are shown in section 4.2.

In the second scheme, the dispersion characteristics of normal modes are used to obtain the sound speed in the seabottom. The propagation of a broadband sound signal exhibits dispersion characteristics in shallow water. The group velocities differ for different frequencies and modes. This dispersion behavior has been successfully utilized for inversion of the geo-acoustic parameters (Potty *et al.*, 2000 & 2003; Li *et al.*, 2007). The dispersion characteristics of normal modes can be observed using time-frequency analysis of a broadband signal measured at sufficiently long range. The modal arrival times corresponding to various modes and frequencies can be extracted from these time-frequency distributions. Potty *et al.* (2000 & 2003) used the wavelet scalogram of the SUS signals to analyze the time-frequency behavior. Li *et al.* (2007) applied an adaptive optimal-kernel time-frequency representation technique (Jones and Baraniuk, 1995) to derive the dispersion characteristics of the normal modes from broadband acoustic signals excited by vacuum glass spheres. In this research, this time-frequency representation method is used to estimate the group velocity dispersion characteristics. The seabottom sound speed is inverted by matching the calculated group velocity dispersion curves with the experimental data.

The inverted seabottom sound speed obtained using the above two schemes is used as a constraint condition to estimate the sound attenuation in the seabottom by three

methods. The first method involves measurement of individual normal mode attenuation coefficients. Ingenito (1973) and Zhou (1985) have obtained the modal attenuation coefficients using individual normal mode amplitudes measured at different ranges. In this chapter, the seabottom attenuation is estimated by matching the measured modal attenuation coefficients of the first three modes with theoretical results. The second method is based on measured normal mode amplitude ratios. Tindle (1982), Zhou *et al.* (1987) and Potty *et al.* (2003) have used the measured normal mode amplitude ratios to determine the attenuation coefficient of the seabottom. A normal mode is largest when the receiver/source depth is close to a depth where the mode depth function has a maximum. In this research, the signal to noise ratio for a given mode is improved by evaluating the normal mode amplitude vs. range at a receiver depth appropriate for that mode. The measured amplitude ratios of the second, third and fourth modes to the first mode are compared with theoretical results to obtain the seabottom sound attenuation. In the third method, the seabottom sound attenuation is inverted by finding the best match between the measured and modeled broadband *TL*s as a function of frequency, range, and depth along two radial lines when receivers are located both above and below the thermocline.

The remainder of this chapter is organized as follows:

In Section 4.2, the inversion of seabed sound speed by matching measured and modeled modal depth functions is presented. In section 4.3, the seabed sound speed is estimated using measured modal arrival times. Then the sound attenuation in the seabed is estimated using measured modal attenuation coefficients (Section 4.4), measured normal mode amplitude ratios (Section 4.5), and *TL* data (Section 4.6).

4.2 Seabed Sound Speed Inverted from Data-derived Mode Depth Functions

4.2.1 Method

4.2.1.1 Construction of CSDM using measured pressure over multiple-frequency bins at a fixed source-receiver distance

The CSDM is constructed using data from the vertical line array which spans the whole water column. The approach to forming the CSDM in this thesis uses measured pressure spectra over multiple-frequency bins in a narrow band at a fixed source-receiver distance (Wolf *et al.*, 1993; Neilsen and Westwood, 2002).

According to the normal mode theory, the far field acoustic pressure excited by a harmonic point source is given by Eq. (3.16).

$$p(r,z) \approx \frac{i}{\rho(z_s)}\sqrt{\frac{1}{8\pi}}e^{(-i\pi/4)}\sum_{n=1}^{M}\Psi_n(z_s)\Psi_n(z)\frac{e^{ik_{n,c}r}}{\sqrt{k_{n,c}r}} \tag{3.16}$$

At a certain fixed source-receiver distance r_0, an $N_z - row$ by $N_f - column$ pressure matrix P is constructed .

$$P = \begin{bmatrix} p(z_1,f_1,r_0) & p(z_1,f_2,r_0) & \cdots & p(z_1,f_{N_f},r_0) \\ p(z_2,f_1,r_0) & p(z_2,f_2,r_0) & \cdots & p(z_2,f_{N_f},r_0) \\ \cdots & \cdots & \cdots & \cdots \\ p(z_{N_z},f_1,r_0) & p(z_{N_z},f_2,r_0) & \cdots & p(z_{N_z},f_{N_f},r_0) \end{bmatrix} \tag{4.2}$$

where, $z_1, z_2, \ldots, z_{N_R}$ are the receiver depths, N_Z is the total number of receivers, $f_1, f_2, \ldots, f_{N_f}$ are the frequencies of the multiple frequency bins in a narrow band. The bandwidth of the narrow band can be expressed as

$$B = f_{N_f} - f_1 \tag{4.3}$$

From Eq. (3.16), the *P* matrix can be expressed as a product of three matrices.

$$P = e^{i\pi/4}\overline{\Psi}\Lambda_f F \tag{4.4}$$

where

$$\overline{\Psi} = \frac{1}{\sqrt{\rho(z_s)}}\begin{bmatrix} \Psi_1(z_1) & \Psi_2(z_1) & \ldots & \Psi_M(z_1) \\ \Psi_1(z_2) & \Psi_2(z_2) & \ldots & \Psi_M(z_2) \\ \ldots & \ldots & \ldots & \ldots \\ \Psi_1(z_{N_z}) & \Psi_2(z_{N_z}) & \ldots & \Psi_M(z_{N_z}) \end{bmatrix}, \tag{4.5}$$

$$\Lambda_f = \sqrt{\frac{N_f}{8\pi\rho(z_s)r_0}}\begin{bmatrix} \Psi_1(z_s) & 0 & \ldots & 0 \\ 0 & \Psi_2(z_s) & \ldots & 0 \\ \ldots & \ldots & \ldots & \ldots \\ 0 & 0 & \ldots & \Psi_M(z_s) \end{bmatrix}, \tag{4.6}$$

$$F = \frac{1}{\sqrt{N_f}}\begin{bmatrix} \frac{e^{ik_{1,c}(f_1)r_0}}{\sqrt{k_{1,c}(f_1)}} & \frac{e^{ik_{1,c}(f_2)r_0}}{\sqrt{k_{1,c}(f_2)}} & \ldots & \frac{e^{ik_{1,c}(f_{N_f})r_0}}{\sqrt{k_{1,c}(f_{N_f})}} \\ \frac{e^{ik_{2,c}(f_1)r_0}}{\sqrt{k_{2,c}(f_1)}} & \frac{e^{ik_{2,c}(f_2)r_0}}{\sqrt{k_{2,c}(f_2)}} & \ldots & \frac{e^{ik_{2,c}(f_{N_f})r_0}}{\sqrt{k_{2,c}(f_{N_f})}} \\ \ldots & \ldots & \ldots & \ldots \\ \frac{e^{ik_{N_M,c}(f_1)r_0}}{\sqrt{k_{N_M,c}(f_1)}} & \frac{e^{ik_{N_M,c}(f_2)r_0}}{\sqrt{k_{N_M,c}(f_2)}} & \ldots & \frac{e^{ik_{N_M,c}(f_{N_f})r_0}}{\sqrt{k_{N_M,c}(f_{N_f})}} \end{bmatrix} \tag{4.7}$$

Thus, the cross-spectral density matrix *C* is given by

$$C = PP^H = \overline{\Psi}\Lambda_f FF^H {\Lambda_f}^H \overline{\Psi}^H \tag{4.8}$$

4.2.1.2 The relationship between singular value decomposition (SVD) of the CSDM and the normalized mode depth functions

The off-diagonal element of FF^H can be expressed by

$$D_{nm} = \sum_{j=1}^{N_f} \frac{1}{N_f \sqrt{k_n(f_j) k_m(f_j)}} \exp(i(k_n(f_j) - k_m(f_j)) r_0), \qquad (4.9)$$

where, $m \neq n$.

In this chapter, D_{nm} is assumed to be negligibly small at a sufficiently long range. The error caused by this assumption will be discussed in section 4.2.2. If $|D_{nm}|$ is approximately zero, Eq. (4.8) becomes

$$C = \overline{\Psi} \Sigma \overline{\Psi}^H \qquad (4.10)$$

where, $\Sigma = \Lambda_f F F^H \Lambda_f{}^H$. Σ is a matrix with nonnegative numbers on the diagonal and zeros off the diagonal.

In Eq. (4.10), the columns of $\overline{\Psi}$ are the orthogonal, normalized mode depth functions,

$$\int_0^D \frac{\Psi_m(z)\Psi_n(z)}{\rho(z)} dz + \int_D^\infty \frac{\Psi_m(z)\Psi_n(z)}{\rho_b(z)} dz = \delta_{mn} \qquad (4.11)$$

where D is the depth of the water column.

The second term in Eq. (4.11) is defined as

$$\sigma_{nm} = \int_D^\infty \frac{\Psi_m(z)\Psi_n(z)}{\rho_b(z)} dz \qquad (4.12)$$

The calculation in section 4.2.2 shows that σ_{nm} is close to zero and negligible. If σ_{nm} is approximately zero and the receivers span the whole water column and sufficiently sample the propagating modes in depth, then Eq. (4.12) can be rewritten as

$$\sum_{i=1}^{N_z} \frac{\Psi_m(z_i)\Psi_n(z_i)\Delta z_i}{\rho(z_i)} \approx \delta_{mn} \tag{4.13}$$

where N_z is the number of the receivers and Δz_i is the depth difference between $(i+1)^{th}$ and i^{th} receiver.

If the i^{th} row of $\overline{\Psi}$ in Eq. (4.5), and equivalently the i^{th} row of P in Eq. (4.2), are multiplied by $\sqrt{\Delta(z_i)}$, then Eq. (4.13) becomes

$$\overline{\Psi}^H \overline{\Psi} = \mathrm{I} \tag{4.14}$$

The CSDM, defined by Eq. (4.1), is obviously a Hermitian matrix. It can be decomposed by SVD (Horn and Johnson, 1991).

$$C = U\Sigma U^H \tag{4.15}$$

where, the columns of U are the orthonormal eigenvectors of C.

$$U^H U = \mathrm{I} \tag{4.16}$$

Comparing Eqs. (4.10) and (4.14) with Eqs. (4.15) and (4.16), researchers recognized that the eigenvectors of the CSDM obtained by SVD correspond to the mode shapes ($U = \overline{\Psi}$).

4.2.1.3 Algorithm for estimating seabottom sound speed

Jensen *et al*. have divided the water column into N equal intervals to construct a mesh of equally spaced points $z_i = ih$, i=0,1……N, where h is the mesh width given by

$h = D / N$ (see figure 4.1). Based on the finite difference mesh, a depth-separated finite difference wave equation can derived from Eq. (3.4)

$$\rho(z)\frac{d}{dz}\left(\frac{1}{\rho(z)}\frac{d\Psi(z)}{dz}\right)+\left(\frac{\omega^2}{c^2(z)}-k_c^2\right)\Psi(z)=0 \tag{3.4}$$

If the density in the water column is constant, Eq. (3.4) becomes

$$\frac{d^2\Psi(z)}{dz^2}+\left(\frac{\omega^2}{c^2(z)}-k_c^2\right)\Psi(z)=0 \tag{4.17}$$

Starting with the Taylor series expansion, the forward and backward difference approximations for the first derivative are obtained.

Forward: $$\frac{d\Psi(z_j)}{dz}\approx\frac{\Psi(z_{j+1})-\Psi(z_j)}{h} \tag{4.18}$$

Backward: $$\frac{d\Psi(z_j)}{dz}\approx\frac{\Psi(z_j)-\Psi(z_{j-1})}{h} \tag{4.19}$$

Adding Eq. (4.18) and Eq. (4.19) yields the centered difference approximation to the second derivative,

$$\frac{d^2\Psi(z_j)}{dz^2}\approx\frac{\Psi(z_{j-1})-2\Psi(z_j)+\Psi(z_{j+1})}{h^2} \tag{4.20}$$

Using Eqs. (4.17) and (4.20) yields the depth-separated finite difference wave equation

$$\Psi(z_{j+1})=-\Psi(z_{j-1})+\left\{2-h^2\left[\frac{\omega^2}{c^2(z_i)}-k_n{}^2\right]\right\}\Psi(z_j) \tag{4.21}$$

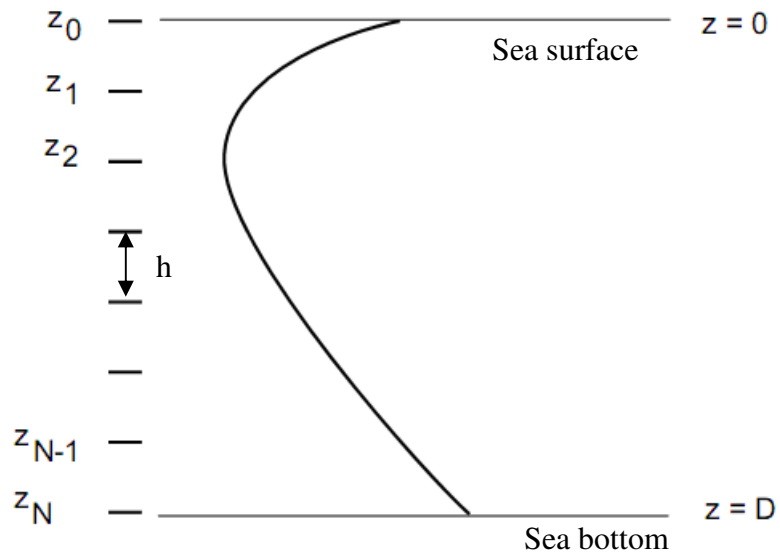

Figure 4.1 Finite-difference mesh (Jensen *et al*., 2000)

Given ssp in the water column and two initial values for $\Psi(0)$ and $\Psi(h)$, the mode depth functions from the sea surface to the seabed can be calculated for all values of wave number k_n by Eq. (4.21). This is called the shooting method (Hursky, 2001). The particular wave number k_n, which corresponds to the data-derived mode, is obtained by seeking a minimum of the cost function

$$\mathrm{F}(k_n) = \sqrt{\sum_{i=1}^{N} (\hat{\Psi}_n(z_i) - \Psi_n(z_i, k_n))^2} \tag{4.22}$$

where $\hat{\Psi}_n(z_i)$ is the nth data-derived mode.

In the shooting method, the mode that matches the data-derived mode is produced without knowing the seabed properties.

The boundary condition at the seabottom is satisfied by matching the impedance of the half-space bottom model with the impedance calculated from the mode depth functions obtained by this shooting method. The seabottom sound speed corresponding to

the mode that best matches the data-derived mode is selected. A detailed description of this estimation process is shown in figure 4.2.

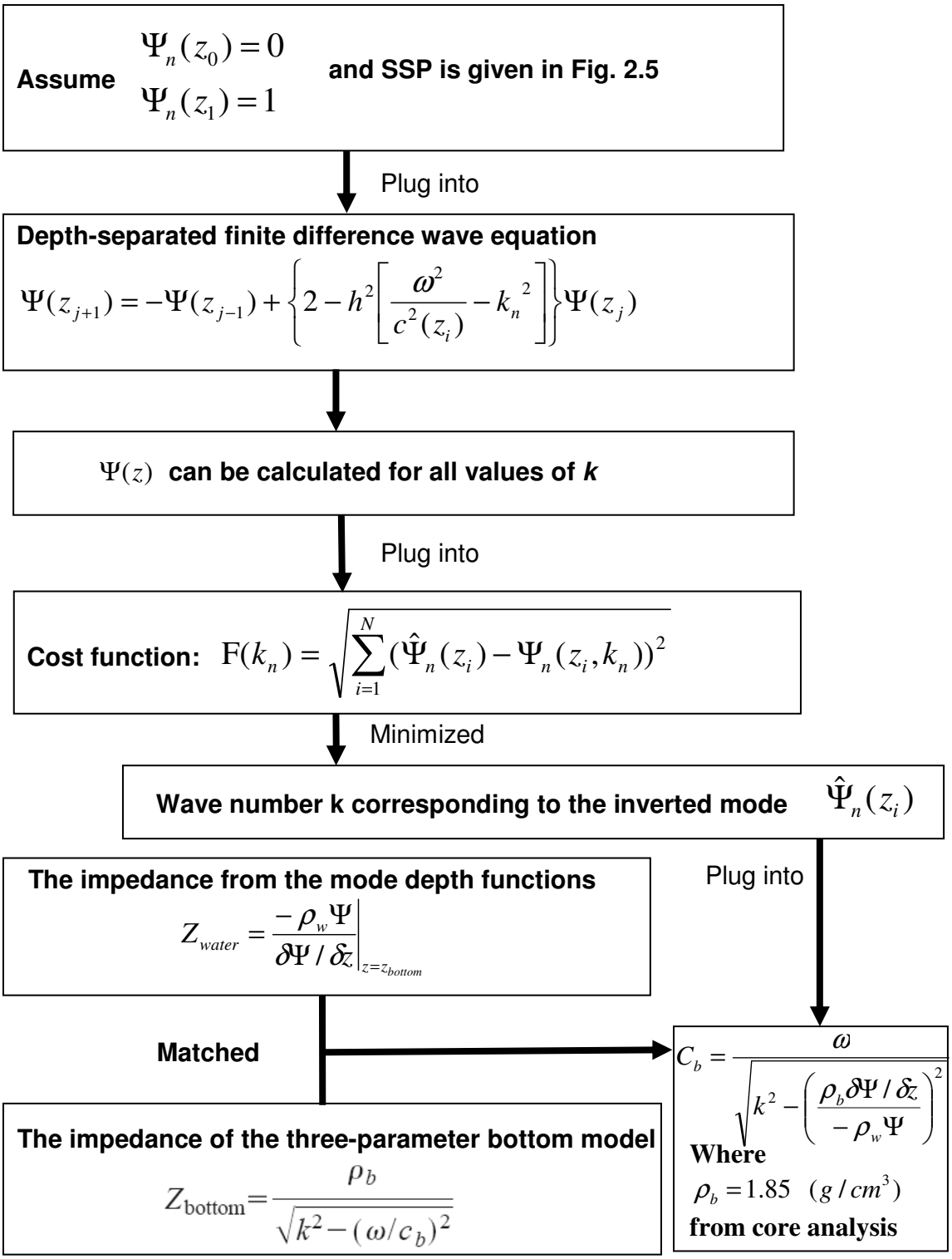

Figure 4.2 Estimation process for obtaining seabed sound speed using data-derived mode shape

4.2.2 Estimation of seabed sound speed using simulated data

In order to predict how this estimation process works with experimental data, simulated sound fields were generated using KRAKEN. The input seabed sound speed for KRAKEN was 1588 m/s and other input parameters, including the sound speed profile in water column, water depth (75 m), source depth (50 m), seabed density ($1.85 g/cm^3$), are the same as those measured in the YS '96 experiment. Thus, the simulations reflect realistic experimental conditions.

The simulated sound fields, containing noise (SNR=10dB), are used to form the CSDM. Sound pressure fields from 70 Hz to 130 Hz with a frequency step of 1.5 Hz are calculated and the sound pressure matrix P (Eq. 4.2) with 41 columns is constructed. Using Eq. (4.1), the simulated CSDM is obtained. Mode extraction from CSDM depends on the distance between the source and the receiver array. The effect of the distance on the inverted mode shapes is studied. In figures 4.3-4.5, black solid lines represent the first mode shape from KRAKEN. Red circles in figures 4.3, 4.4, and 4.5 represent the derived first mode shapes from the SVD of CSDM obtained at distances of 16.0 km, 26.7 km, and 53.5 km respectively. These figures show that as the distance increase, the mode shape from the SVD of CSDM improves. In figure 4.6, the difference between the mode shape from KRAKEN and from the SVD of CSDM as a function of distance is shown. The difference is decreased with increasing range. Based on the derived mode shapes from the SVD of CSDM in figures 4.3-4.5, the inverted bottom sound speed is obtained by the shooting method at three ranges (16.0 km, 26.7 km, and 53.5 km) and listed in Table 4.1. The results in Table 4.1 show that the inverted sound speed is 1584.5 m/s with an error of

3.5 m/s at 53.5 km. Therefore, our simulation indicates that the process of estimating seabed sound speed shown in Fig. 4.2 is reliable at a distance of 53.5 km.

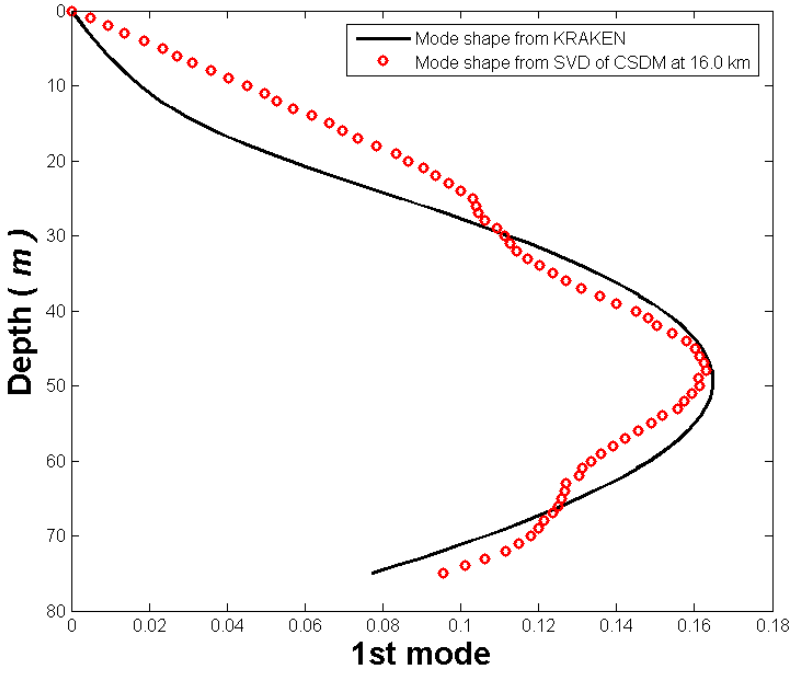

Figure 4.3 Comparison of the first mode shape at 16.0 km

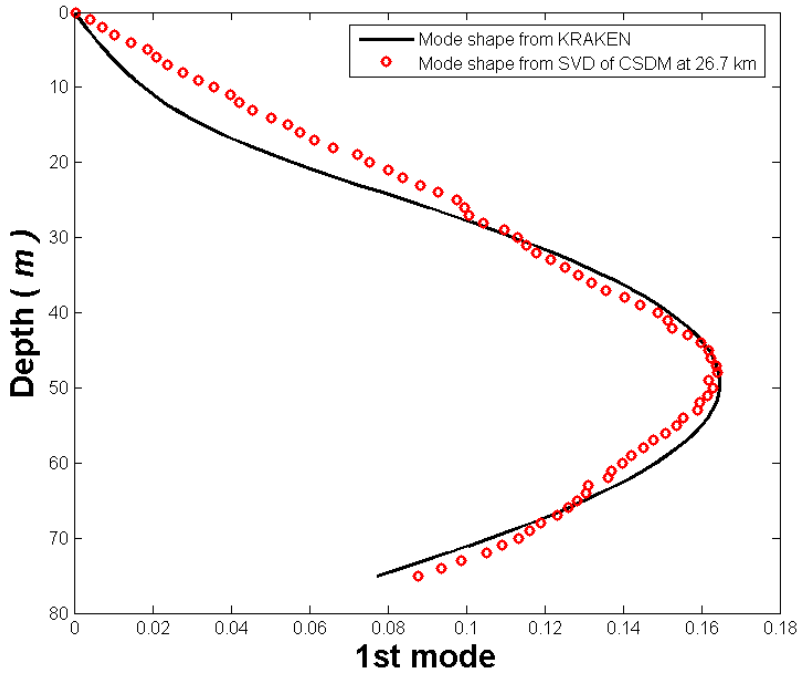

Figure 4.4 Comparison of the first mode shape at 26.7 km

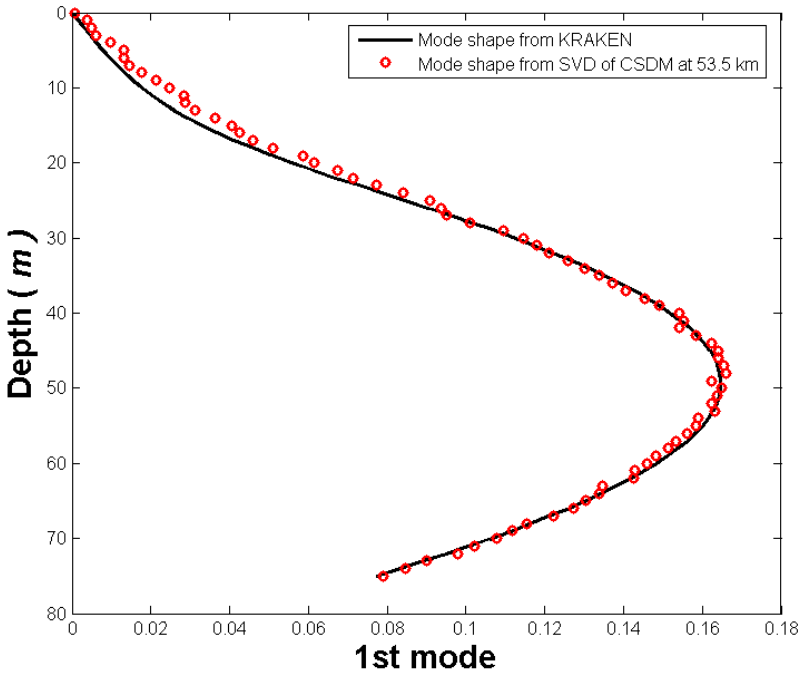

Figure 4.5 Comparison of the first mode shape at 53.5 km

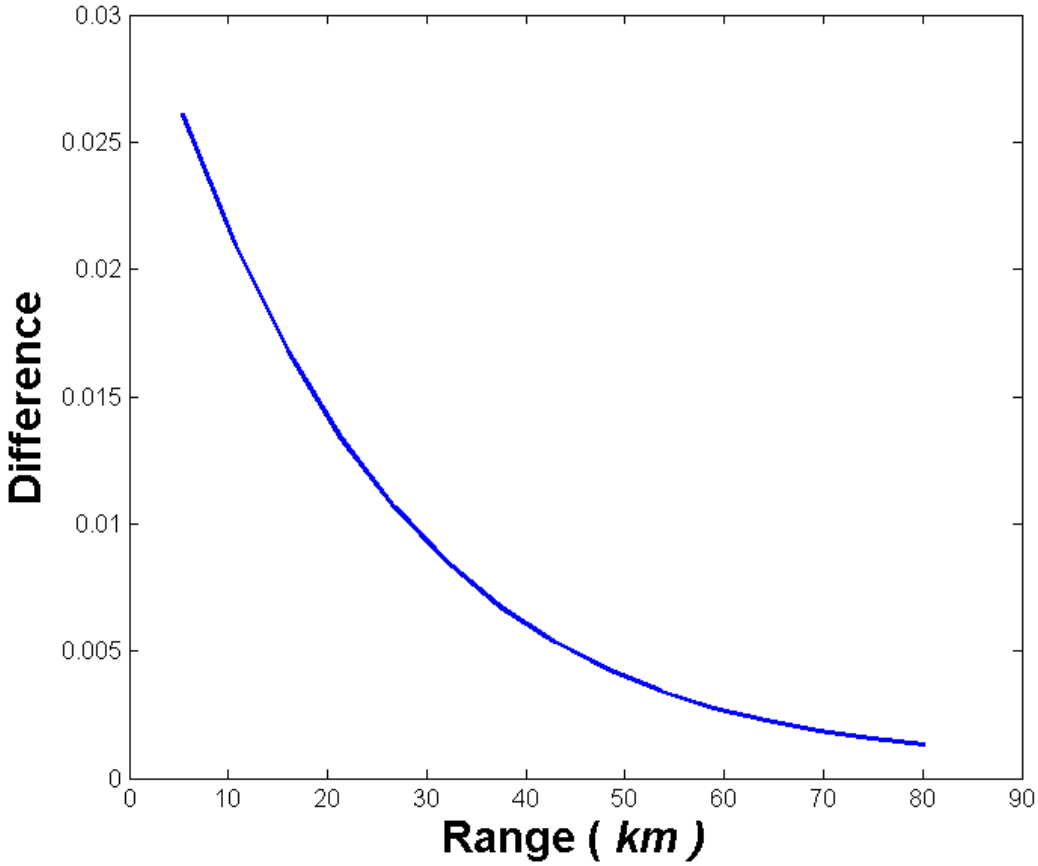

Figure 4.6 Difference between the mode shape from KRAKEN and from SVD of the CSDM

Table 4.1 Seabottom sound speed inverted from simulated data

Range	Inverted Bottom Sound Speed	Input Bottom Sound Speed	Estimation Error
16.0km	1572.7m/s	1588m/s	-15.3m/s
26.7km	1578.4m/s	1588m/s	-9.6m/s
53.5km	1584.5m/s	1588m/s	-3.5m/s

The errors shown in Table 4.1 are mainly caused by two assumptions. First, the magnitude of D_{nm}, defined by Eq. (4.9), is assumed to be negligibly small at sufficiently long range. Second, σ_{nm}, defined by Eq. (4.12), is approximately zero, and the receivers span the whole water column so that the orthogonality condition, Eq. (4.13), is satisfied.

Based on the simulated sound field, the magnitude of D_{nm} is calculated and listed in Table 4.2. The calculation results show that the estimation error caused by the first assumption is less than 3.5m/s at 53.5km.

Table 4.2 Magnitude of D_{nm} at 16.0km, 26.7km and 53.5km

Range (r_0)	$\lvert D_{12}\rvert$	$\lvert D_{13}\rvert$	$\lvert D_{23}\rvert$	$\lvert D_{12}\rvert+\lvert D_{13}\rvert+\lvert D_{23}\rvert$	Estimation Error
16.0km	0.14	0.16	0.21	0.51	-15.3m/s
26.7km	0.08	0.09	0.14	0.31	-9.6m/s
53.5km	0.08	0.18	0.02	0.28	-3.5m/s

The calculated group velocities, wave numbers and modal attenuation coefficients (β_n) for the three modes at 100 Hz are listed in Table 4.3 (there are only three propagating modes at 100 Hz).

Table 4.3 Group velocities, wave numbers and modal attenuation coefficients at 100Hz

Mode(n)	1	2	3
V_n (m/s)	1475.9	1464.6	1447.2
k_n (m^{-1})	0.425570	0.416092	0.405712
β_n (m^{-1})	6.46×10^{-6}	19.7×10^{-6}	38.5×10^{-6}

The normal-mode attenuation coefficient for the n[th] mode can be expressed by the integrals (Koch *et al.*, 1983).

$$\beta_n = \frac{\omega}{k_n}\int_D^{\infty}\frac{\alpha_b}{c_b}\rho_b\Psi_n^2(z)dz + \frac{\omega}{k_n}\int_0^{D}\frac{\alpha}{c}\rho\Psi_n^2(z)dz \tag{4.23}$$

where α_b is the sound attenuation in the seabottom, and α is the sound attenuation in water column.

The normal-mode attenuation coefficient due to seabottom attenuation can be expressed by the first integral in Eq. (4.23). Comparing Eq. (4.12) and the first integral in Eq. (4.23), the relations between $\sigma_{nm}(n=m)$ and modal attenuation coefficients are obtained.

$$\beta_n > \frac{\omega}{k_n}\frac{\alpha_b}{c_b}\rho_b^2 \times \sigma_{nn} \tag{4.24}$$

$$\text{where } \sigma_{nn} = \int_D^{\infty}\frac{\Psi_n^2(z)}{\rho_b}dz \tag{4.25}$$

Substituting the wave numbers and modal attenuation coefficients at 100 Hz listed in Table 4.3 into Eq. (4.24), yields

$\sigma_{11} < 0.00039$, $\sigma_{22} < 0.0012$, and $\sigma_{33} < 0.0022$.

$$\text{Since, } \sigma_{mn}(n \neq m) \leq \max\{\sigma_{mm}, \sigma_{nn}\} \tag{4.26}$$

$\sigma_{12} < 0.0012$, $\sigma_{13} < 0.0022$ and $\sigma_{23} < 0.0022$

The calculation results show σ_{nm} is close to zero and negligible at 100 Hz.

4.2.3 Estimation of seabed sound speed using experimental data from YS '96

4.2.3.1 Mode extraction from vertical line array data

Before applying the mode extraction technique to the Yellow Sea '96 experiment, the appropriateness of the experimental setup is examined. The 32-element vertical line array in the Yellow Sea '96 experiment spanned nearly the entire water column with negligible array tilt and sufficiently dense element spacing. The water depth was 75 m and the array spanned the depths between 4 m and 68 m with a spacing of 2 m (See figure 2.4). Thus, the data from the 32-element vertical line array can be used to construct the CSDM. In this chapter, the bandwidth B is selected to be 60 Hz and the central frequency is selected to be 100Hz. There are 41 frequency bins within the bandwidth B. As discussed in section 4.2.2, the fixed source-receiver distance r_0 should be appropriately chosen for good mode extraction results. In our data processing, r_0 is chosen to be 53.5 km on the QA track, and seven explosive signals with a source depth of 50 m were measured by the 32-element vertical line array to form the CSDM. The eigenvectors of the CSDM correspond to the mode depth function. The extracted depth function for mode one is shown in Fig. 4.7b by circles. The error bars in Fig. 4.7b show the standard deviations of the extracted mode shape at different receiver depths.

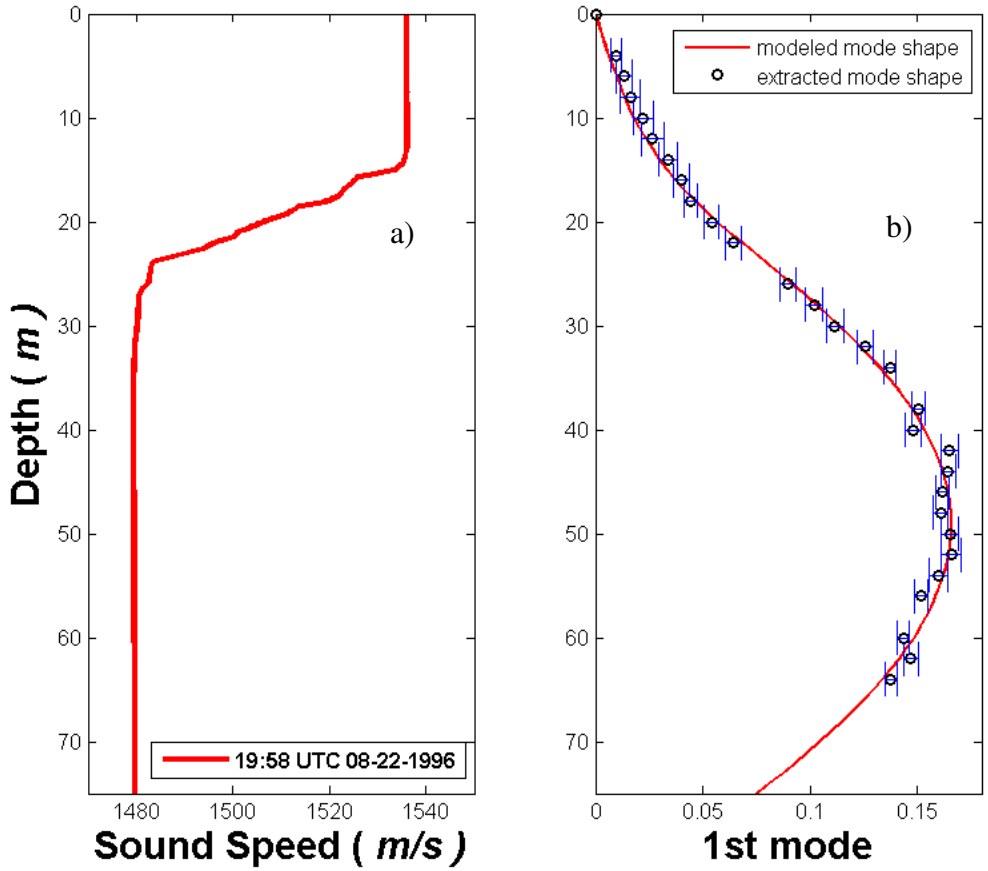

Figure 4.7 Comparison of extracted and modeled first mode shape (100Hz)

4.2.3.2 Results of the CSDM-inverted seabottom sound speed

The SSP used in the shooting method was measured at almost the same time as the data used for the mode extraction. For example, the SSP shown in Fig. 4.7a was measured at 19:58 UTC on August 22, 1996. That SSP was used in the shooting method to process the broadband explosive data measured at 19:53 UTC on August 22, 1996. A one-to-one correspondence was achieved between the extracted mode and the modeled mode obtained by the shooting method. The cost function is calculated for seven broadband explosive signals measured at a distance of 53.5 km. As an example, the cost

function of the first signal for the first mode as a function of seabed sound speed at 100 Hz is shown in figure 4.8. The inverted seabed sound speed at 100Hz for the first signal is 1603.4 m/s at the minimum point of the cost function *F*. The CSDM-inverted seabed sound speed and the corresponding wave number for mode one at 100 Hz are listed in Table 4.4. Thus, the averaged inverted seabed sound speed (C_b) is $1593 \pm 15 m/s$, and the corresponding wave number for mode one at 100 Hz is 0.422561 ± 0.000039. The modeled first mode shape with a seabed sound speed of 1593 m/s at 100 Hz, calculated by the shooting method, is shown in figure 4.7b by a solid line. The modeled shape is in good agreement with the extracted one obtained by averaging seven broadband explosive signals.

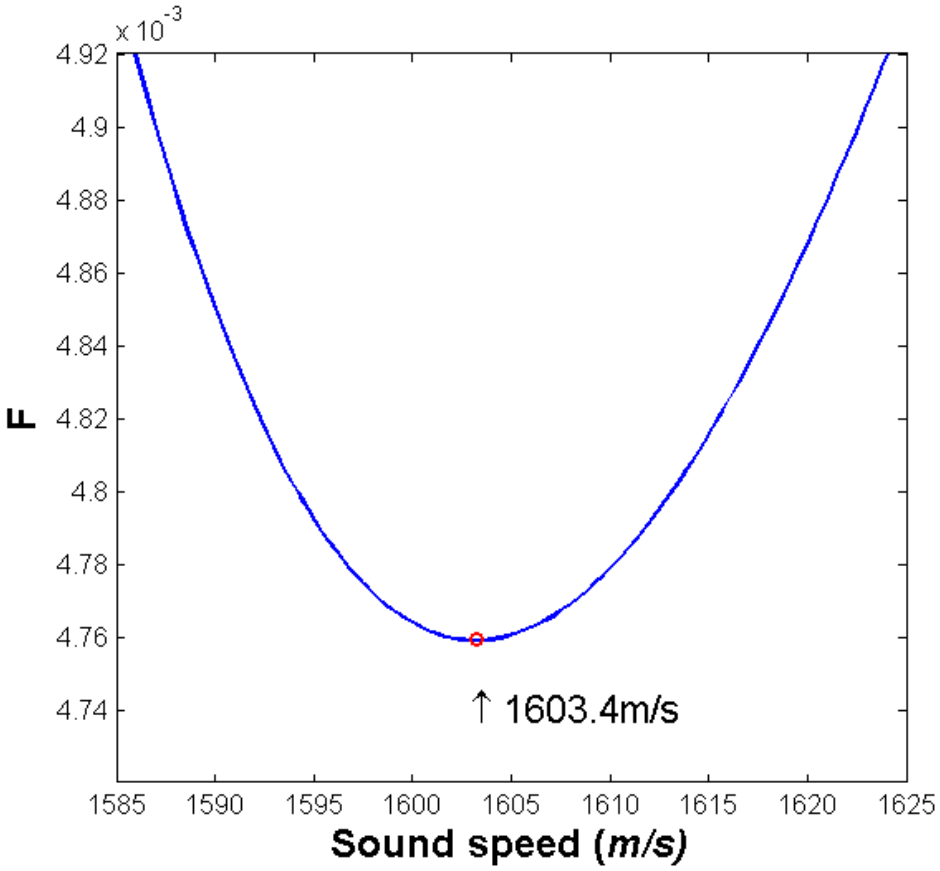

Figure 4.8 F as a function of seabed sound speed at 100 Hz

Table 4.4 Inverted results from YS '96 experimental data

Signal number	Inverted Bottom Sound Speed (*m/s*)	Inverted Wave Number
1	1603.4	0.4225355
2	1601.2	0.4225382
3	1611.5	0.4226174
4	1601.2	0.4226138
5	1575.2	0.4225310
6	1569.8	0.4225652
7	1589.7	0.4225688

4.3 Seabed Sound Speed Inverted from Measured Modal Arrival Times

4.3.1 Method

In a shallow water wave guide, for an impulsive signal of a given frequency, each mode has a distinct group velocity. The group velocity of the nth mode V_g^n is defined by

$$V_g^n = \frac{d\omega}{dk_n} \tag{3.19}$$

The group velocity of the nth mode also satisfies (Koch *et al.,* 1983)

$$\frac{1}{V_g^n} = \frac{\omega}{k_n}\int_0^\infty \frac{\rho(z)}{c^2(z)}\left|\Psi_n(z)\right|^2 dz \tag{4.27}$$

The modal group velocity varies with frequency. The arrival time difference between two frequencies for the nth mode at range *r* is given by

$$\Delta T_n(f) = [1/V_g^n(f) - 1/V_g^n(f_H)]r = K_{tn}(f)r \tag{4.28}$$

At a given distance *r,* for the same frequency, the arrival time difference between mode *n* and mode *m* is given by

$$\Delta T_{nm}(f) = [1/V_g^m(f) - 1/V_g^n(f)]r = K_{tmn}(f)r \tag{4.29}$$

where f_H is the reference frequency, which is higher than *f*. K_{tn} and K_{tmn} are the group slowness differences.

The experimental arrival time difference ($\Delta T_n^{'}$ and $\Delta T_{nm}^{'}$) at a range *r* and the experimental group slowness differences ($K^{'}_{tn}$ and $K^{'}_{tmn}$) can be extracted from time-frequency representation of the broadband experimental signals. The widely used short-time Fourier transform time-frequency representation is produced by taking the Fourier transform of broadband signals over a fixed time window. However, the resolution of the short-time Fourier transform time-frequency representation is limited by a user specified window length. The continuous wavelet transform provides a different approach to time-frequency analysis. However, wavelet analysis does not give good frequency resolution at higher frequencies. In this research, an adaptive optimal-kernel time-frequency representation (AOK TFR) based on a signal-dependent radially Gaussian kernel is used. Since this time-frequency representation adapts its kernel to each set of signal components, it resolves the fine detail more sharply than the short-time Fourier transform time-frequency representation or wavelet analysis (Marple *et al*., 1993). Details of the adaptive optimal-kernel time-frequency representation algorithm can be found in Jones and Baraniuk's paper (1995).

If the water column SSP and the seabottom density are known, the seabottom sound speed can be inverted by matching the calculated group slowness differences (K_{tn} and K_{tmn}) with their experimental values ($K^{'}_{tn}$ and $K^{'}_{tmn}$) (Zhou *et al.* 1985, 1987). The inverted seabottom sound speed is obtained by seeking a minimum of the cost function

$$L(c_b, f) = \sqrt{\sum_n (K^{'}_{tn}(f) - K_{tn}(f, c_b))^2 + \sum_{m,n(m\neq n)} (K^{'}_{tmn}(f) - K_{tmn}(f, c_b))^2} \qquad (4.30)$$

This estimation process is shown in figure 4.9.

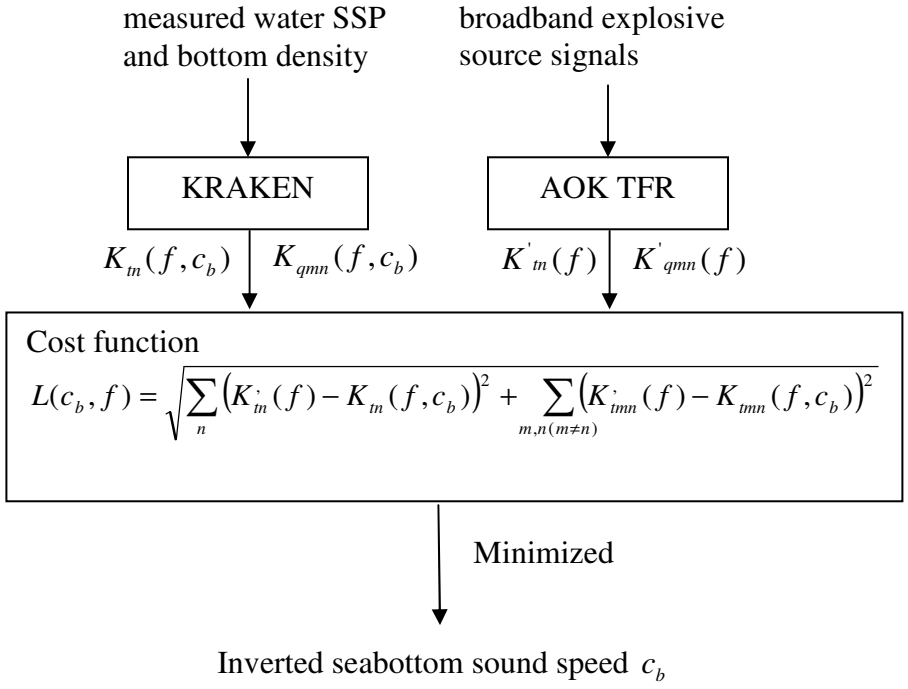

Figure 4.9 Estimation process of seabed sound speed using measured modal arrival time

4.3.2 Experimental Results

4.3.2.1 Time-frequency representation of the broadband signals in YS '96

Figure 4.10a shows the measured time series at a distance of 12.86 km when the 38g TNT source depth (SD) is 50 m and the receiver depth (RD) is 50 m. Figure 4.9b shows the measured time series at a distance of 36.72 km when the 38g TNT source depth is 50 m and the receiver depth is 66 m. The time series in Fig. 4.10a and Fig. 4.10b are processed using a standard AOK TFR program and the results are shown in Fig. 4.11a and Fig. 4.11b, respectively.

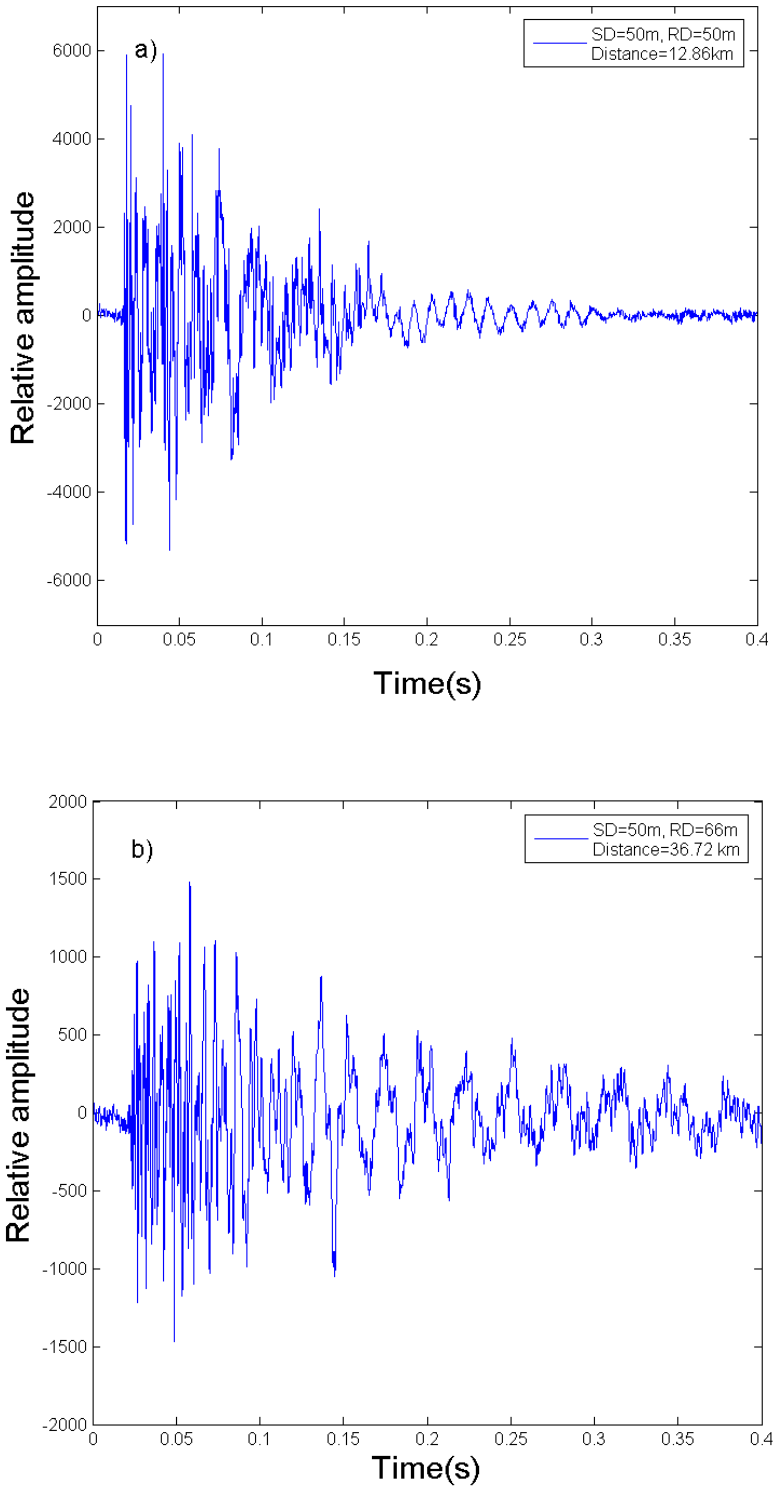

Figure 4.10 Time series of broadband explosive signals: a) at a distance of 12.86 km. b) at a distance of 36.72 km.

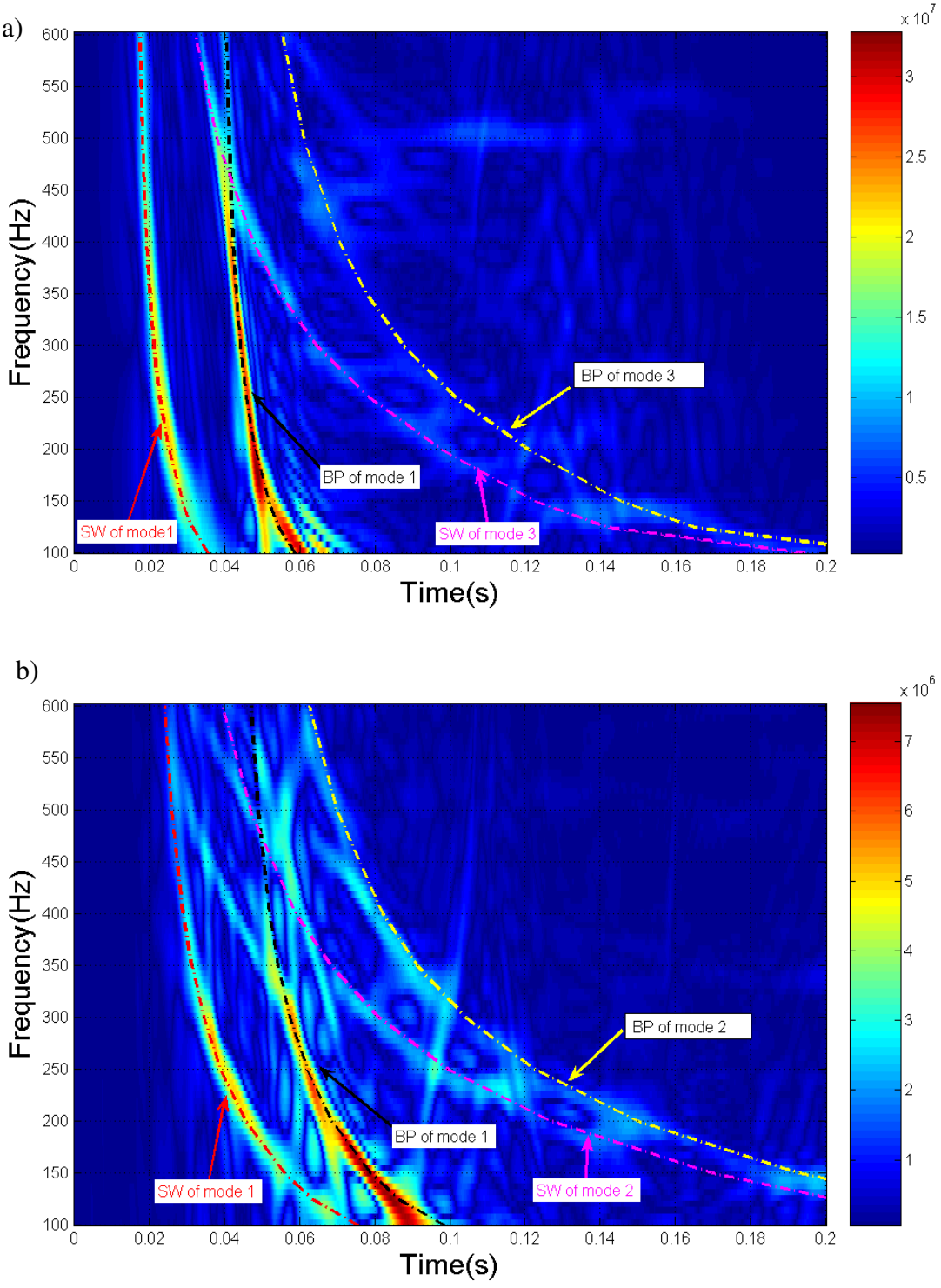

Figure 4.11 Comparison of extracted and calculated dispersion curves: a) at a distance of 12.86 km (RD=50 m); b) at a distance of 36.72km (RD=66 m).

In figure 4.11a, at a receiver depth of 50 m, the time-frequency representation of the shock waves (SWs) and bubble pulses (BPs) of the first mode and the third mode are seen to have a relatively high resolution in both the time and frequency domains. The time difference between the shock wave and the bubble pulse is approximately 0.023 s for a 38g TNT source exploding at a depth of 50 m (Urick, 1983). The second mode can not be identified. By way of explanation, figure 3.1 shows the four normal mode shapes at 200 Hz for the YS '96 experimental environment. It can be seen from figure 3.1 that the magnitude of the second mode is near its null at a depth of 50 m, while the magnitude of the first mode and third mode are near their maxima. Figure 4.11b shows that the shock waves and bubble pulses of the first and the second mode are separated and easily identified at a receiver depth of 66 m. The intensity of the second mode was enhanced, because the magnitude of the second mode is almost at its maximum at a depth of 66 m.

4.3.2.2 Results of the TFR-inverted seabottom sound speed

The average group slowness differences K'_{tmn} as a function of frequency, extracted from 25 experimental signals at different distances by using time-frequency representation, are listed in Table 4.5. In our data processing, the dispersion curve below 100Hz is not used, because the shock wave arrivals and the bubble pulse arrivals can not be temporally resolved below 100Hz. The parameter K'_{t1}, defined by Eq. (4.28) between 150Hz and 600Hz, is $0.8555\times10^{-6} s/m$. Inputting K'_{tn} and K'_{tmn} into Eq. (4.30), the cost $L(c_b)$ as a function of seabed sound speed is obtained. For example, figure 4.12 shows the cost $L(c_b)$ as a function of seabed sound speed at 200 Hz. The inverted seabed sound speed at 200 Hz is 1576 m/s at the minimum point of the cost function *L*.

The averaged inverted seabed sound speed is $1587 \pm 15 m/s$ over a frequency range from 150Hz to 400 Hz. The theoretical group velocity dispersion curves are calculated by KRAKEN and are shown in figure 4.11 by dashed lines. The calculated curves show good agreement with the extracted ones obtained by time-frequency representation of the broadband explosive signals.

Table 4.5 Extracted group slowness differences (YS '96)

f (Hz)	200	250	300	350	400
K'_{t12} (s/m)	2.2138×10^{-6}	1.5500×10^{-6}	1.1844×10^{-6}		
K'_{t13} (s/m)	5.5563×10^{-6}	4.3436×10^{-6}	3.4228×10^{-6}	2.7383×10^{-6}	2.1750×10^{-6}

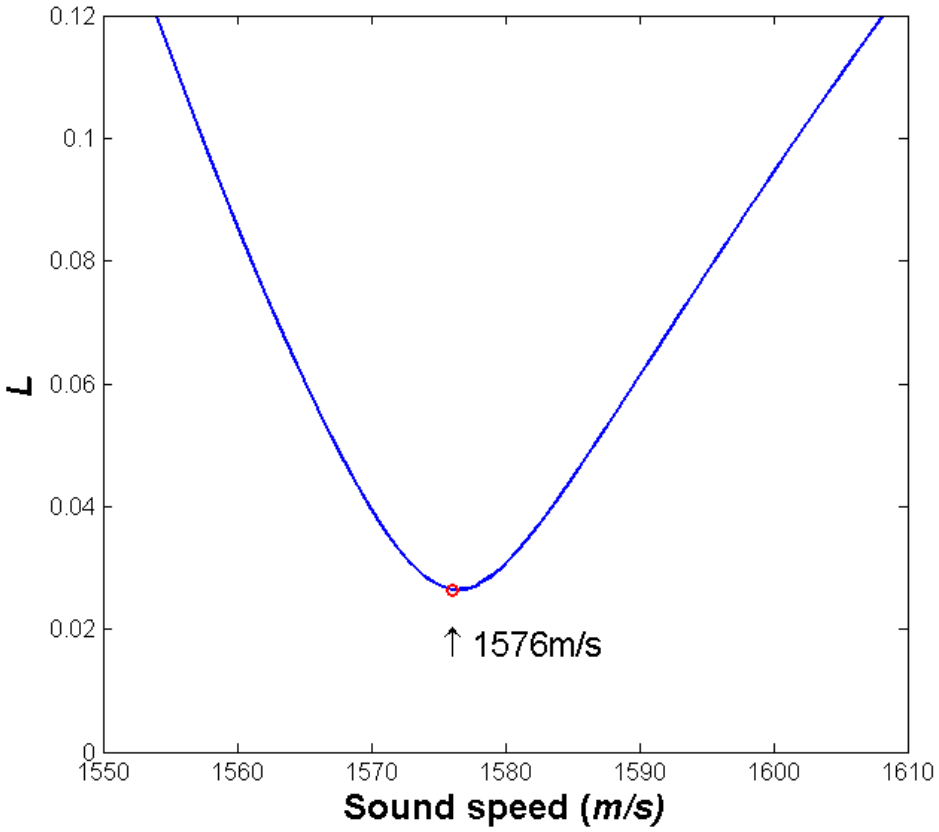

Figure 4.12 L as a function of seabed sound speed at 200 Hz

The inverted seabottom sound speed from the CSDM-based inversion and the dispersion-based inversion as a function of frequency are listed in Table 4.46 and shown in figure 4.13. The average inverted seabottom sound speed is 1588 m/s, which is used as a constraint condition for seabed attenuation inversion in Sec. 4.4, Sec. 4.5 and Sec. 4.6.

Table 4.6 Inverted seabed sound speed as a function of frequency (YS '96)

f (Hz)	100	150	200	250	300	350	400
C_b (m/s)	1593	1581	1576	1582	1592	1614	1576

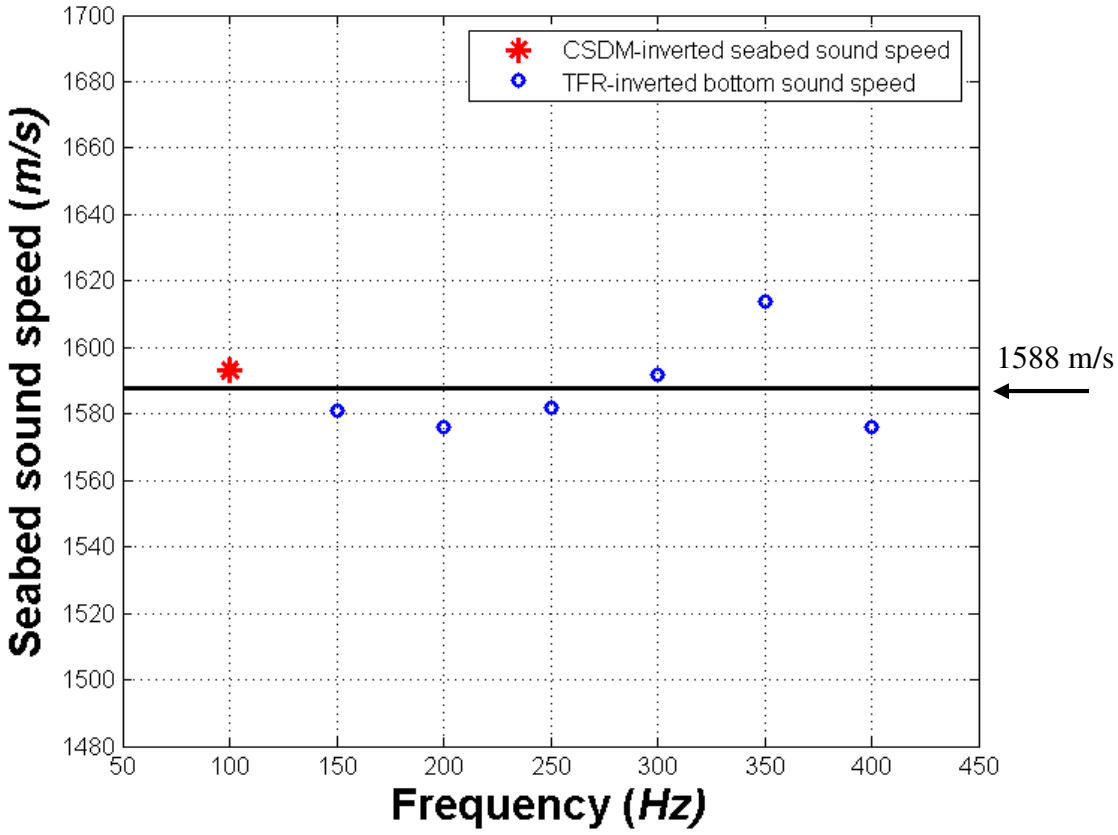

Figure 4.13 Inverted seabed sound speed as a function of frequency (YS '96)

4.4 Seabed Attenuation Inverted from Measured Modal Attenuation Coefficients

4.4.1 Method

The normal-mode attenuation coefficient for the n[th] mode can be expressed by the integrals shown in Eq. (4.23) (Koch *et al.*, 1983).

$$\beta_n = \frac{\omega}{k_n}\int_D^{\infty}\frac{\alpha_b}{c_b}\rho_b\Psi_n^2(z)dz + \frac{\omega}{k_n}\int_0^{D}\frac{\alpha}{c}\rho\Psi_n^2(z)dz \qquad (4.23)$$

where α_b is the sound attenuation in the seabottom, and α is the sound attenuation in the water column.

The normal-mode attenuation coefficients (β_n) depend on the seabed attenuation (α_b). The seabed attenuation can thus be inverted by minimizing the difference between the theoretical modal attenuation coefficients and the measured modal attenuation coefficients ($\beta_n^{'}$). The experimental modal attenuation coefficients ($\beta_n^{'}$) can be extracted from the measurements of n[th] modal amplitudes at different ranges.

For a signal mode n, Eq. (3.16) expressed in decibels becomes

$$20\log|p_n(r,z)| = 20\log\left(\frac{\frac{1}{\rho(z_s)}\sqrt{\frac{1}{8\pi}}\Psi_n(z_s)\Psi_n(z)}{\sqrt{k_{n,c}}}\right) - 20\log\left(\sqrt{r}\right) - (20\beta_n\log e)r \qquad (4.31)$$

If the source depth and receiver depth are held constant, a plot of modal amplitude (expressed in decibels and corrected for cylindrical spreading) versus ranges should be a straight line (Ingenito, 1973 and Zhou, 1985). Its slope is

$$K_a = -(20\log e)\beta_n \qquad (4.32)$$

If K_a is obtained from the experiment, then β'_n is known from Eq. (4.32). The theoretical modal attenuation coefficients are computed using KRAKEN. A half-space bottom model with three-parameters (sound speed, density and attenuation) is used. The seabed sound speed is taken to be 1588 m/s, which is the average value obtained from the CSDM-based inversion and the dispersion-based inversion. The density (1.85 g/cm^3) is taken from the core analysis. By adjusting the attenuation inputs to KRAKEN, the normal-mode attenuation coefficient (β_n) is obtained. The inverted seabottom sound attenuation is estimated by seeking a minimum of the cost function

$$Y(\alpha_b) = \sqrt{\sum_n \left(\beta_n(\alpha_b) - \beta'_n\right)^2} \tag{4.33}$$

This estimation process is shown in figure 4.14.

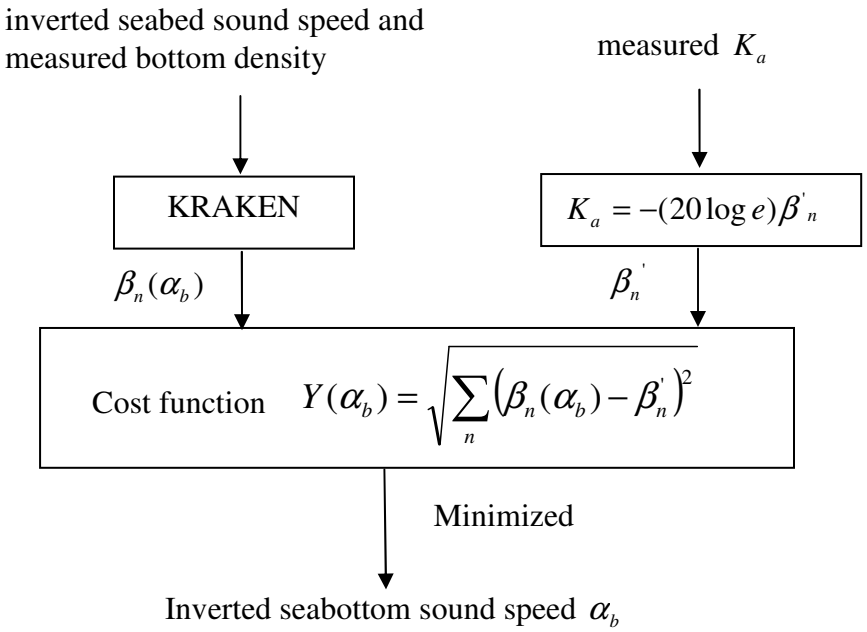

Figure 4.14 Estimation process of seabed sound attenuation using measured modal attenuation coefficients

4.4.2 Experimental Results

The amplitudes of the first three modes were measured at distances of 11 km, 19 km, 28 km, 37 km, and 55 km on the QA track over a frequency range of 100 Hz to 400 Hz. At each distance, three or four explosive signals were analyzed. For example, the modal amplitudes of the first three modes at 125Hz (expressed in decibels and corrected for cylindrical spreading) plotted versus range are shown in figure 4.15. The modal amplitude of the first mode (expressed in decibels and corrected for cylindrical spreading) plotted versus range over a frequency range of 100 Hz to 400 Hz are shown in figure 4.16. The slopes K_a of the straight lines in figures 4.15 and 4.16 are obtained by a least squares fit to the data. Then the experimental modal attenuation coefficients (β_n') are calculated using Eq. (4.32). Figure 4.17 shows the cost $Y(\alpha_b)$ as a function of seabed sound attenuation at 125 Hz. The inverted seabed sound attenuation at 125 Hz is 0.00913 dB/m at the minimum point of the cost function *Y*. The inverted seabed attenuations over a frequency range of 100Hz to 400Hz are listed in Table 4.7.

Table 4.7 Inverted seabed attenuation using measured modal attenuation coefficients (YS '96)

f (Hz)	100	125	160	200	250	315	400
α_b (dB/m)	0.00447	0.00913	0.01018	0.01448	0.02393	0.04225	0.06272

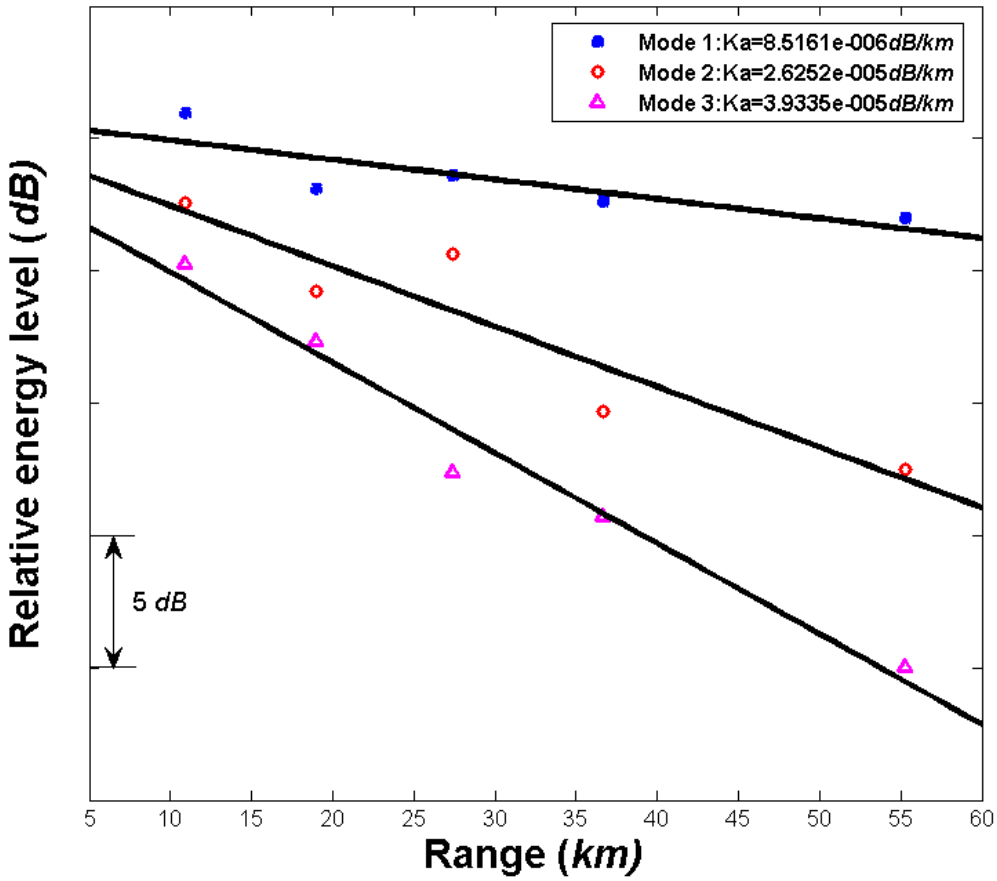

Figure 4.15 Attenuation of the first three normal modes at 125Hz corrected for cylindrical spreading. The straight lines are least-squares fits.

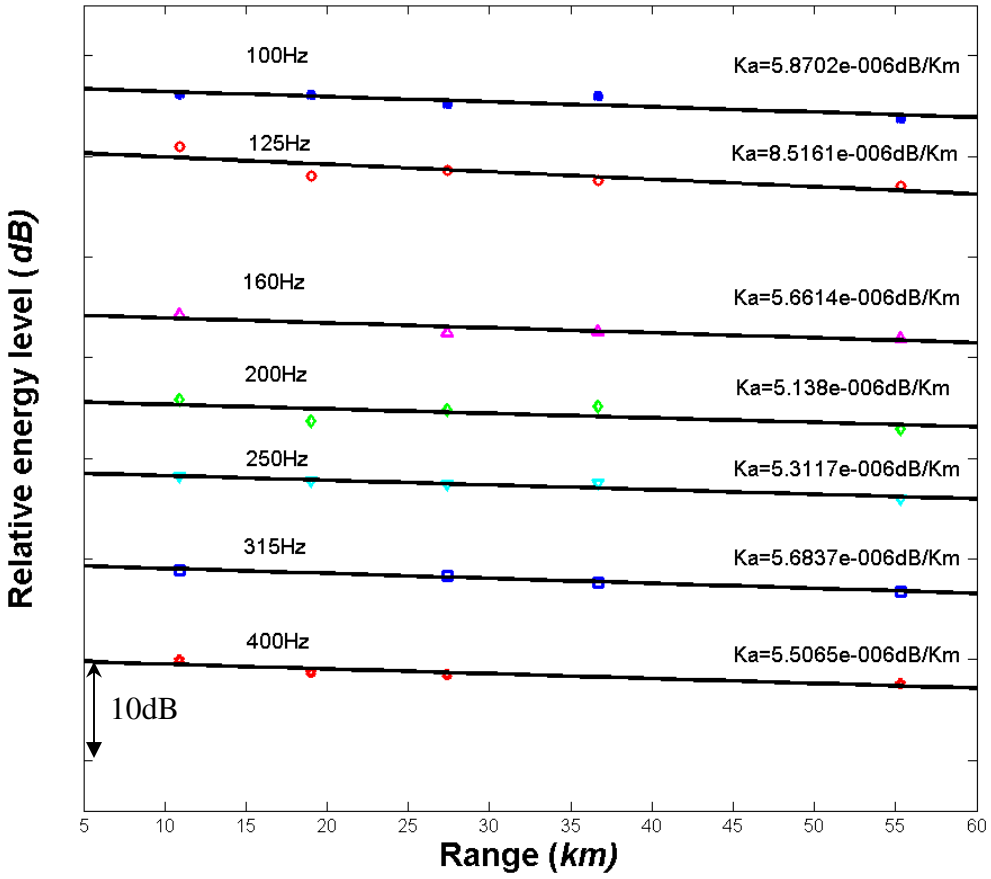

Figure 4.16 Attenuation of the first normal mode corrected for cylindrical spreading (100-400Hz). The straight lines are least-squares fits.

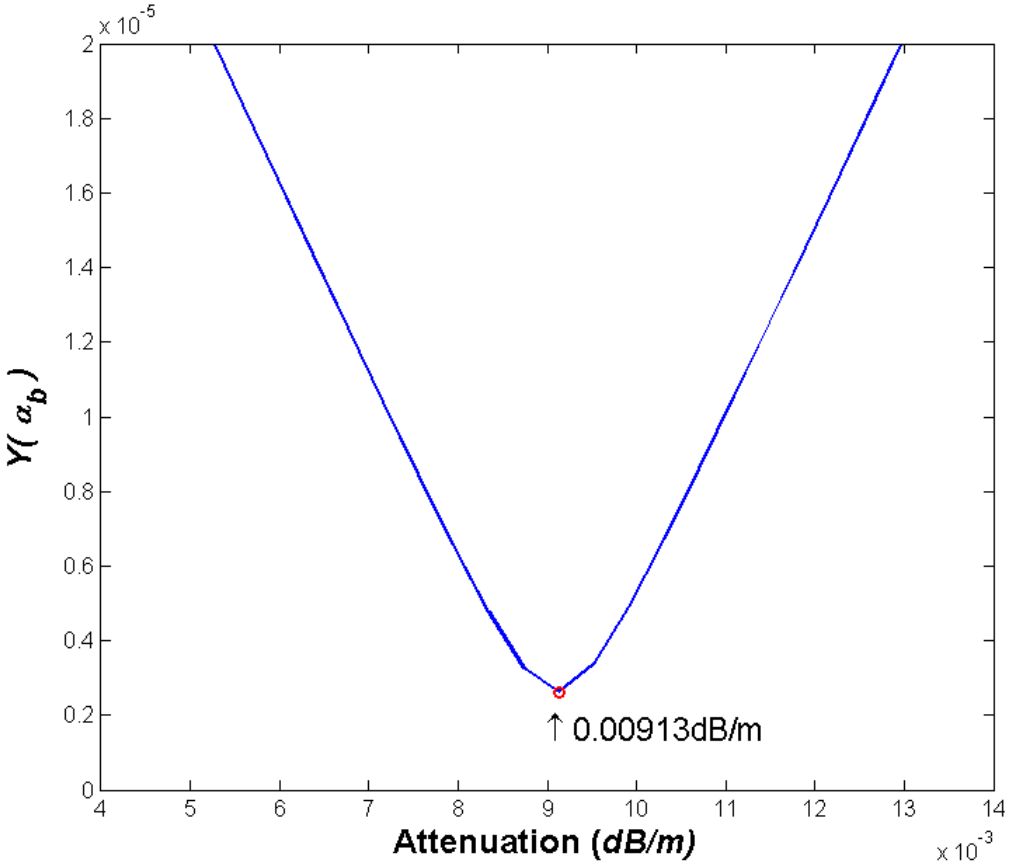

Figure 4.17 *Y* as a function of seabed sound attenuation at 125 Hz

4.5 Seabed Attenuation Inverted from Measured Modal Amplitude Ratios

4.5.1 Method

At a given distance *r* from the source, the ratio of the amplitude of the nth mode to the amplitude of the first mode can be written as

$$R_{n1}(f) = \sqrt{\frac{k_1}{k_n}} \left| \frac{\Psi_n(z_s)\Psi_n(z)}{\Psi_1(z_s)\Psi_1(z)} \right| e^{(\beta_1 - \beta_n)r} \tag{4.34}$$

The normal-mode attenuation coefficients (β_n) depend on the seabed attenuation. Thus the theoretical modal amplitude ratio [$R_{n1}(f)$] in Eq. (4.34) also depends on the seabed attenuation. The seabed attenuation can be inverted by minimizing the difference between the theoretical modal amplitude ratios and the measured modal amplitude ratios $R_{n1}^{'}$. By adjusting the attenuation inputs to KRAKEN, the modal depth functions (Ψ_n), the wave numbers (k_n), and the normal-mode attenuation coefficient (β_n) are obtained. Then the theoretical modal amplitude ratio is calculated by Eq. (4.34). The inverted seabottom sound attenuation is obtained by seeking a minimum of the cost function

$$Q(\alpha_b) = \sqrt{\sum_n \left(R_{n1}(\alpha_b) - R_{n1}^{'} \right)^2} \tag{4.35}$$

This estimation process is shown in figure 4.18.

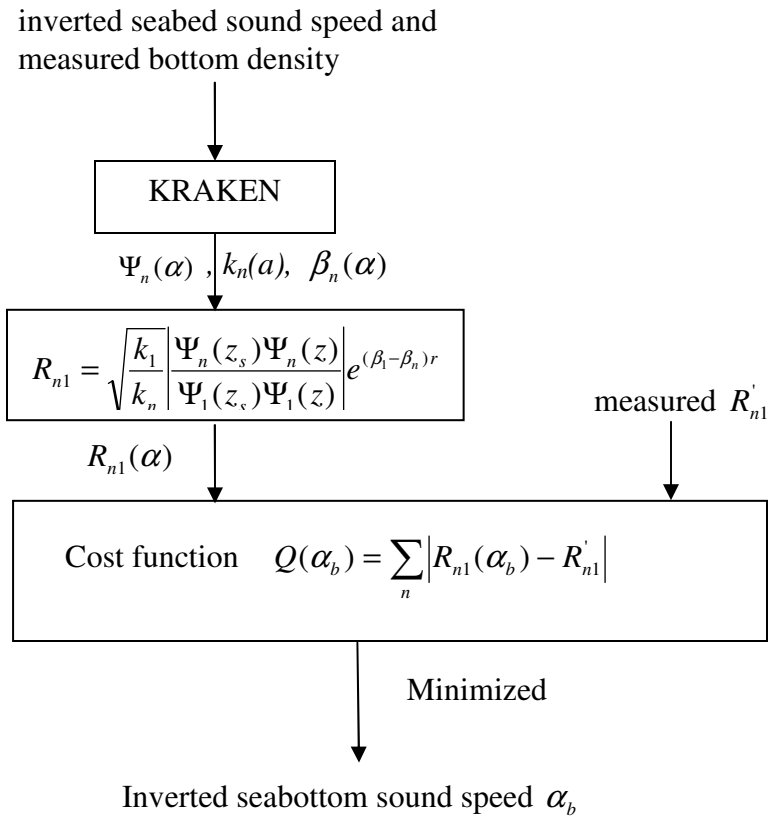

Figure 4.18 Estimation process of seabed sound attenuation using measured normal mode amplitude ratios

4.5.2 Experimental results

The ratios of the amplitude of the second mode, third mode, and fourth mode to the amplitude of the first mode (R'_{21}, R'_{31}, and R'_{41}) were extracted at distances of 13 km, 19 km, 28 km, 37 km, and 53 km on the QA track and the QG track over a frequency range of 160 Hz to 400 Hz. At each distance, around five explosive signals were analyzed. The nominal source depth was 50 m. Figures 4.19a and 4.19b show the received signals filtered by a one-third-octave filter with a center frequency of 200 Hz when the source-receiver distance is 27.48 km. The receiver depths are 40 m (Fig. 4.19a)

and 52 m (Fig. 4.19b). In Fig. 4.19a, at a receiver depth of 40 m, the shock wave and bubble pulse of the first mode, the second mode, and the fourth mode can be identified, but not the third mode. This is because the magnitude of the third mode depth function is nearly at a null at a depth of 40 m (See Fig. 3.1). At a receiver depth of 52 m, the shock wave and bubble pulse of the first four modes can be identified, but the second mode is very weak. This is because the magnitude of the second mode depth function is close to a null at a depth of 52 m (See Fig. 3.1).

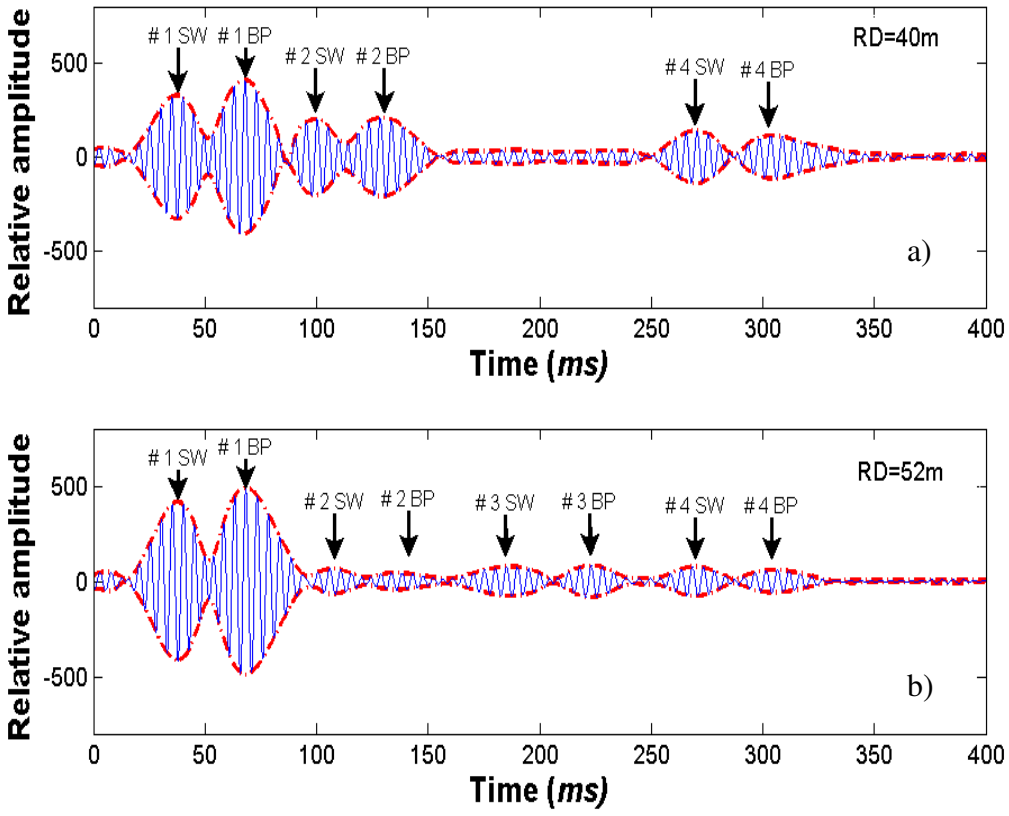

Figure 4.19 a) the signal received at the receiver depth of 40 m; b) the signal received at the receiver depth of 52 m (Range=27.48km and Frequency=200Hz).

Seabed attenuation as a function of frequency from 160 Hz to 400 Hz is determined by minimizing the difference between the theoretical modal amplitude ratios and the measured modal amplitude ratios ($R_{21}^{'}$, $R_{31}^{'}$, and $R_{41}^{'}$). The inverted seabed attenuation obtained using the amplitude ratio of the second mode to the first mode ($R_{21}^{'}$) was close to that obtained using the amplitude ratio of the third mode to the first mode ($R_{31}^{'}$) and the amplitude ratio of the fourth mode to the first mode ($R_{41}^{'}$). This implies that the bottom attenuation is not depth dependent. Different modes penetrate into different bottom depths. If there is apparent depth dependence in bottom attenuation, the seabed attenuations inverted using different modes should be different. The inverted seabed attenuations over a frequency range from 160Hz to 400 Hz are listed in Table 4.8.

Table 4.8 Inverted seabed attenuation using measured modal amplitude ratios

f (Hz)	160	200	250	315	400
α_b (dB/m)	0.00841	0.02091	0.02287	0.03516	0.05761

4.6 Seabed Attenuation Inverted from Transmission Loss data

4.6.1 Method

Seabed attenuation can also be determined by comparing Transmission Loss data with predictions along the propagation direction. This inversion method for attenuation utilizes the inverted seabottom sound speed as a constraint condition. *TL* predictions are calculated by KRAKEN. The inverted seabed attenuations are obtained by adjusting the attenuation inputs to KRAKEN such that the difference between modeled and measured *TL* is minimized. In this paper, *TL* is defined as TL_{bb} when both the source and the receiver are located below the thermocline (SD=50 m and RD=50 m); TL_{ba} is defined when the source and the receiver are separately located below and above the thermocline (SD=50 m and RD=7 m). The authors define the following cost functions:

$$E_1(\alpha_b) = \sqrt{\sum_{i=1}^{N_r}\left(\left|\hat{TL}_{ba\_QG}(i) - \hat{TL}_{bb\_QG}(i)\right| - \left|TL_{ba}(i) - TL_{bb}(i)\right|\right)^2 \Big/ (N_r - 1)} \qquad (4.36)$$

$$E_2(\alpha_b) = \sqrt{\sum_{i=1}^{N_r}\left(\left|\hat{TL}_{ba\_QA}(i) - \hat{TL}_{bb\_QA}(i)\right| - \left|TL_{ba}(i) - TL_{bb}(i)\right|\right)^2 \Big/ (N_r - 1)} \qquad (4.37)$$

$$E_3(\alpha_b) = \sqrt{\sum_{i=1}^{N_r}\left(\hat{TL}_{ba\_QG}(i) - TL_{ba}(i)\right)^2 \Big/ (N_r - 1)} \qquad (4.38)$$

$$E_4(\alpha_b) = \sqrt{\sum_{i=1}^{N_r}\left(\hat{TL}_{ba\_QA}(i) - TL_{ba}(i)\right)^2 \Big/ (N_r - 1)} \qquad (4.39)$$

where $\hat{TL}_{bb\_QG}(i)$ -- measured TL_{bb} at the i^{th} distance on the QG track,

$\hat{TL}_{ba\_QG}(i)$ -- measured TL_{ba} at the i^{th} distance on the QG track,

$\hat{TL}_{bb\_QA}(i)$ -- measured TL_{bb} at the i^{th} distance on the QA track,

$\hat{TL}_{ba\_QA}(i)$ -- measured TL_{ba} at the i^{th} distance on the QA track,

$TL_{bb}(i)$ -- calculated TL_{bb} at the i^{th} distance,

$TL_{ba}(i)$ -- calculated TL_{ba} at the i^{th} distance,

N_r -- the number of distances.

The cost function $E_1(\alpha_b)$ calculates the difference between the *TL* data and predictions on the QG track from 3 km to 20 km, when both TL_{bb} and TL_{ba} are taken into account. The cost function $E_2(\alpha_b)$ calculates the difference on the QA track from 3 km to 53.5 km, when both TL_{bb} and TL_{ba} are taken into account. The cost function $E_3(\alpha_b)$ calculates the difference on the QG track from 3 km to 20 km, when only TL_{ba} is taken into account. The cost function $E_4(\alpha_b)$ calculates the difference on the QA track from 3 km to 20 km, when only TL_{ba} is taken into account.

4.6.2 Experimental results

Seabed attenuation as a function of frequency from 80 Hz to 1000 Hz is determined by comparing Transmission Loss data with predictions along the QA and QG directions in the Yellow Sea '96 experiment. Transmission loss data as a function of range along two radial directions (QA and QG) were obtained by averaging the spectrum in 1/3-octave bands. On the QG track, five shots were detonated at 18.8 km and ten shots were detonated at each of the distances 3.9 km, 5.8 km, 9.5 km, and 12.9km. On the QA

track, ten shots were detonated at each of the distances 11.2 km and 19 km, and two shots were detonated at each of the other distances. During the experiment, the sea surface was rather smooth. In any case, sea surface effects on long-range and low-frequency sound propagation are generally negligible. The attenuation in the water column is taken into account using a simplified expression for frequency dependence of the attenuation in a water column taken from Chapter 1 of Jensen *et al.* (1994):

$$\alpha_w \cong 3.3\times10^{-3} + \frac{0.11 f^2}{1+f^2} + \frac{44 f^2}{4100+f^2} + 3.0\times10^{-4} f^2 \, [dB/km] \; (f \text{ in kHz}) \qquad (4.40)$$

Based on the range independent normal mode calculation, the theoretical incoherent *TL* is obtained using the averaged SSP measured at location Q (See Fig. 2.5). The results, obtained from 80 Hz to 1000 Hz by minimizing $E_1(\alpha_b)$, $E_2(\alpha_b)$, $E_3(\alpha_b)$ and $E_4(\alpha_b)$ respectively, are listed in Table 4.9. Tables 4.7, 4.8 and 4.9 show that the three independent approaches have resulted in consistent values for seabed attenuation.

Table 4.9 Inverted seabed attenuation using *TL* data (YS '96)

f (Hz)	80	100	125	160	200	250
α_b from $E_1(\alpha_b)$ (dB/m)	0.00207	0.00447	0.00716	0.00746	0.02330	0.01999
α_b from $E_2(\alpha_b)$ (dB/m)	0.00307	0.00636	0.00756	0.01108	0.02204	0.02157
α_b from $E_3(\alpha_b)$ (dB/m)	0.00282	0.00510	0.00834	0.00867	0.02519	0.02157
α_b from $E_4(\alpha_b)$ (dB/m)	0.00257	0.00605	0.00756	0.01149	0.02015	0.01999
Averaged α_b (dB/m)	0.00263	0.00549	0.00766	0.00967	0.02267	0.02078
f (Hz)	315	400	500	630	800	1000
α_b from $E_1(\alpha_b)$ (dB/m)	0.03630	0.06020	0.08407	0.13965	0.21663	0.36524
α_b from $E_2(\alpha_b)$ (dB/m)	0.03928	0.05516	0.08879	0.13370	0.22670	0.37783
α_b from $E_3(\alpha_b)$ (dB/m)	0.03928	0.05768	0.08722	0.12378	0.23678	0.37783
α_b from $E_4(\alpha_b)$ (dB/m)	0.04027	0.05516	0.08722	0.13766	0.21159	0.35894
Averaged α_b (dB/m)	0.03878	0.05705	0.08682	0.13370	0.22292	0.36996

When the bottom attenuation was obtained by inversion from mode attenuation coefficients, mode amplitude ratios or *TL*s, no particular form for the frequency dependence was assumed, but rather an unknown (to be determined) seabottom attenuation value (dB/m) at each frequency. For convenience, a power law form of frequency dependence for the bottom attenuation in a given frequency band is widely used in the ocean acoustics community:

$$\alpha_b = \alpha_0 f^n (dB/m \cdot kHz) \tag{1.1}$$

where α_0 and n are empirically derived constants. Using the "power law fitting" method, the constants (α_0 and n) and their uncertainties can be uniquely determined for this data. The inverted seabottom attenuation shown in figure 4.20 can approximately be expressed by:

$$\alpha_b = (0.33 \pm 0.02) f^{1.86 \pm 0.04} (dB/m \cdot kHz) \tag{4.41}$$

The standard deviations in Eq. (4.41) represent only the curve-fit uncertainties and not any of the other uncertainties in the measurements or methods.

The sound speed and attenuation in the seabottom at the YS'96 site are very close to the geoacoustic inversion results obtained in the Yellow Sea by Zhou (1985 and 1987), Li *et al.* (2000), Li *et al.* (2004), Rogers *et al.* (2000) and Dahl and Choi (2006). The resultant seabed sound attenuation in this paper exhibits nonlinear frequency dependence, which is close to the results obtained by Holmes *et al.* (2007) and Zhou *et al*. (2009).

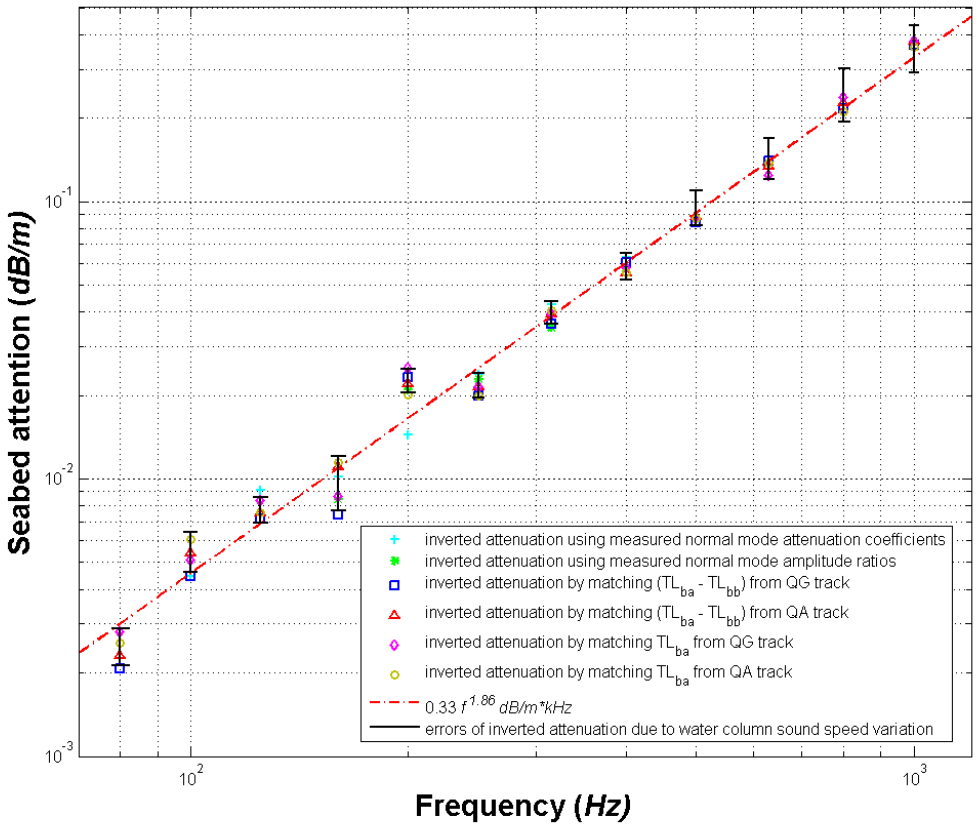

Figure 4.20 Sound attenuation in the bottom as a function of frequency (YS '96)

4.6.3 Comparison of *TL* data with predictions

TL was obtained as a function of frequency, range, and depth. Measured TL data are compared with predictions based on the inverted seabottom acoustic parameters.

4.6.3.1 *TL* as a function of range and frequency

Figure 4.21 shows that the theoretical and measured *TL*s as a function of range are in good agreement at 400Hz. The difference between TL_{bb} and TL_{ba} at 10 km shows a source-receiver depth dependence for sound propagation, which is caused by the strong thermocline. To illustrate this phenomenon, the first four theoretical normal mode shapes are shown in figure 3.1. The water column is divided into two regions by the strong thermocline. The lower region is a sound duct which includes the low sound speed portion of the water column and the thermocline itself. The other region is the isothermal region above the thermocline. Note that the magnitudes of the lower order modes in the upper region in figure 3.1 are much smaller than the corresponding magnitudes in the lower region. If both the source and the receiver are located in the lower region, the lower order modes will dominate the sound field at long range because of mode stripping. The thermocline looks like the upper boundary of the duct and TL_{bb} is similar to that in a Pekeris shallow water waveguide. If the source is in the lower region and the receiver is in the upper region, from Eq. (3.16) it is evident that only higher order modes can be transmitted. These higher order modes have higher attenuation. Therefore, TL_{ba} is much larger than TL_{bb} at a long distance. The *TL* data for sound propagation in Fig. 4.21 clearly exhibits such characteristics. The results for TL_{ba} for frequencies from 80 Hz to 630 Hz are shown in figure 4.22. The theoretical and measured TL_{ba} are in reasonable agreement.

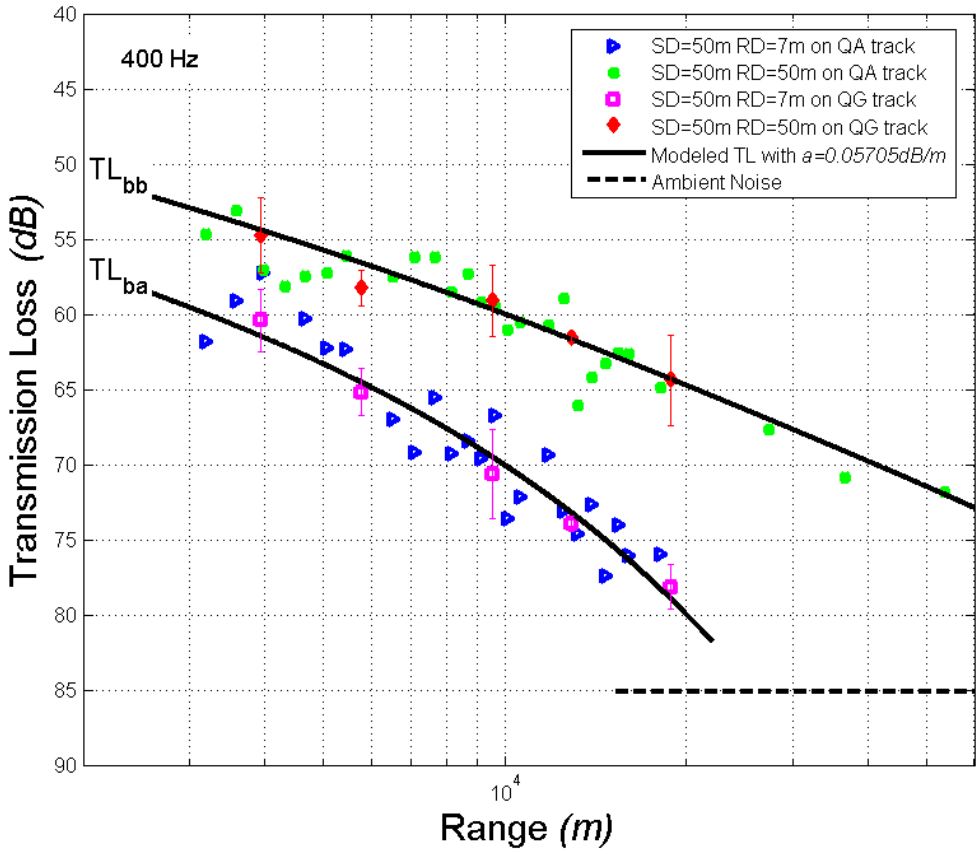

Figure 4.21 Comparison of *TL* data with predictions as a function of range along two radial directions at 400Hz

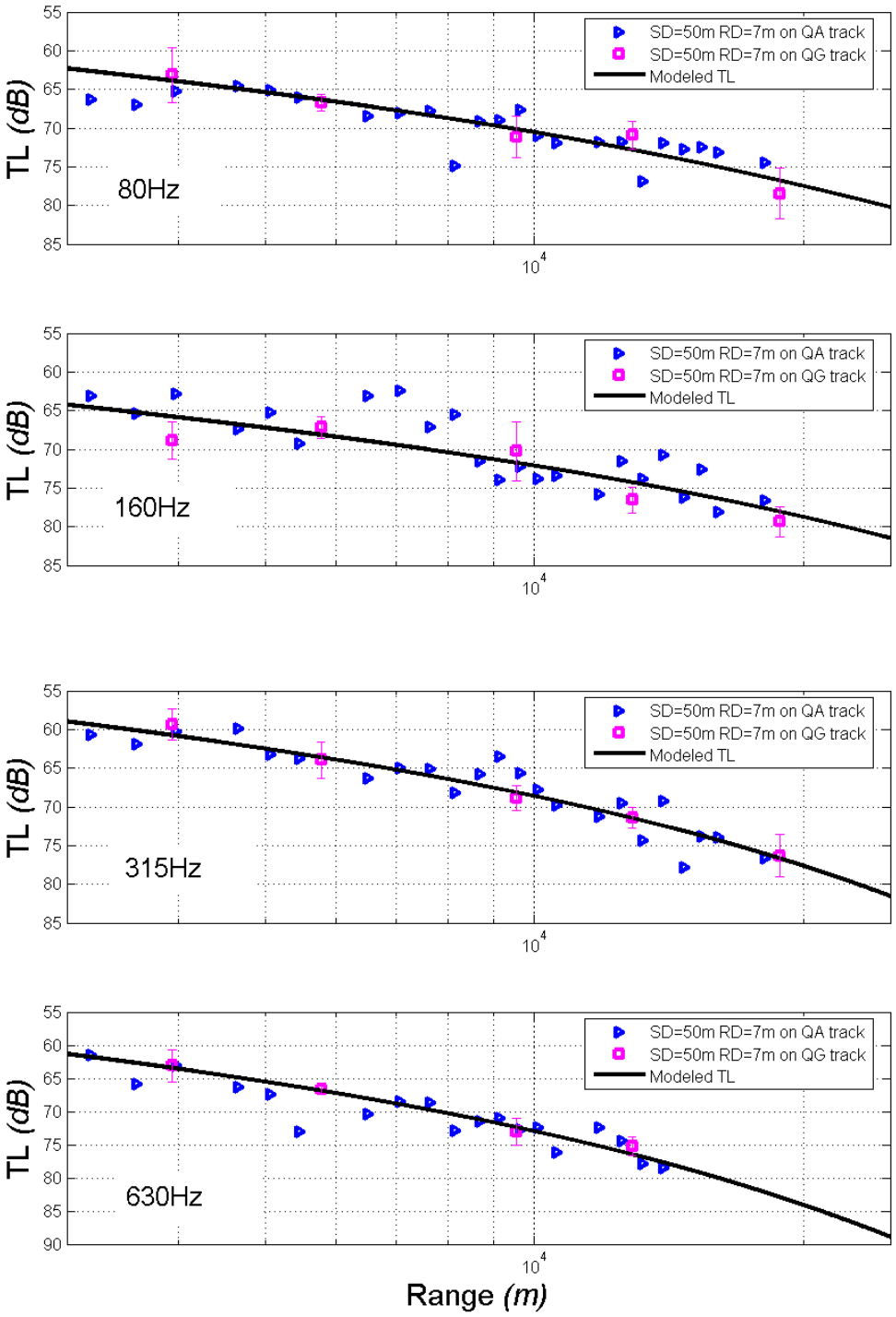

Figure 4.22 Comparison of *TL* data with predictions as a function of range when SD=50 m and RD=7 m at 80 Hz, 160 Hz, 315 Hz, and 630 Hz

4.6.3.2 *TL* as a function of depth

Both measured *TL* data and calculated *TL* as a function of depth on the QG track are obtained. Five shots were detonated at each point on the QG track. For example, figure 4.23 shows the results at 100 Hz at ranges of 5.77 km and 9.55 km. Most measured and calculated *TL* depth dependences are close to each other.

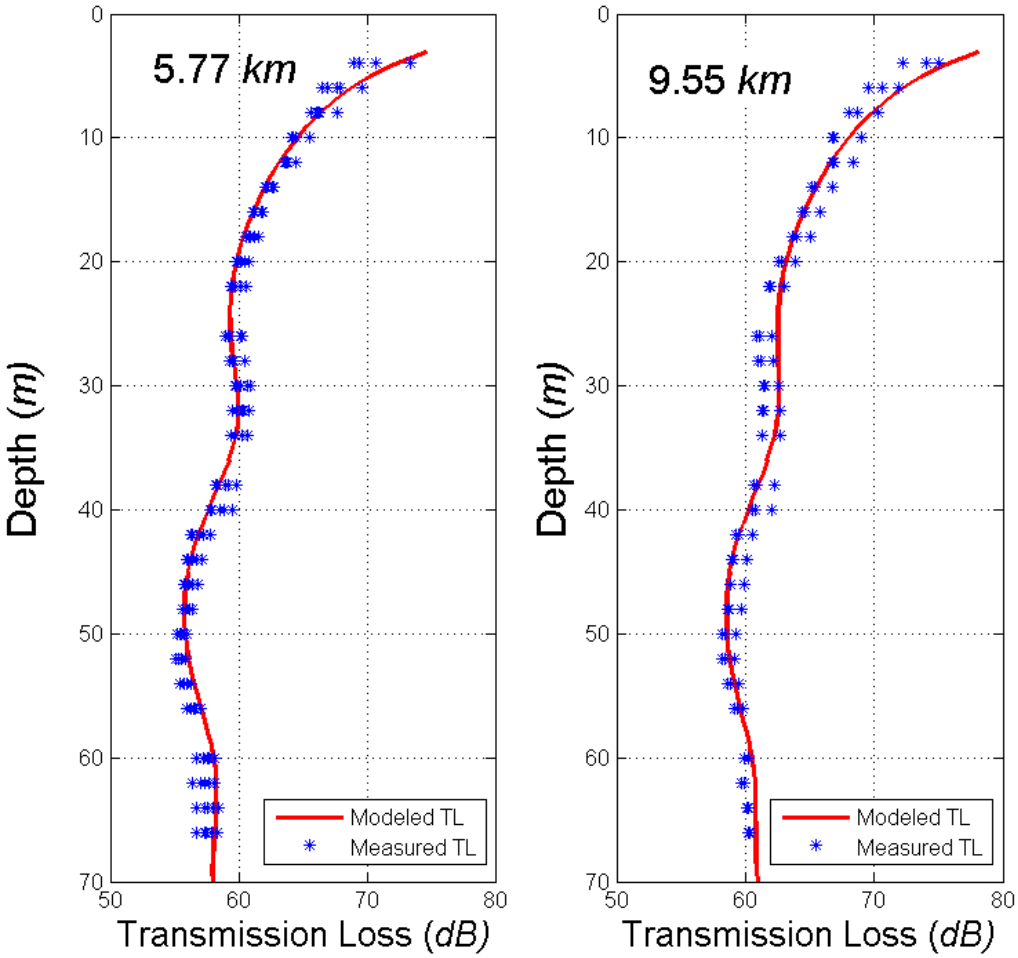

Figure 4.23 Comparison of *TL* data with predictions as a function of depth at ranges of 5.77 km and 9.55 km (SD=50 m and frequency=100 Hz)

4.6.4 Sensitivity analysis on the TL-based inversion of seabed sound attenuation

For example, figure 4.24 shows the cost E_3 as a function of the attenuation inputs at a frequency of 400Hz on the QG track. The inverted seabed sound attenuation is 0.0577dB/m at the minimum point of E_3. If the seabed attenuation increases or decreases by 0.01dB/m, the increase in the cost function (E_3) will be around 83%. Thus, the cost function is sensitive to the seabed sound attenuation. However, the sensitivity of the cost function to the seabed attenuation may not reliably indicate the sensitivity of *TL* to the seabed attenuation. Additional calculation results (shown in figure 4.25) are used to discuss the sensitivity of *TL* to the seabed attenuation. Figure 4.25 shows the effect of changes in seabed attenuations on TL_{ba} and TL_{bb}. The solid lines in Fig. 4.25 show modeled *TL* with a seabed attenuation of 0.0577dB/m, which corresponds to the best match for E_3 at 400Hz. The dashed lines and the dash-dot lines show modeled *TL* when the seabed attenuation increases and decreases by 0.01dB/m from 0.0577dB/m, respectively. The changes in TL_{bb} due to this variation of seabed attenuation are not notable from 3 km to 5 km and are less than 0.5dB from 5 km to 60 km. However, the changes in TL_{ba} are much larger than those in TL_{bb}. A variation of 0.01 dB/m in bottom attenuation will cause a variation of ±2.2 dB for TL_{ba} at 20 km. The calculations show that for the YS '96 experiment site: (1) TL_{bb} is insensitive to seabed sound attenuation from 3 km to 60 km; (2) TL_{ba} or (TL_{ba} - TL_{bb}) are sensitive to seabed sound attenuation with increasing range; (3) The four cost functions defined in Sec. 4.6.1 may appropriately be used for the geoacoustic inversion at the Yellow Sea '96 experiment.

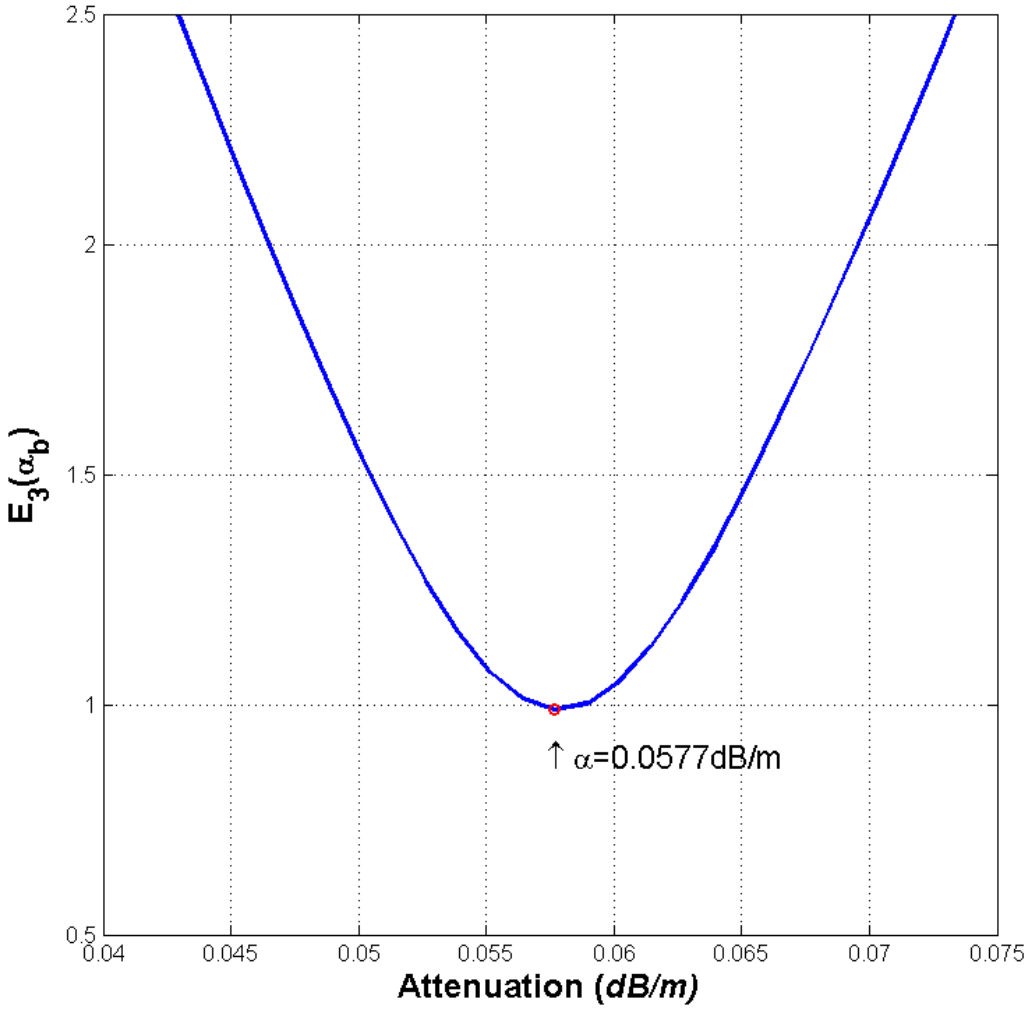

Figure 4.24 $E_3(\alpha_b)$ as a function of seabed attenuation at 400Hz

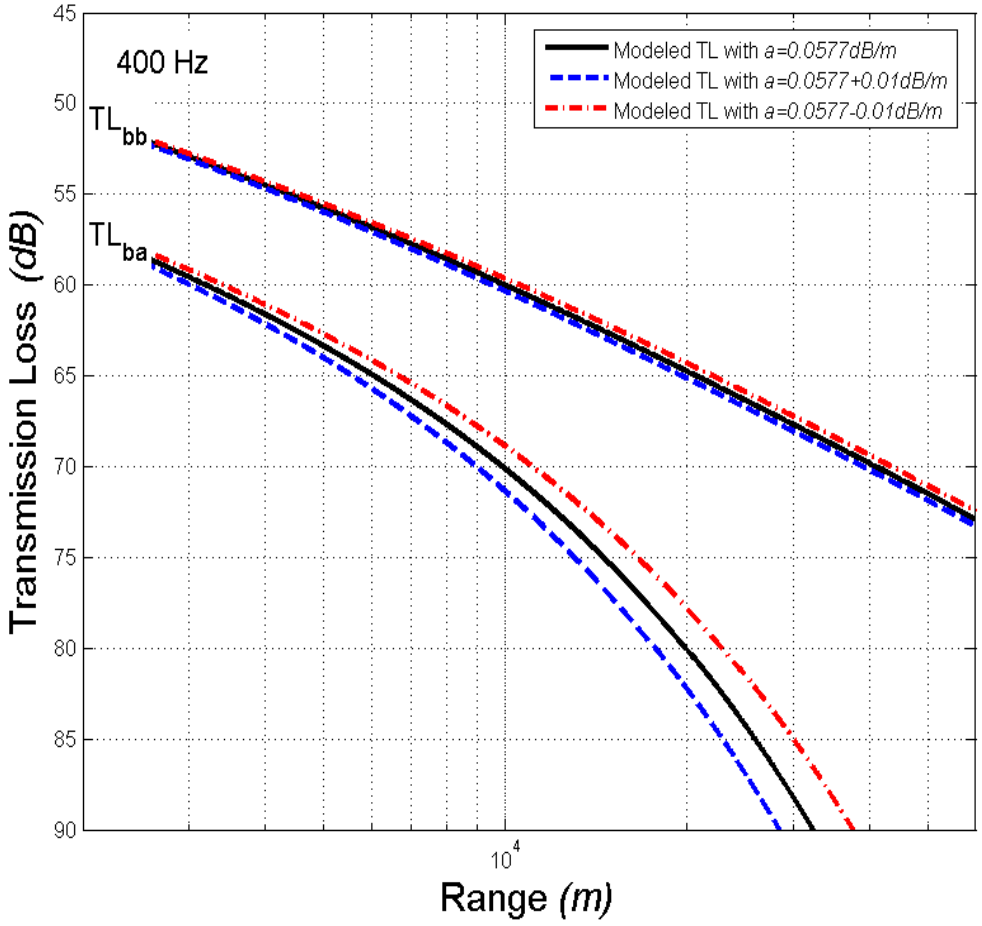

Figure 4.25 Effect of changes in seabed sound attenuation on *TL*

4.6.5 Uncertainty of inverted seabed attenuations caused by range-dependent SSPs in the water column

The variations of SSPs shown in figure 2.5 assumed to be caused by internal waves. For simplicity, it is also assumed that wideband internal waves are spatially stationary and isotropic. The SSPs measured for a long period at a given location can, in some degree, represent the SSPs measured from many locations at a given time. Then, the bootstrap method (Efron and Tibshirani, 1986) with 200 bootstrap samples is used to quantify the possible effect of the SSP spatial variation in the water column on the inverted seabed attenuation. In each bootstrap sample, sixteen water column SSPs were selected in random order from the sixteen SSPs measured over 14 hours shown in Fig. 2.5 and assigned to sixteen locations ranging from 0 km to 52.5 km with a step of 3.5 km along the sound propagation path. Sediment properties and bathymetry at the YS'96 site were well assumed to be range independent. Applying coupled mode theory to each resulting range dependent model, the seabed attenuation estimation process described in Sec. 4.6.1 is performed for every bootstrap sample. After running 200 bootstrap samples for each frequency, the averaged inverted seabed attenuations obtained by four functions (E_1, E_2, E_3, and E_4) and their standard deviations are listed in Table 4.10 and shown in Fig. 4.20. The averaged seabed attenuations inverted from 200 bootstrap samples are close to the results obtained in Sec. 4.6.2 over a frequency range of 80Hz to 1000Hz. For example, the histograms of 200 bootstrap replications of inverted seabed attenuations at 100Hz and 400Hz are shown in figures 4.26 and 4.27, respectively. In each figure, the four bootstrap histograms correspond to the inverted results obtained by four cost functions (E_1, E_2, E_3, and E_4), respectively. The height of each bar represents the

number of bootstrap samples, whose inverted seabed attenuations are within each attenuation bin. The horizontal coordinate of the vertical solid line in each histogram represents the inverted seabed attenuation obtained by range independent inversion with an averaged SSP. The horizontal coordinate of the vertical dash-dot line in each histogram represents the average inverted seabed attenuation obtained by range dependent inversions with 200 bootstrap samples. In figures 4.26 and 4.27, the center of each histogram (the vertical dash-dot line) is close to the vertical solid line. The comparison of inverted seabed attenuations obtained using a range independent model with those obtained using a range dependent model indicates that the effect of the SSP variation in the water column on the inverted seabed attenuation is weak. Range-independent inversion with an averaged SSP is acceptable for the Yellow Sea '96 experiment.

Table 4.10 Inverted seabed attenuation and standard deviation

f (Hz)	80	100	125	160	200	250
Averaged α_b (dB/m)	0.00250	0.00551	0.00778	0.00987	0.02267	0.02183
Standard deviation (dB/m)	0.00038	0.00091	0.00082	0.00216	0.00224	0.00225
f (Hz)	315	400	500	630	800	1000
Averaged α_b (dB/m)	0.03996	0.05869	0.09543	0.14444	0.24752	0.36126
Standard deviation (dB/m)	0.00373	0.00637	0.01374	0.02448	0.05403	0.06919

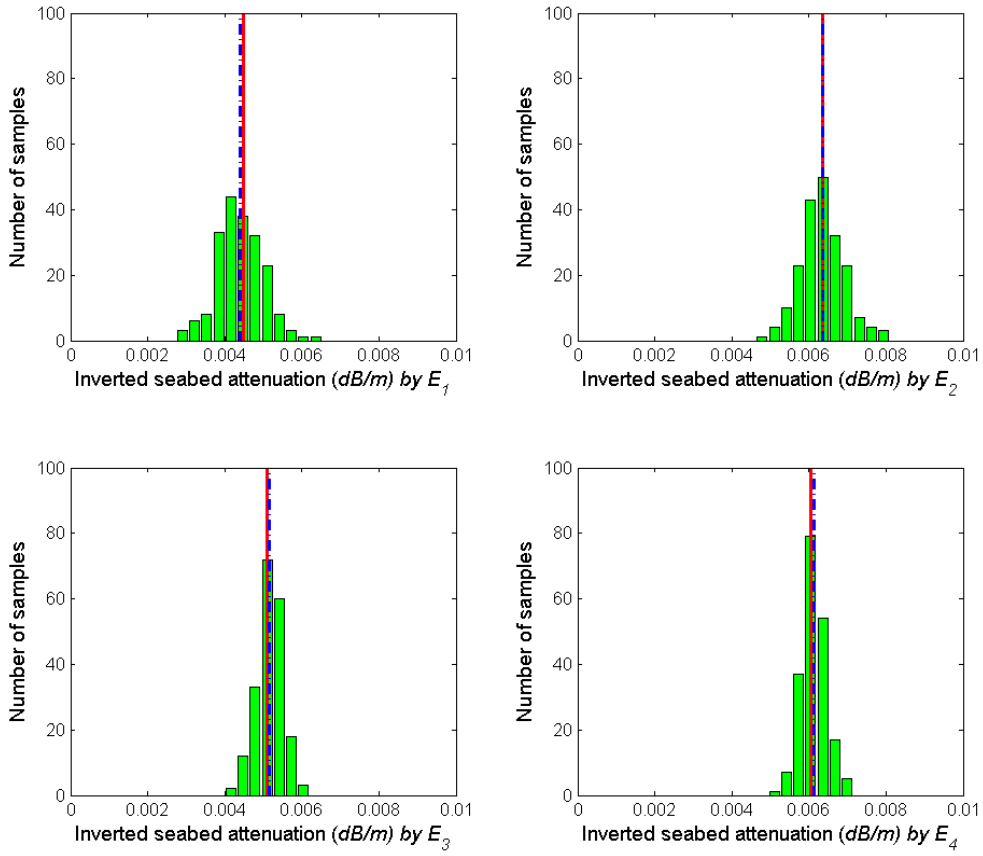

Figure 4.26 Histograms of 200 bootstrap replications of inverted seabed attenuations by four cost functions (E_1, E_2, E_3, and E_4) at 100Hz

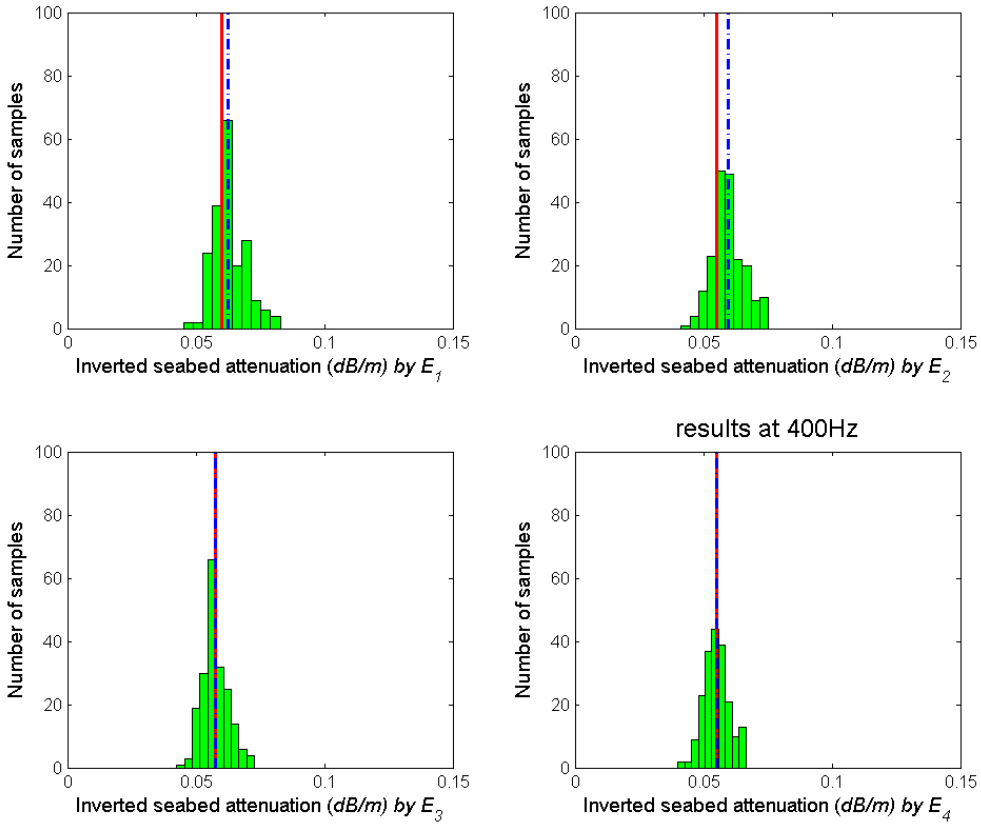

Figure 4.27 Histograms of 200 bootstrap replications of inverted seabed attenuations by four cost functions (E_1, E_2, E_3, and E_4) at 400Hz

CHAPTER 5

SEABED SOUND SPEED AND ATTENUATION INVERSION FOR THE SHALLOW WATER '06 EXPERIMENT

5.1 Introduction

In the summer of 2006, a large multidisciplinary experiment (SW '06) was conducted off the coast of New Jersey. Over its two month duration, a number of sub-experiments were carried out which deal with geo-acoustic inversion. This chapter contains analysis of combustive sound source signals, light bulb implosion signals and chirp signals, which were transmitted from the two research vessels (Knorr and Sharp) and measured by three L-shaped arrays (SWAMI32, SWAMI52, and Shark). The goals of this chapter are: (1) to analyze modal characteristics of broadband explosive sound signals; (2) to study the characteristics of three dimensional (3D) spatial coherence; (3) to obtain *TL*s as a function of range, frequency, and depth; (4) to invert sound speed and attenuation in the seabottom using the data from (1); (5) to validate the resultant geo-acoustic parameters using spatial coherence data and *TL* data obtained from (2) and (3).

In Chapter 4, no apparent bottom layer structure was found by a site survey at the YS '96 site (Li *et al.*, 1991), a half-space bottom model (with an effective sound speed, attenuation and density) was hence used for the YS '96 experimental data. The cost function with one unknown geo-acoustic parameter (such as seabed sound speed and seabed attenuation) was minimized by local optimization methods, which are deterministic algorithms. In this chapter, site surveys by chirp sonar mapped an interface known as the "R"-reflector over the SW'06 experimental area. The "R"-reflector is around 20 m under the seabed and is indicated by a green line in Fig. 5.1 (Goff *et al.*,

2007). A bottom model with two layers in the seabed is used in the SW '06 experiment (see figure 5.2). In figure 5.2, H0 is the water depth (~70 m); H1 is the depth of the first bottom layer (~20 m); C1U is the sound speed right below the interface of water and the first bottom layer; C1D is the sound speed right above the interface of the first and second bottom layer (a linear gradient of sound speed is assumed in the first bottom layer); C2 is the sound speed in the second bottom layer; ρ_1 and ρ_2 are the densities of the first and second bottom layers, respectively. Core analysis shows that ρ_1 is $1.85 g/cm^3$ and ρ_2 is $2.1 g/cm^3$. The sound effective attenuation in the seabed (α_b) is assumed to be same in those two bottom layers.

Since the densities of the first and second bottom layers are not sensitive to the cost functions used in this chapter, ρ_1 and ρ_2 will not be determined by inversion. Besides the seabed sound speed and attenuation, H0 and H1 are sensitive to the cost function defined by modal arrival time differences. H0 and H1 can be estimated by inversion. The inverted H0 and H1 are compared with their measured values from the site survey, which is a sanity check.

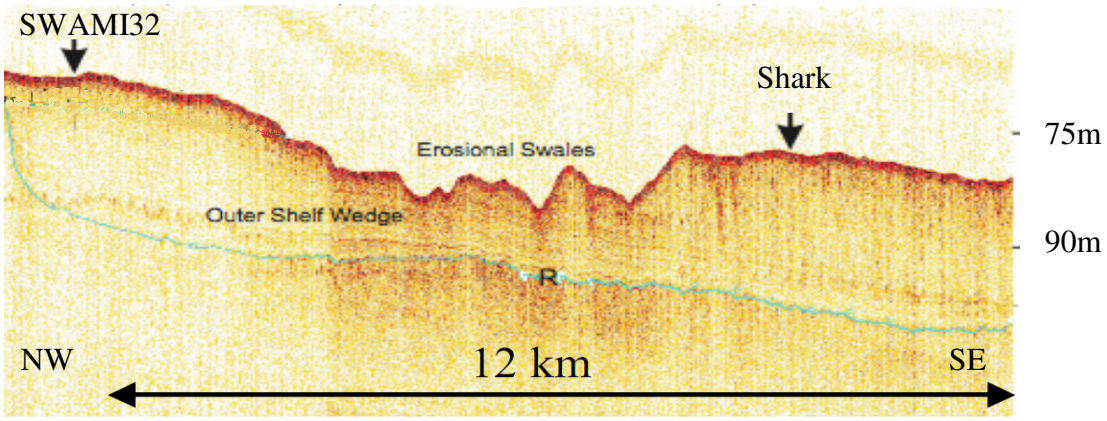

Figure 5.1 Chirp seismic section measured during SW'06

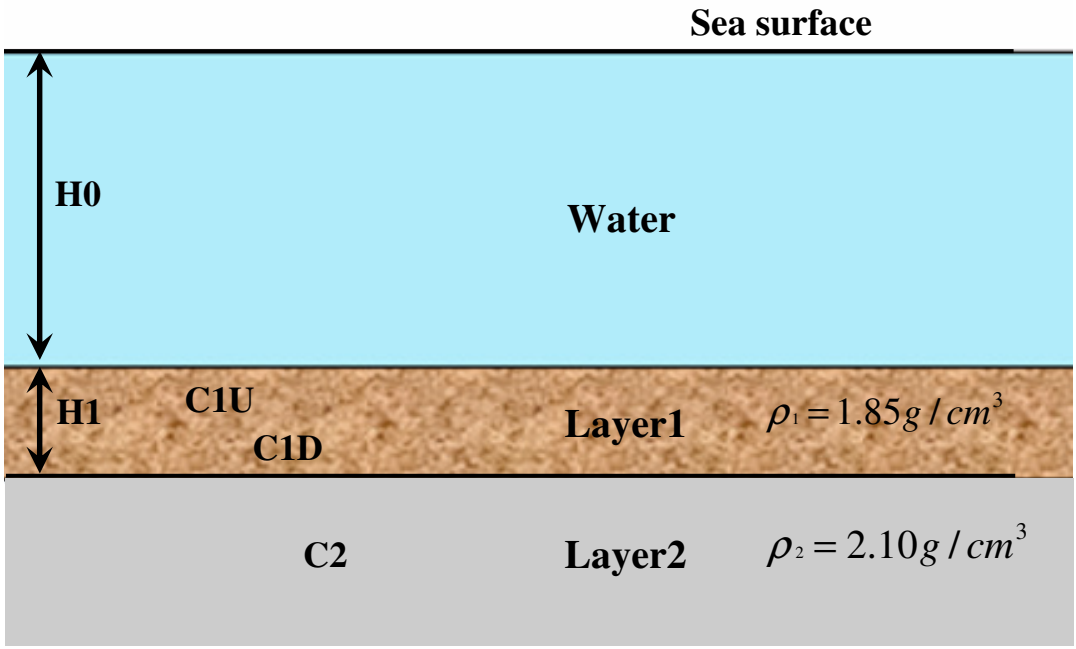

Figure 5.2 A bottom model with two layers in the seabed

Both local and global optimization methods have been successfully used in the geo-acoustic inversions. Gerstoft (1995) applied a combination of genetic algorithms and the Gauss-Newton approach to geo-acoustic inversion. The Levenberg-Marquardt algorithm, which is a local search approach, has been used in the estimation of seabottom properties by Neilsen (2000). Potty *et al.* (2003) used a hybrid scheme in the inversion for sediment compressional wave velocity, where the best parameter vector obtained by a GA search is further optimized using the Levenberg-Marquardt algorithm.

Both local and global optimization methods are used to find the minimum of the cost function in the geo-acoustic inversions of the SW'06 experiment. In section 5.2, the cost function is defined by multiple unknown parameters (sediment layer depth, seabed sound speed in each sediment layer, and water depth). A hybrid optimization method, including a genetic algorithm (GA) and a pattern search algorithm, is used to find the global minimum of the cost function and to estimate those unknown parameters at the SW '06 site. In section 5.3, the sound speed right below the interface of water and the first bottom layer is inverted using the data derived mode depth function by an exhaustive local search. The inverted results obtained in sections 5.2 and 5.3 are used as a constraint condition to estimate the sound attenuation in the seabed by matching the theoretical modal amplitude ratios with experimental data in section 5.4.

Spatial coherence of the sound field in shallow water is sensitive to the seabed parameters. Zhou *et al.* (2004) used reverberation vertical coherence data to invert the seabed sound speed and attenuation. The experimental configuration of sub-experiment one in SW '06, shown in figure 2.12, offers an opportunity to simultaneously analyze the three dimensional (3D) spatial coherence: vertical, transverse horizontal and longitudinal

horizontal. In section 5.5, the spatial coherence data as a function of frequency and range are analyzed and used to validate the inverted results obtained in sections 5.2, 5.3 and 5.4.

A sensitivity analysis for the *TL*-based inversion of seabed sound attenuation is given in section 4.6.4. The calculation shows that *TL* is sensitive to the seabed geo-acoustic parameters when the source is located below the thermocline and the receiver is located above the thermocline. In sub-experiment two of SW '06, several geo-acoustic tracks (shown in figure 2.16) were designed to obtain *TL* as a function of range. In section 5.6, the inverted results obtained in sections 5.2, 5.3 and 5.4 are validated by comparing the theoretical *TL* with measured data.

5.2 Seabed Sound Speed Inverted from Measured Modal Arrival Times

5.2.1 Multiple parameter inversion by a hybrid optimization approach

Measured modal arrival times were successfully used to invert the seabed sound speed in the YS '96 experiment. The details of this method can be found in section 4.3.1. Five parameters (H0, H1, C1U, C1D and C2) are sensitive to modal arrival time difference. Based on this dispersion characteristic of broadband signals, those five parameters are used to parameterize the cost functions and are estimated by seeking a minimum of the cost function.

$$L(H0, H1, C1U, C1D, C2) = \sqrt{\sum_{m,n(m\neq n)} (K'_{tmn} - K_{tmn}(H0, H1, C1U, C1D, C2))^2} \qquad (5.1)$$

A standard hybrid optimization algorithm, which includes a genetic algorithm (GA) and a pattern search algorithm from the MATLAB toolbox, is used to find the minimum of the cost function. The optimum parameters obtained from the GA inversion are used as a starting point for a local search using a pattern search algorithm, which

searches a set of points, called a mesh, around the current point. The mesh is formed by adding the current point to a scalar multiple of a fixed set of vectors called a pattern.

If the pattern search algorithm finds a point in the mesh where the value of the cost function is lower than the value at the current point, the new point becomes the current point at the next step of the algorithm. The multiplier at the next step is called the expansion factor and normally has a default value of 2. Thus, the mesh size at the next step is doubled.

If none of the mesh points at the current step have a smaller cost function value than the value at the current point, the algorithm does not change the current point at the next step. The multiplier at the next step is called the contraction factor and normally has a value of 0.5. Thus, the mesh size at the next step gets smaller.

Through a set of steps, the pattern search algorithm computes a sequence of points that get closer and closer to the optimal point, which corresponds to the minimum of the cost function.

The estimation process using hybrid optimization is shown in figure 5.3.

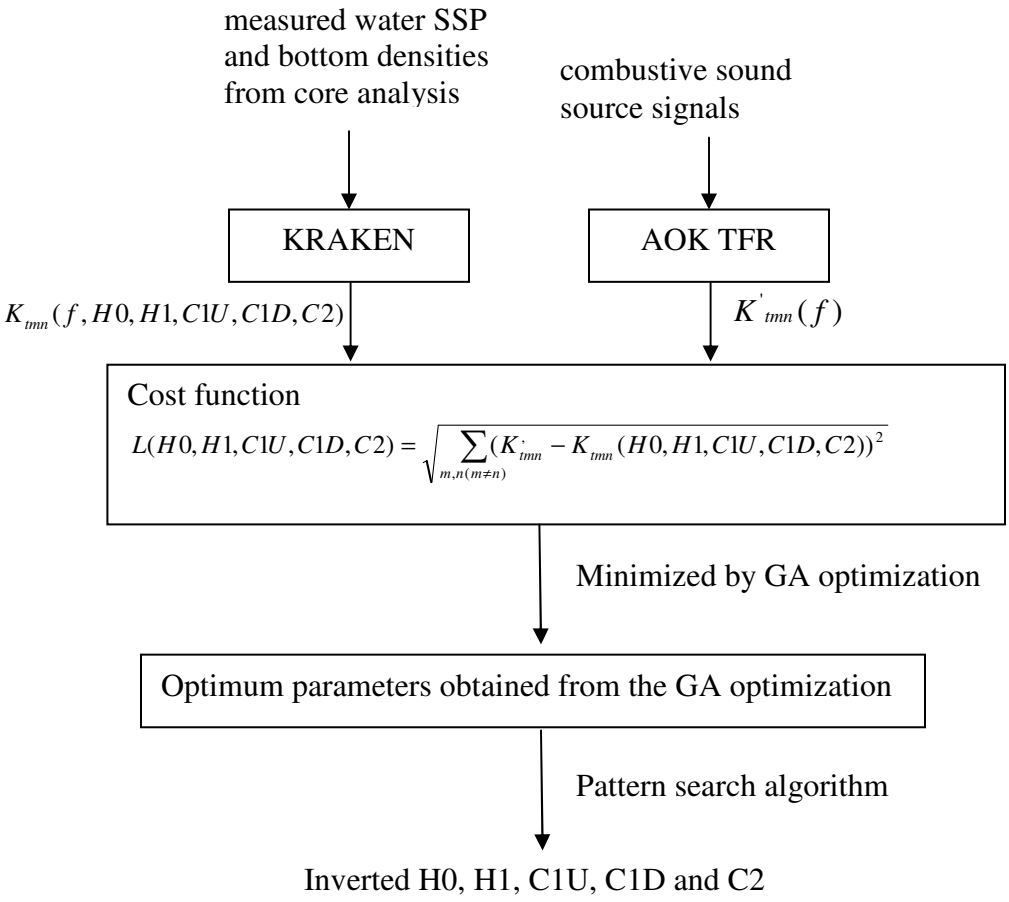

Figure 5.3 Estimation process of multiple parameters using measured modal arrival times

5.2.2 Estimation of multiple parameters using simulated data

In order to predict how this estimation process would work with experimental data, simulated sound fields are generated by KRAKEN. The input parameters of KRAKEN are listed in Table 5.1 and the input SSP is shown in figure 2.13. Theoretical group slowness differences are calculated and listed in Table 5.2

Table 5.1 Input parameters for KRAKEN

H_0 (m)	H_1 (m)	$C1U$ (m/s)	$C1D$ (m/s)	$C2$ (m/s)	ρ_1 (g/cm^3)	ρ_2 (g/cm^3)	α_b (dB/λ)
70	20	1600	1800	1865	1.85	2.10	0.000373

Table 5.2 Theoretical group slowness differences

f (Hz)	30	50	70		
K'_{t12} (s/m)	5.3237×10^{5}	2.3915×10^{-5}	1.1339×10^{-5}		
K'_{t13} (s/m)		6.4893×10^{-5}	3.8495×10^{-5}		
K'_{t14} (s/m)			6.4825×10^{-5}		
	90	110	130	150	200
K'_{t12} (s/m)	6.3153×10^{-6}	4.2026×10^{-6}	3.2856×10^{-6}	2.8342×10^{-6}	2.1584×10^{-6}
K'_{t13} (s/m)	2.1113×10^{-5}	1.2161×10^{-5}	7.3637×10^{-6}	5.1032×10^{-6}	4.2802×10^{-6}
K'_{t14} (s/m)	4.8844×10^{-5}	3.1279×10^{-5}	1.9937×10^{-5}	1.2351×10^{-5}	2.8193×10^{-6}
K'_{t15} (s/m)	5.5401×10^{-5}	5.4801×10^{-5}	3.9472×10^{-5}	2.8401×10^{-5}	1.2118×10^{-5}
K'_{t16} (s/m)	1.2894×10^{-6}	4.0047×10^{-5}	5.7149×10^{-5}	4.4811×10^{-5}	2.3034×10^{-5}
K'_{t17} (s/m)			2.2331×10^{-5}	5.6887×10^{-5}	3.4448×10^{-5}

It is assumed that five parameters (H0, H1, C1U, C1D and C2) need to be estimated from the simulated group slowness differences shown in Table 5.2. Inputting K'_{tmn} into Eq. (5.1), the cost L is minimized by a hybrid optimization approach, including a genetic algorithm (GA) and a pattern search algorithm. In the GA optimization, the search bounds for five parameters (H0, H1, C1U, C1D and C2) are listed in Table 5.3. The search bounds are determined by *a priori* knowledge of those parameters. An initial population of 40 samples is randomly generated within the search bounds for the unknown parameters. These 40 samples are the first generation of the GA. The value of the cost function for each sample is calculated. The smallness of the cost function value measures the fitness of the sample. The GA creates three types of children for the next generation. 1) Elite children: the samples in the current generation with the best fitness values. These samples automatically survive to the next generation. 2) Crossover children: the samples in the next generation are created by combining the vectors of a pair of parents, which are the samples in the current generation. 3) Mutation children: the samples in the next generation are created by introducing random changes, or mutations, to a single parent. Here, the numbers of elite children, crossover children, and mutation children for each generation are set at 2, 24, and 14, respectively. The best fitness function value at each generation is the minimum of the cost function values for 40 samples at that generation. Figure 5.4 shows the minimum and average of the cost function values for 40 samples at each generation. Through a set of generations, the initial population evolves in order to become more fit. If there is no improvement in the minimum of the cost function values for 10 consecutive generations, the genetic algorithm will stop. In figure 5.4, the genetic algorithm stops at the 40th generation. The

cost function values for 40 samples at the 40th generation are close to the best fitness function value. The optimum point in the parameter space corresponds to the optimum parameters with the best fitness function value. The optimum point at the 40th generation is used as a starting point for a local search using the pattern search algorithm. The inverted results of multiple parameters (H0, H1, C1U, C1D and C2) are listed in Table 5.3. The results in Table 5.3 indicate that the estimation process shown in Figure 5.3 is reliable.

Table 5.3 Search bounds and inverted results from simulated data

	H0 (m)	H1 (m)	C1U (m/s)	C1D (m/s)	C2 (m/s)
Search Bounds	[68,72]	[5,30]	[1580,1650]	[1700,1900]	[1800,1900]
Inversion Results	69.94	20.02	1608.00	1803.90	1865.01
Input Value	70	20	1600	1800	1865
Difference	-0.06	0.02	8.00	3.90	0.01

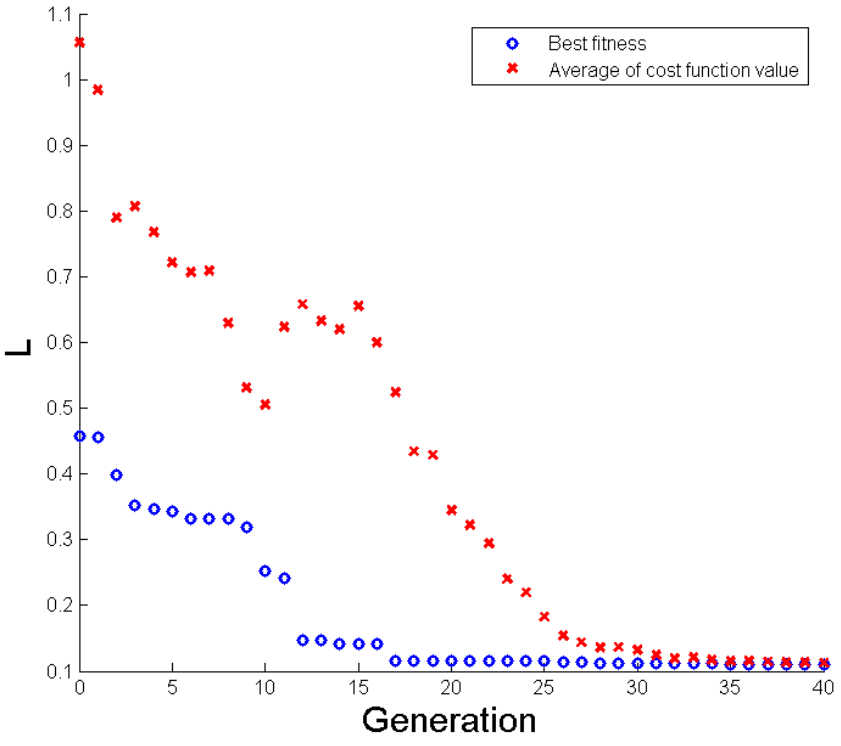

Figure 5.4 Minimum and average of cost function values vs. generation

5.2.3 Estimation of multiple parameters using experimental data

5.2.3.1 Time-frequency representation of the broadband signals in sub-experiment one of SW '06

Figure 5.5a shows the measured time series at a distance of 16.33 km when the combustive sound source (SD=50 m) was detonated on the BA track (shown in figure 2.9) and the receiver was the 17^{th} hydrophone of SWAMI52. Figure 5.5b shows the measured time series at a distance of 16.33 km when the combustive sound source depth (SD) was 50 m and the receiver was the 20^{th} hydrophone of SWAMI52, which was laid on the seabed. The time series in Fig. 5.5a and Fig. 5.5b were processed using AOK TFR and the results are shown in Fig. 5.6a and Fig. 5.6b, respectively. It is seen from figures 5.6a and Fig. 5.6b that the dispersion curves can not be easily identified because of the low signal to noise ratio.

The HLA portion of SWAMI52 (hydrophone number: 17-52) was laid on the seabed and exactly perpendicular to the direction of sound propagation. The time series received by the hydrophones of the HLA portion of SWAMI52 are combined so that the signal to noise ratio is enhanced and the dispersion curves can be easily identified. Figure 5.7 shows the combined time series of 36 channels on the HLA portion of SWAMI52. The time series in Fig. 5.7 were processed using AOK TFR and the results are shown in Fig. 5.8.

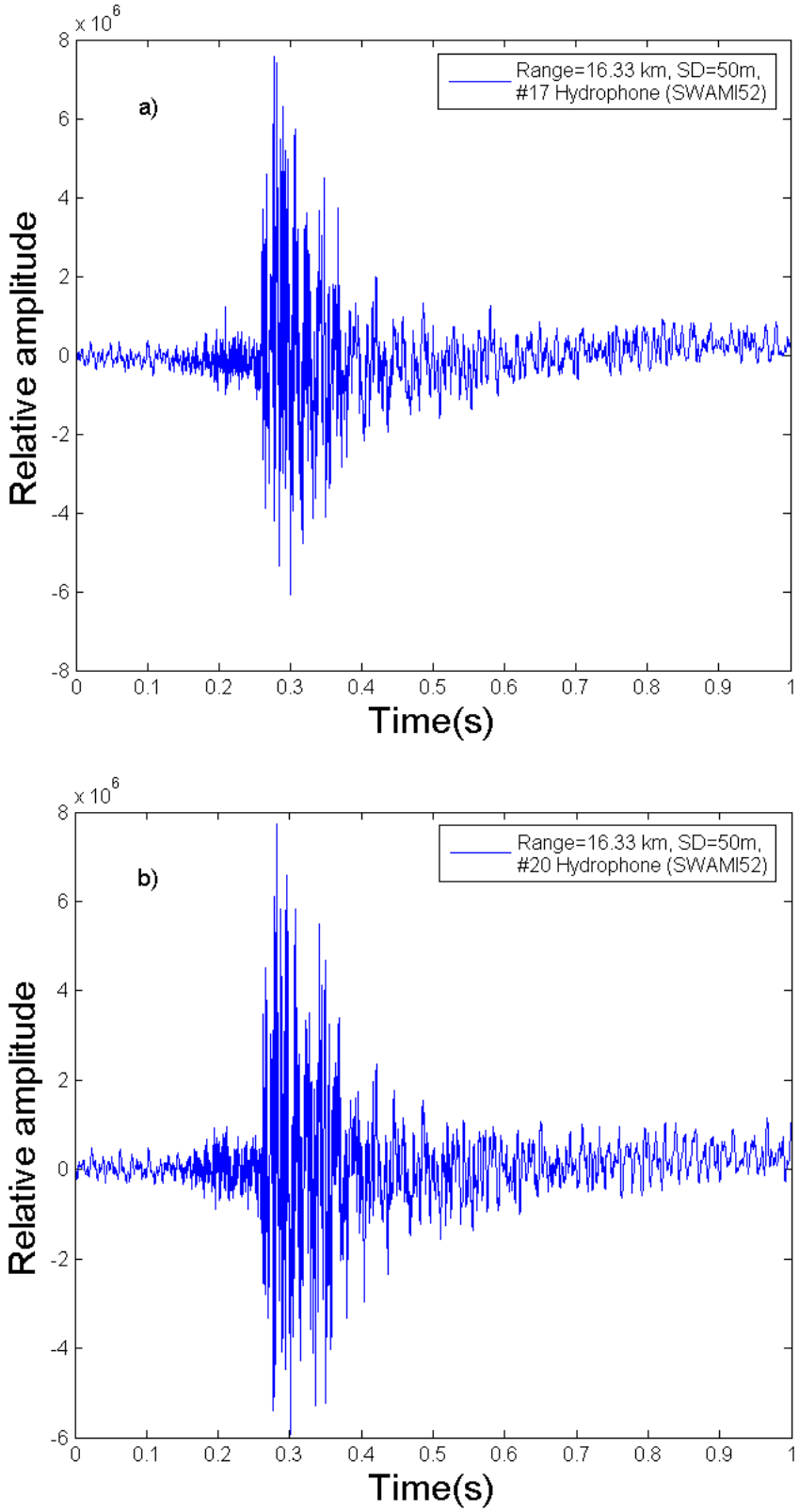

Figure 5.5 Measured time series of combustive sound source signals: a) the receiver is #17 hydrophone of SWAMI52. b) the receiver is #20 hydrophone of SWAMI52.

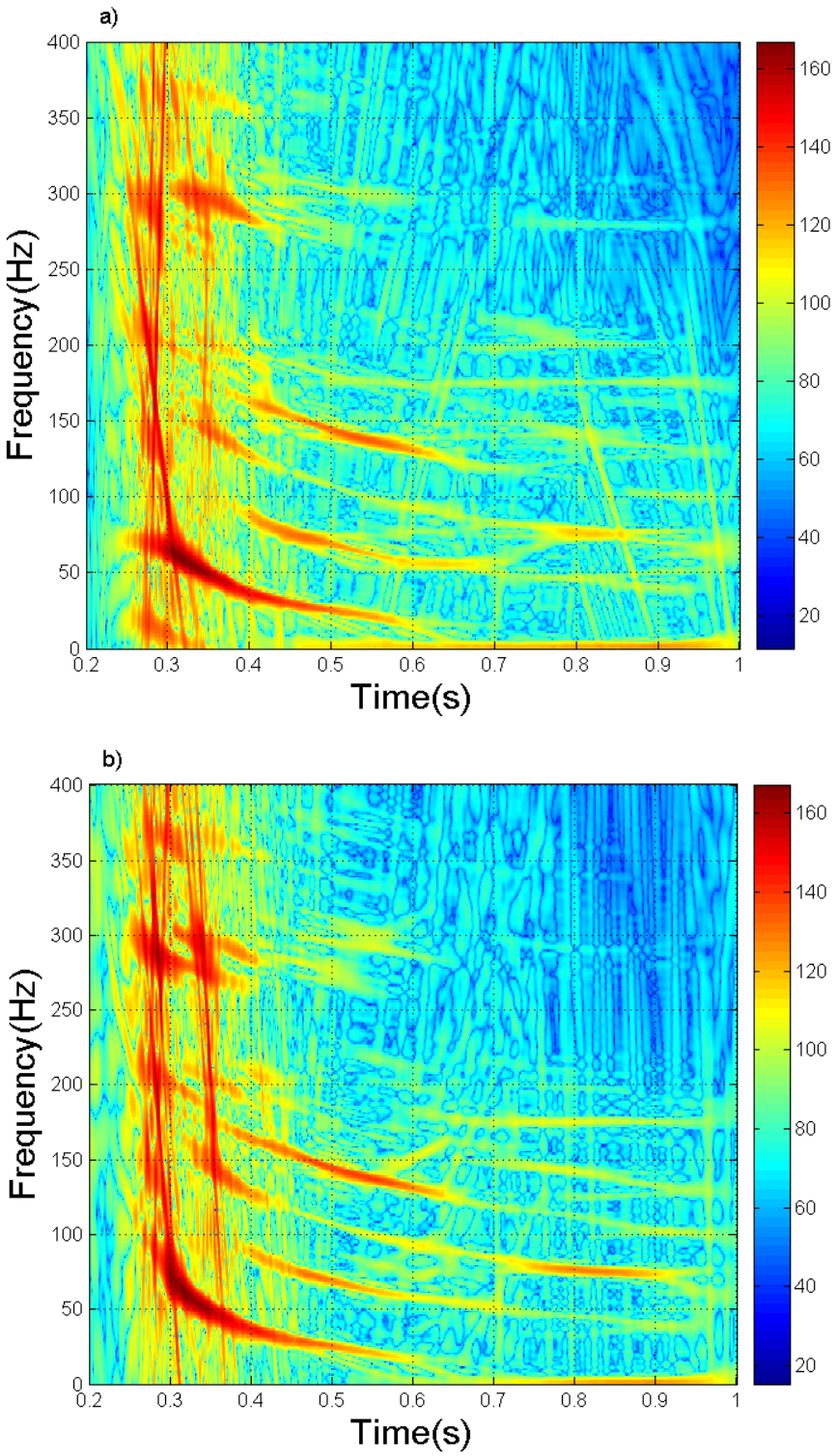

Figure 5.6 TFR of measured time series of combustive sound source signals: a) the receiver is #17 hydrophone of SWAMI52. b) the receiver is #20 hydrophone of SWAMI52.

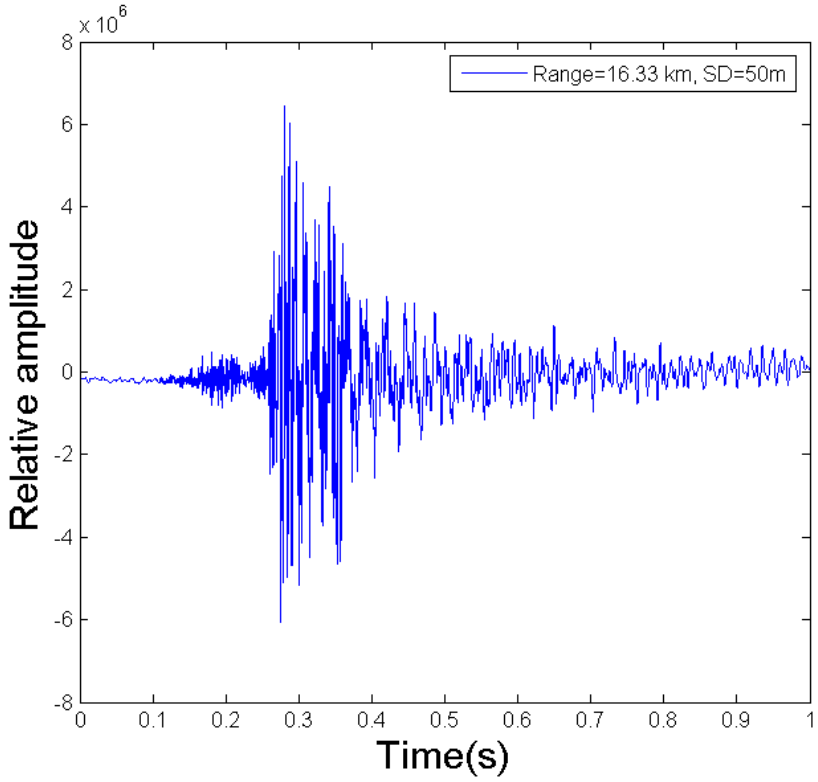

Figure 5.7 Combined time series of 36 channels on the HLA portion of SWAMI52

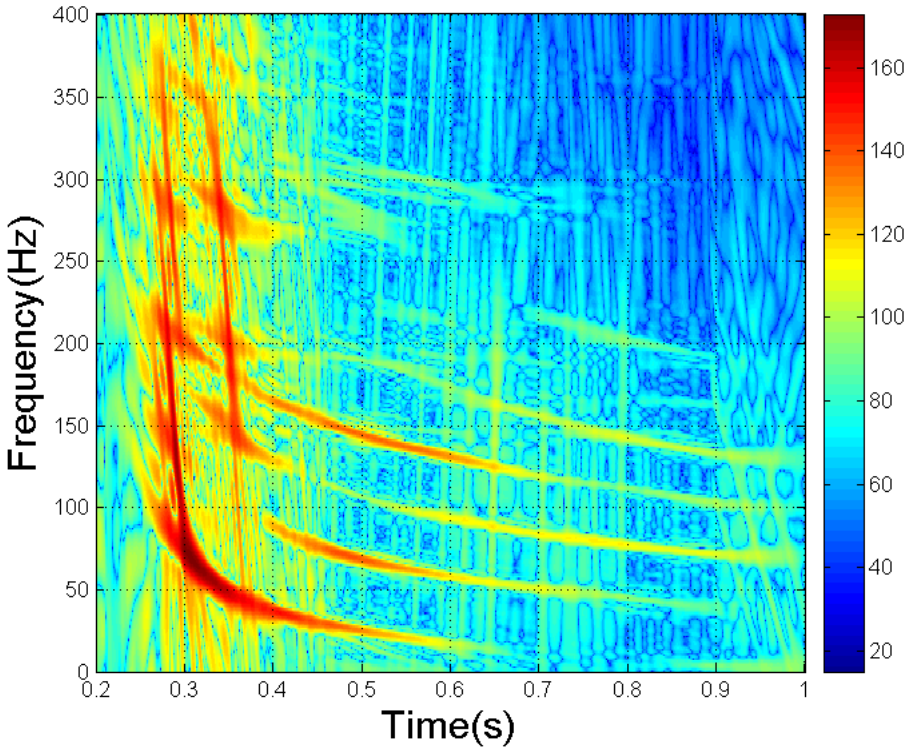

Figure 5.8 TFR of the time series shown in figure 5.7

5.2.3.2 Inverted results

The average group slowness differences K'_{tmn} as a function of frequency, extracted from the combined time series of 36 channels on the HLA portion of SWAMI52 at different distances by using time-frequency representation, are listed in Table 5.4. Inputting K'_{tmn} into Eq. (5.1), the cost L is minimized by the hybrid optimization approach shown in section 5.2.2. The search bounds and inverted results of multiple parameters (H0, H1, C1U, C1D and C2) are listed in Table 5.5. The theoretical group velocity dispersion curves are calculated using the inverted parameters and are shown in figure 5.9 by dashed lines. The calculated curves show good agreement with the extracted ones obtained by time-frequency representation of the broadband explosive signals.

Table 5.4 Extracted group slowness differences (SW '06)

f (Hz)	50	60	90		
K'_{t12} (s/m)	2.3896×10^{-5}	1.5956×10^{-5}	0.6151×10^{-5}		
f (Hz)	65	75	90		
K'_{t23} (s/m)	2.8981×10^{-5}	2.3277×10^{-5}	1.4519×10^{-5}		
f (Hz)	90	100	105	115	135
K'_{t34} (s/m)	2.9414×10^{-5}	2.2962×10^{-5}	2.1652×10^{-5}	1.7983×10^{-5}	1.1516×10^{-5}
f (Hz)	135	140	150	160	
K'_{t45} (s/m)	1.9296×10^{-5}	1.9024×10^{-5}	1.7240×10^{-5}	1.5375×10^{-5}	

Table 5.5 Search bounds and inverted results (SW '06)

	H0 (m)	H1 (m)	C1U (m/s)	C1D (m/s)	C2 (m/s)
Search Bounds	[65,80]	[1,50]	[1540,1700]	[1540,1800]	[1700,2100]
Inversion Results	70.8	21.8	1607.8	1795.4	1865.1

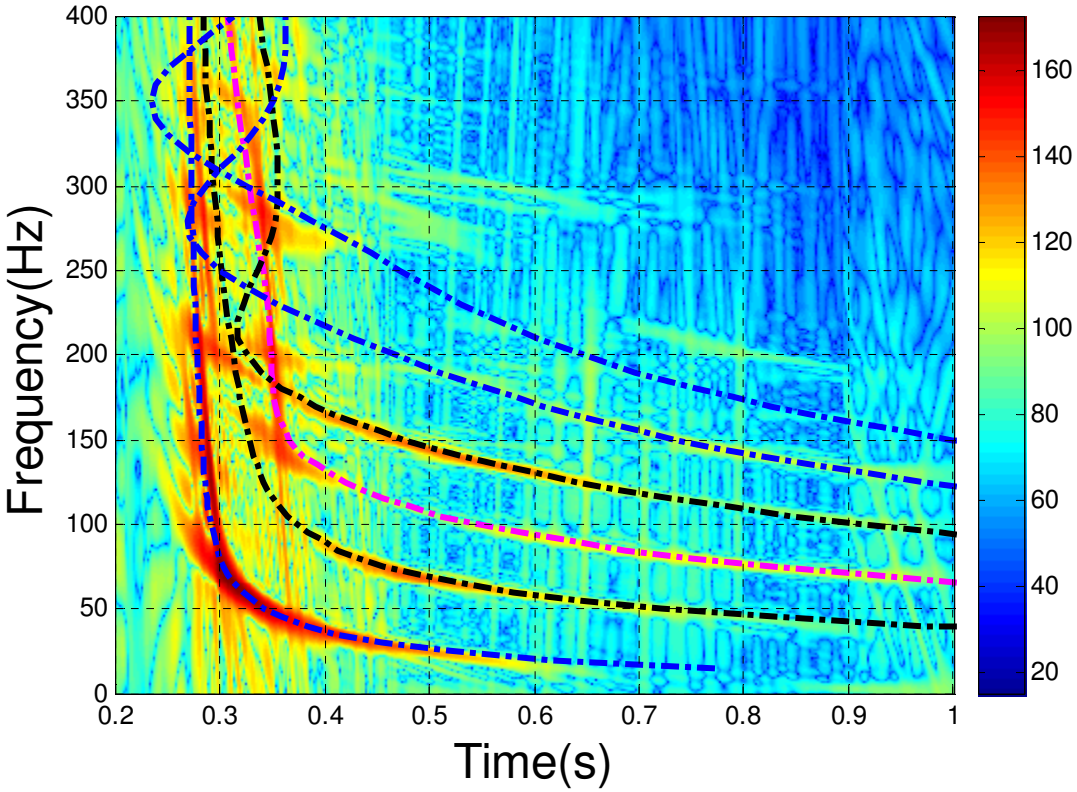

Figure 5.9 Comparison of extracted and calculated dispersion curves (Range=16.33 km, SD=50 m, RD= 70.8 m)

5.3 Seabed Sound Speed Inverted from Data-derived Mode Depth Functions

In section 4.2.1, data-derived mode depth functions obtained from CSDM were successfully used to invert the seabed sound speed in the YS '96 experiment. In this section, this inversion technique is used for sub-experiment one of the SW '06 experiment to estimate the sound speed right below the interface of water and the first bottom layer (C1U).

5.3.1 Mode extraction from VLA portion of SWAMI52

In SW '06, the VLA portion of SWAMI52 spanned nearly the entire water column and had dense element spacing. The water depth as obtained from section 5.2.3 was 70.8 m and the array spanned the depths between 11 m and 67.77 m with a spacing of 4.37 m (See Table 2.2c). The data from the VLA portion of SWAMI52 can be used to construct the CSDM. In this section, the bandwidth B is selected to be 8 Hz and the central frequency is selected to be 50Hz. There are 8 frequency bins within the bandwidth B. In our data processing, the fixed source-receiver distance r_0 is chosen to be 18.96 km along the BA track (See figure 2.9). Combustive sound source signals with a source depth of 25 m were measured on the VLA portion of SWAMI52 to form the CSDM. Recall from Chapter 4 that the eigenvectors of the CSDM correspond to the mode depth function. The extracted depth function for mode one is shown by circles in Fig. 5.10b.

5.3.2 Results of the CSDM-inverted sound speed (C1U)

The SSP used in the shooting method is shown in Fig. 5.10a. The cost function is calculated for the combustive sound source signal measured at a distance of 18.96 km on the BA track. The cost function for the first mode as a function of C1U at 50 Hz is shown

in figure 5.11. The inverted C1U at 50Hz is 1606.9 m/s at the minimum point of the cost function *F,* and the corresponding wave number for mode one at 50 Hz is 0.207346. The modeled first mode shape with a C1U of 1606.9 m/s at 50 Hz, calculated by the shooting method, is shown in figure 5.10b by a solid line. The modeled shape is in good agreement with the extracted one. The inverted C1U (1606.9m/s) in the CSDM-based method is close to the inverted C1U (1607.8m/s) in the dispersion-based method. The ratio of C1U to the sound speed in water column near the seabed is 1.079.

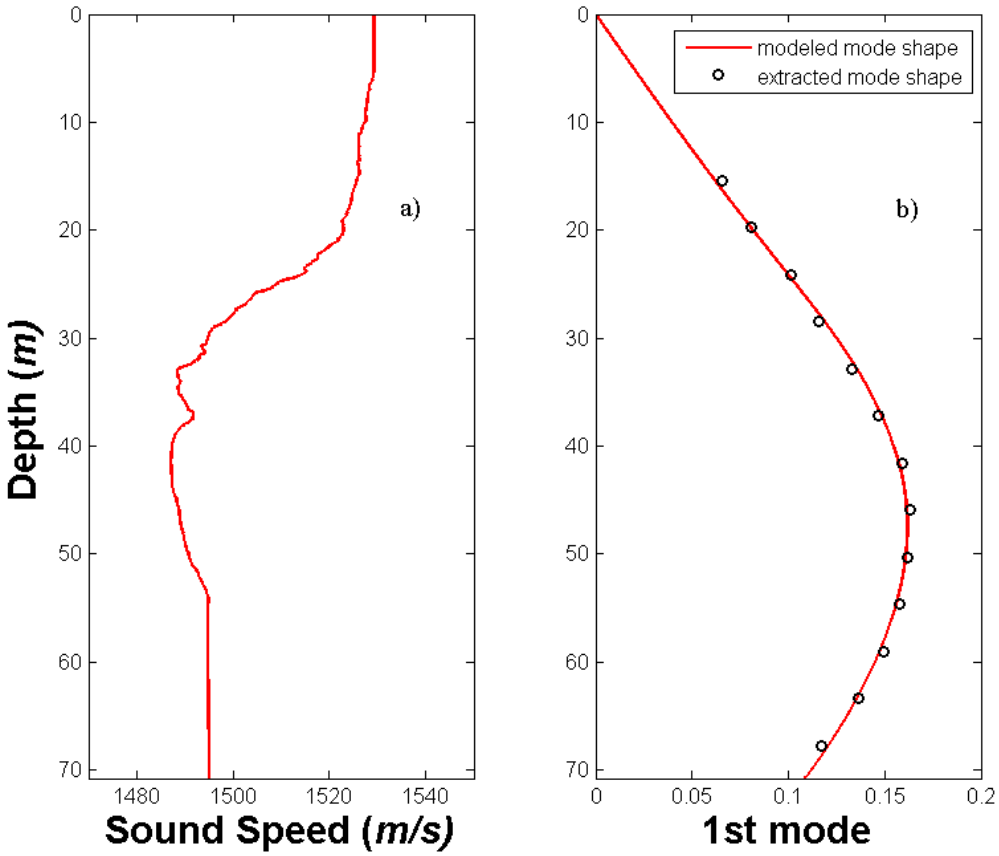

Figure 5.10 Comparison of extracted and modeled first mode shape (50Hz)

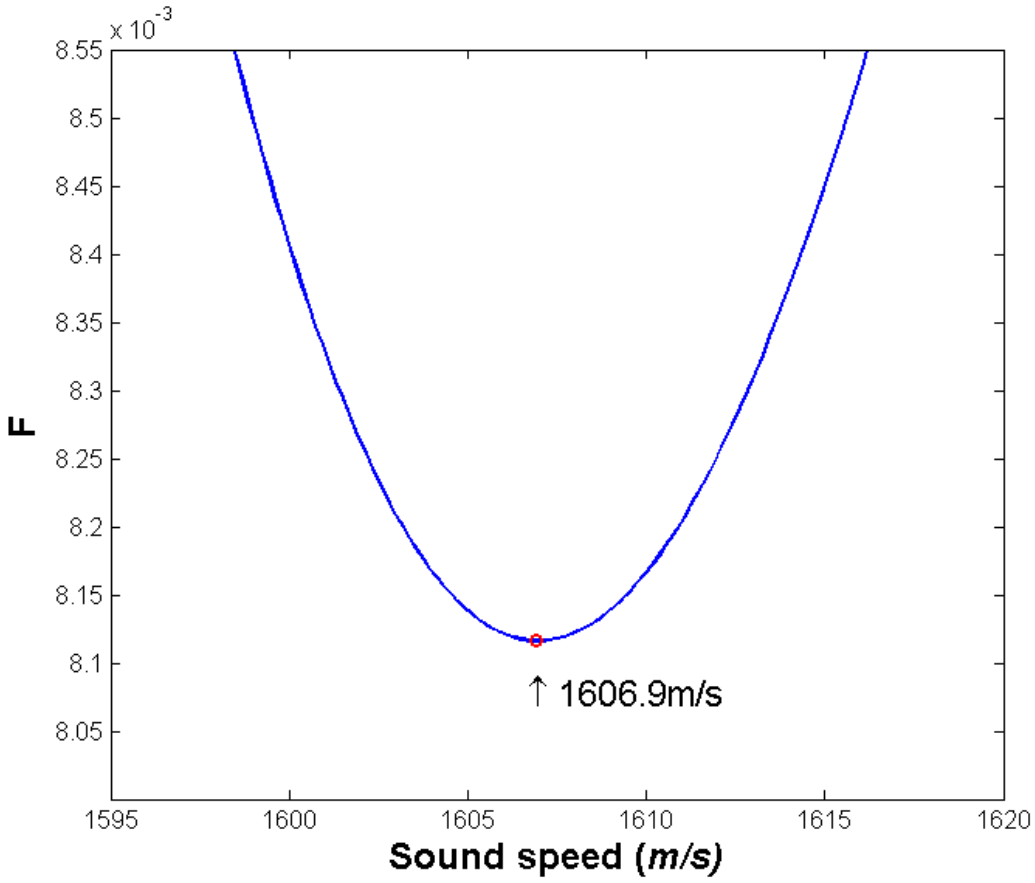

Figure 5.11 F as a function of C1U at 50 Hz

5.4 Seabed Attenuation Inverted from Measured Modal Amplitude Ratios

In SW ’06, the CSS signals with same source depth were detonated at only three or four ranges. Thus, measured modal attenuation coefficients and *TL* data will not be used to estimate the seabed attenuation for SW ’06.

In section 4.5.1, measured modal amplitude ratios were successfully used to invert the seabed sound attenuation for the YS ’96 experiment. In this section, the method is applied to sub-experiment one of SW ’06. The inverted results obtained in sections 5.2 and 5.3 are used as a constraint condition to estimate the sound attenuation in the seabed by matching the theoretical modal amplitude ratios with experimental data.

The ratios of the amplitudes of the second mode and third mode to the amplitude of the first mode ($R_{21}^{'}$ and $R_{31}^{'}$) were extracted at distances of 10.79 km, 16.33 km and 25.69km on the BA track over a frequency range of 63Hz to 400Hz. For example, Fig. 5.12 shows the received signal at 315 Hz when the source-receiver distance is 16.33 km. The source depth was 50 m and the receiver depth was 50.3 m. The first four modes can be identified in figure 5.12.

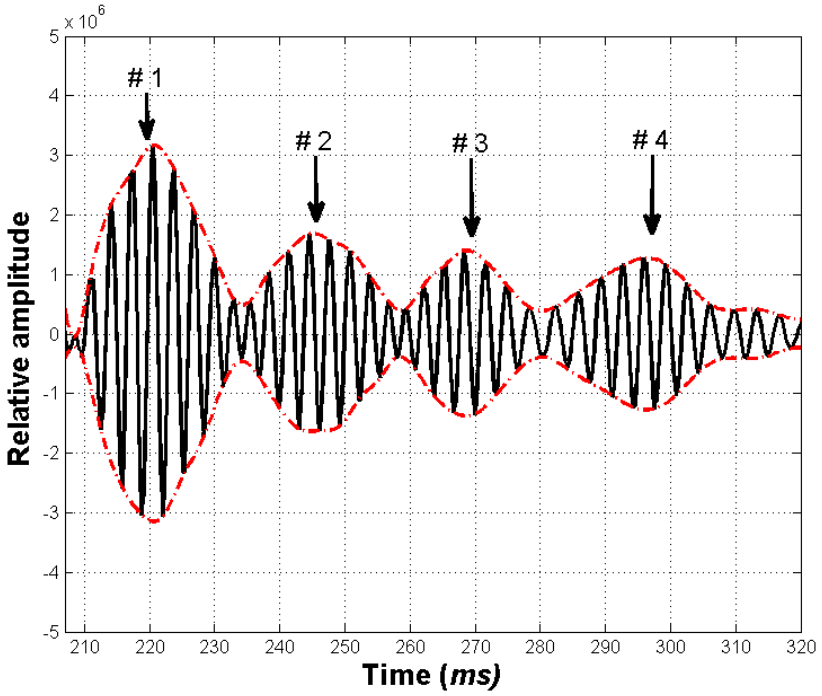

Figure 5.12 The received signal at 315 Hz when the source-receiver distance is 16.33 km.

Seabed attenuation is determined by minimizing the difference between the theoretical modal amplitude ratios and the measured modal amplitude ratios ($R_{21}^{'}$ and $R_{31}^{'}$). The inverted seabed attenuations over a frequency range of 63Hz to 400Hz are listed in Table 5.6 and shown in figure 5.13. The inverted seabottom attenuation shown in figure 5.13 can approximately be expressed by:

$$\alpha_b = (0.41 \pm 0.08) f^{1.82 \pm 0.10} (dB/m \cdot kHz) \qquad (5.2)$$

Table 5.6 Inverted seabed attenuation using measured modal amplitude ratios (SW '06)

f (Hz)	63	80	100	125	160	200	250	315	400
α_b (dB/m)	0.0028	0.0045	0.0059	0.0092	0.0090	0.0293	0.0355	0.0454	0.0812

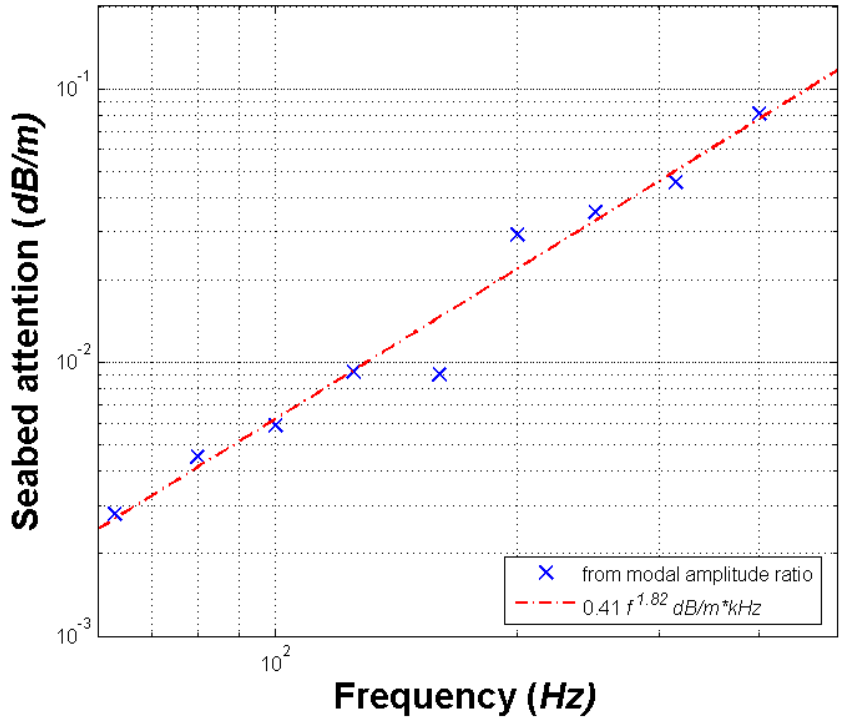

Figure 5.13 Sound attenuation in the bottom as a function of frequency (SW '06)

5.5 Comparison of Spatial Coherence Data with Predictions based on Inverted Seabottom Parameters

The spatial coherence of the sound field in shallow water is sensitive to the seabed parameters (Zhou *et al.* 2004). Measured spatial coherence can thus be used to validate the inverted seabottom parameters. The experimental configuration of sub-experiment one in SW '06 is shown in figure 2.12. Two L-shaped arrays (SWAMI32 and SWAMI52) were deployed. The constructions of SWAMI32 and SWAMI52 are shown in figures 2.10 and 2.11 and Table 2.2. The source ship traveled along the straight line connecting points A and B in figure 2.9. The HLA component of SWAMI52 was perpendicular to the direction of sound propagation. The HLA component of SWAMI32 was parallel to the direction of sound propagation. This configuration offered an opportunity to simultaneously analyze the three dimensional (3D) spatial coherence: vertical, transverse horizontal and longitudinal horizontal. The spatial coherence data as a function of frequency and range are analyzed and used to validate the inverted results obtained in sections 5.2, 5.3 and 5.4.

5.5.1 Spatial coherence measurements from SWAMI32 and SWAMI52 in the sub-experiment one of SW '06

5.5.1.1 Experimental data processing

Figure 5.14a shows the combustive sound source (CSS) signal received by the 52 hydrophones of SWAMI52 at a distance of 16.33 km. (hydrophone #18 of SWAMI52 did not work during the experiment). Figure 5.14b shows the same combustive sound source signal received by the 32 hydrophones of SWAMI32 at a distance of 4.79 km. The source depth was 50 m.

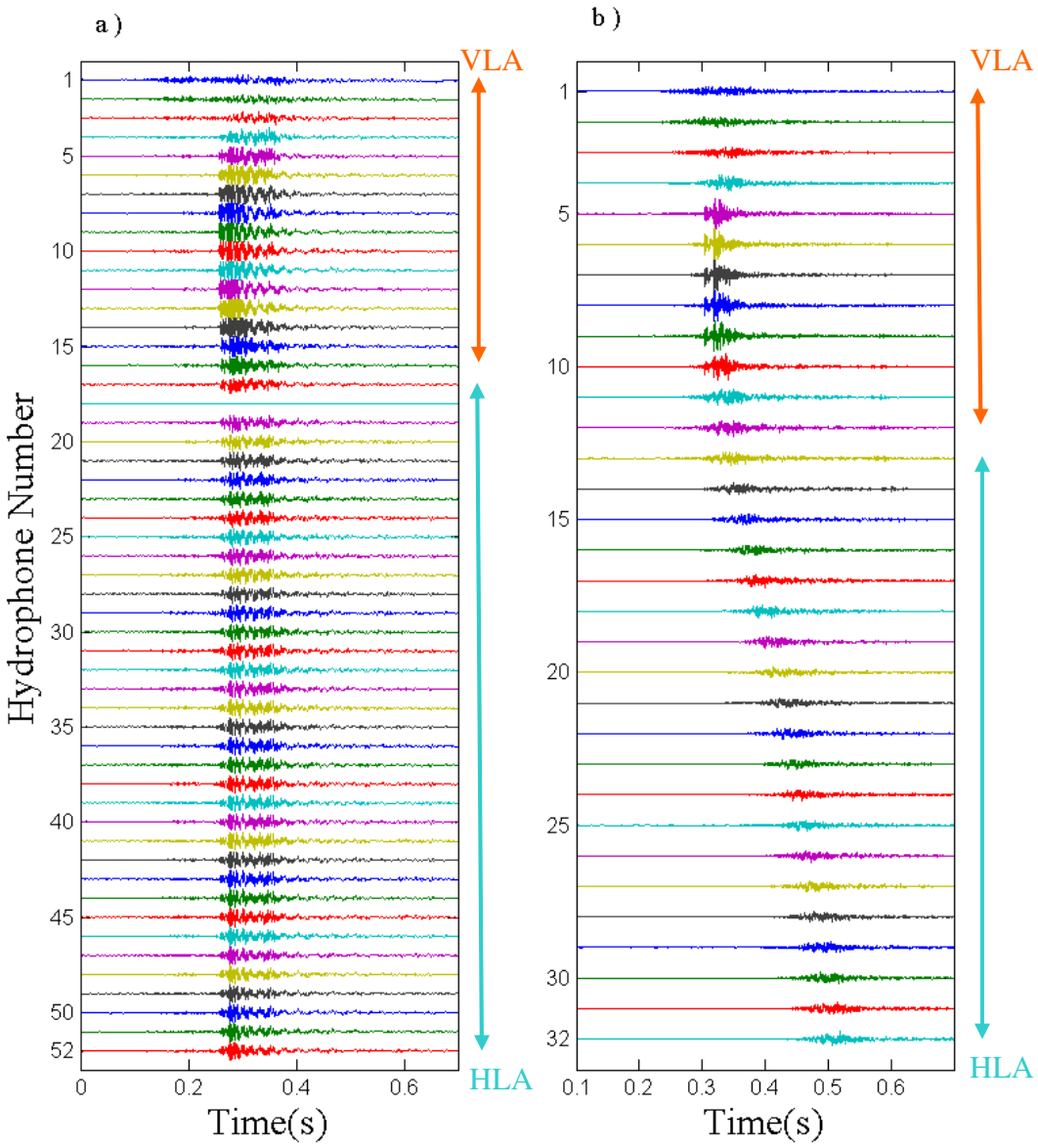

Figure 5.14 Combustive sound source signal received by a) SWAMI52 at a distance of 16.33 km; b) SWAMI32 at a distance of 4.79 km (SD=50 m).

Experimental spatial coherence in this chapter is defined as the normalized cross correlation between the sound pressures received at two spatially separated points. The mathematical expression for the experimental spatial coherence is shown in Eq. (5.3)

$$\rho(\Delta T,\tau)=\frac{\int_{t}^{t+\Delta T} p_1(t)\,p_2\,(t-\tau)dt}{\sqrt{\int_{t}^{t+\Delta T} p_1{}^2(t)dt\times\int_{t}^{t+\Delta T} p_2{}^2(t)dt}} \tag{5.3}$$

where, τ is the time delay and ΔT is the integration time. It can be seen from figure 5.14 that the time delay is zero for the vertical coherence. Since the HLA component of SWAMI52 was perpendicular to the direction of sound propagation, the time delay is zero for the transverse horizontal coherence. The HLA component of SWAMI32 was parallel to the direction of sound propagation, so the time delay for the longitudinal horizontal coherence is given by $\tau = L/c$, where L is the hydrophone separation and c is the sound speed. The spatial coherence is evaluated using an integration time 426.7 ms for SWAMI52 and 655.3 ms for SWAMI32 and is averaged over different pairs of hydrophones with the same separation in the water. In section 5.5.1.1, all presented data are evaluated for the stated center frequencies with a bandwidth of 100 Hz. In this section, the coherence length is defined as the separation between two receivers, expressed in units of the wavelength at the center frequency at which the spatial coherence falls below 0.5. The coherence length is a measure of the angular uncertainty caused by the transmitting medium.

An example is used here to explain the data processing. Figures 5.15a and 5.15b show the CSS time series received by the VLA portion of SWAMI32 at depths of 46.72 m and 52.68 m respectively, when the source depth was 35 m and the source-receiver

range was 10.8 km. Those CSS time series have high signal to noise ratio. The signals in Fig. 5.15a and Fig. 5.15b were filtered by a band pass filter with a center frequency of 300 Hz and a bandwidth of 100 Hz (See Fig. 5.16a and Fig. 5.16b). The normalized cross correlation function is evaluated by Eq. (5.3). Figure 5.17 shows the normalized cross correlation function. The spatial correlation coefficient for the two signals shown in Fig. 5.16 is seen to be 0.64.

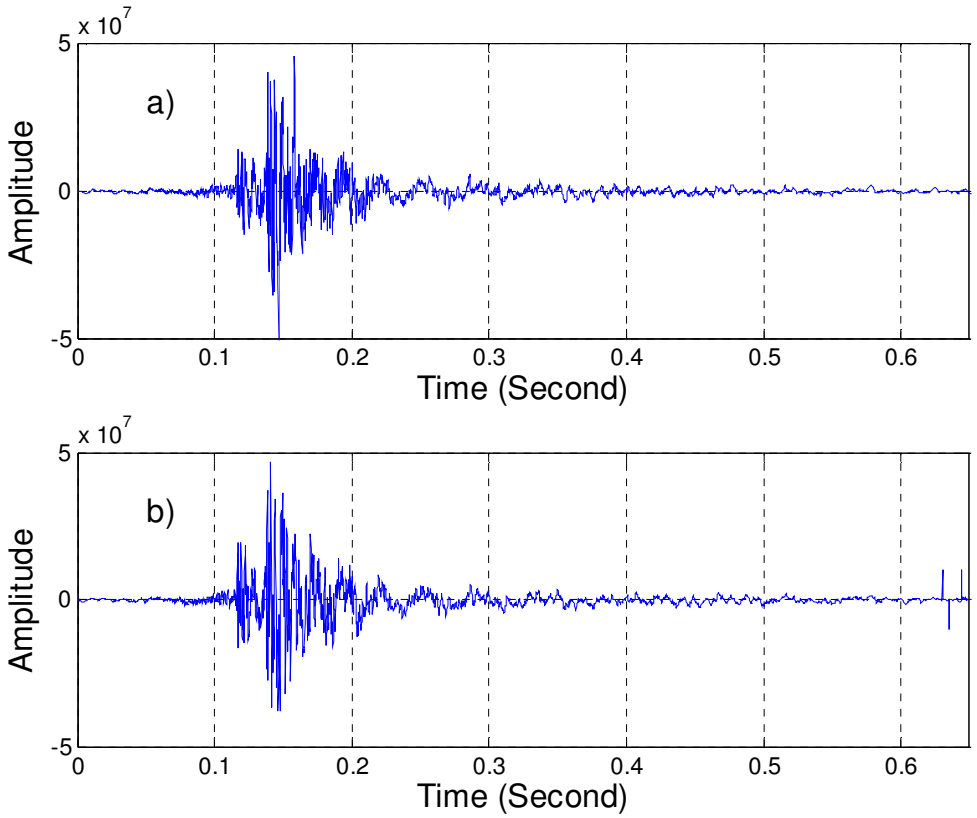

Figure 5.15. Measured CSS time series received by the VLA portion of SWAMI32. a) RD=46.72 m; b) RD=52.68 m.

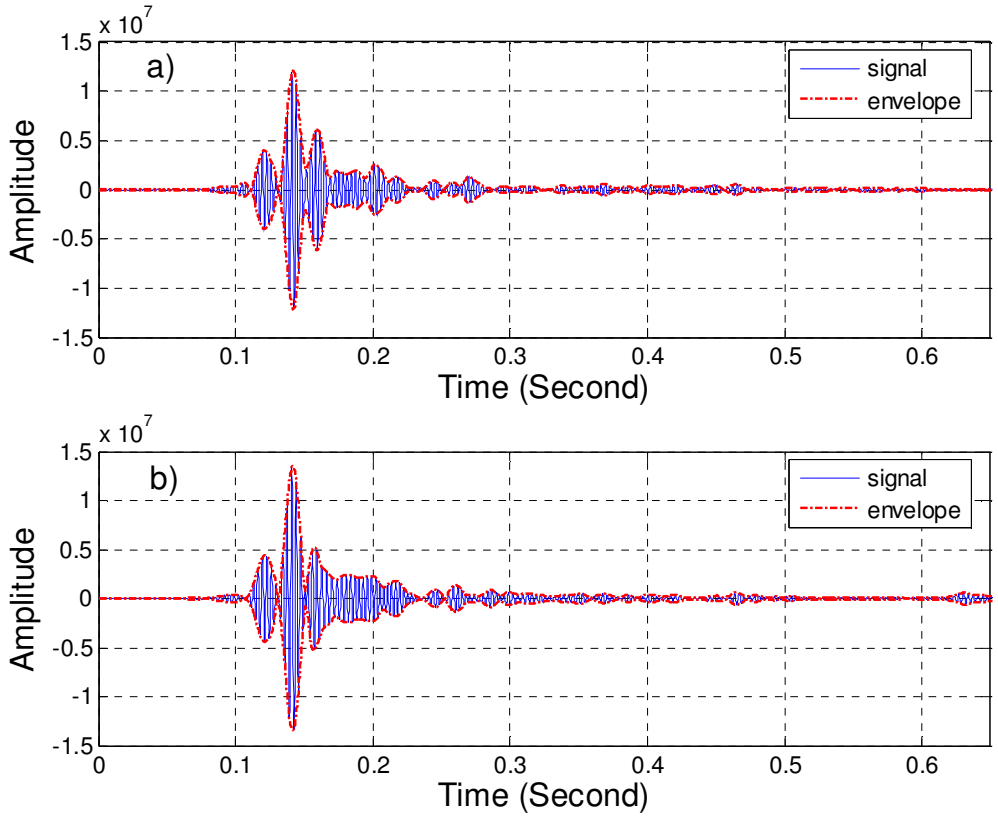

Figure 5.16 The measured CSS time series of Fig. 5.15 filtered by the band pass filter with a center frequency of 300 Hz and a bandwidth of 100 Hz.

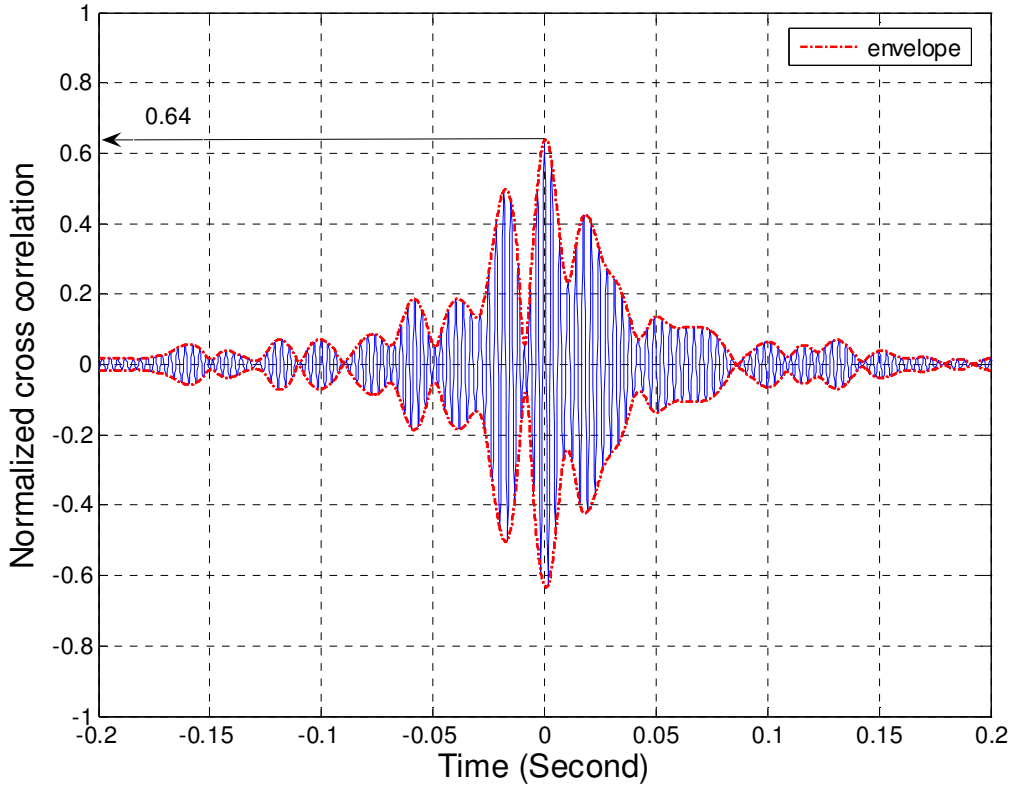

Figure 5.17 Normalized cross correlation function for two signals shown in Fig. 5.16.

5.5.1.2 Characteristics of observed spatial coherence

5.5.1.2.1 Range dependence of vertical coherence

Figure 5.18 shows the experimental results for vertical correlation coefficient as a function of hydrophone separation (in units of wavelength λ) at three different ranges (3.5 km, 7.7 km, and 10.8 km). The source was located at a depth of 35m, which was below the thermocline. The vertical correlation coefficient was averaged over data from six receivers which were below the thermocline. The center frequency was 100 Hz. The data show that the coherence lengths were 0.58 λ at 3.5 km, 0.81 λ at 7.7 km and 0.96 λ at 10.8 km. Figure 5.19 shows the measured vertical correlation coefficient as a function of range at three different frequencies (100 Hz, 200 Hz and 300 Hz). The hydrophone separation was 5.95 m. In Fig. 5.19, the measured vertical correlation coefficient at 200 Hz increased from -0.04 at a range of 0.8 km to 0.82 at a range of 10.8 km. Based on Fig. 5.18 and Fig. 5.19, the conclusion was drawn that the vertical coherence length in units of wavelength increases with range. This conclusion was also obtained by Galkin *et al.* (2004) and Jie Yang *et al*. (2007).

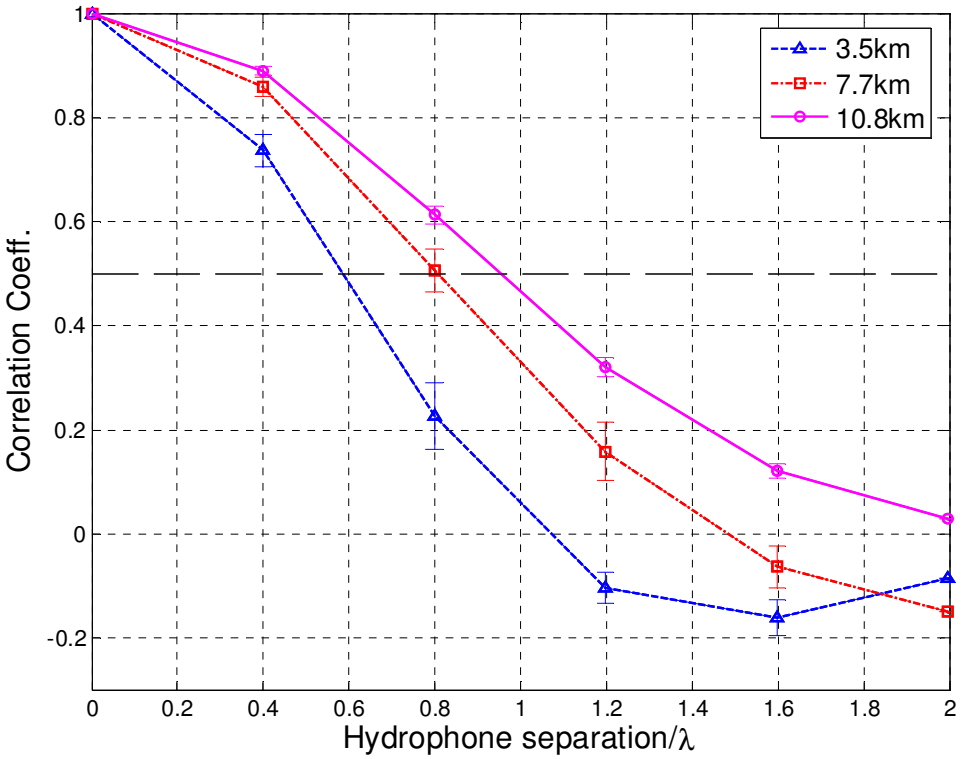

Figure 5.18 Vertical coherence at different ranges (SD=35 m and frequency = 100 Hz).

The error bars show the standard errors.

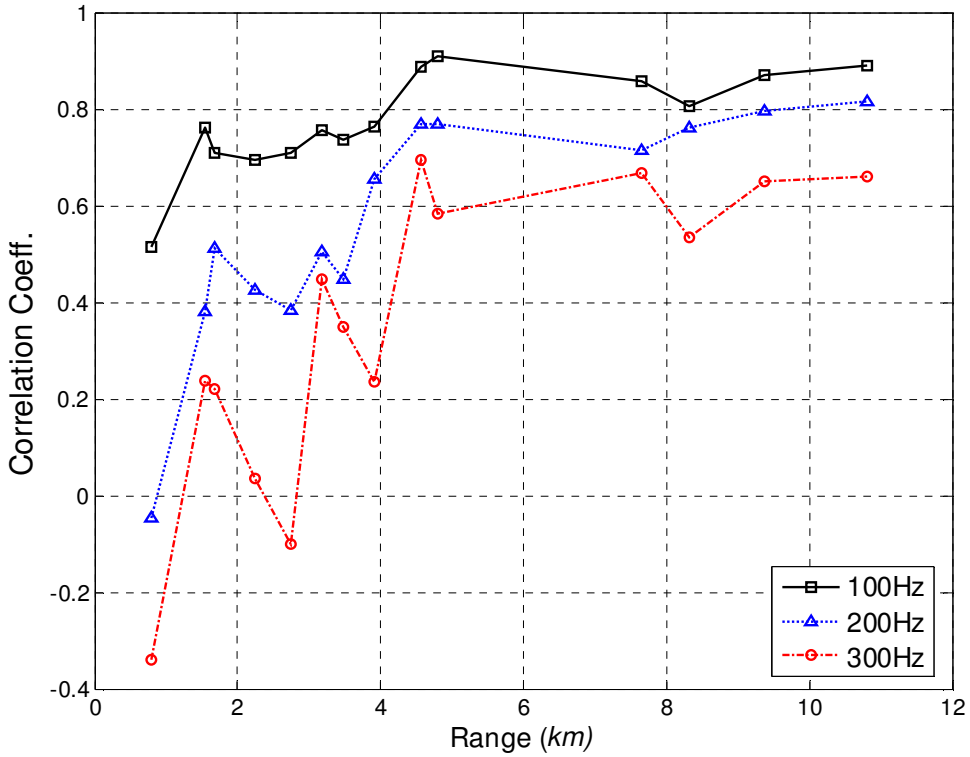

Figure 5.19 Vertical coherence as a function of range at different frequencies.

(Hydrophone separation is 5.95 m).

5.5.1.2.2 Frequency dependence of vertical coherence

Figure 5.20 shows the experimental results for vertical correlation coefficient as a function of hydrophone separation (in units of λ) at two different frequencies (100 Hz and 300 Hz). The source was located at a depth of 35m, which was below the thermocline. The vertical correlation coefficient was averaged over data from nine receivers which were located below the thermocline. The source-receiver range was 13.5 km. In Fig. 5.20, the coherence lengths were 0.87 λ at 100 Hz, 1.39λ at 200 Hz and 1.51 λ at 300 Hz from which it was concluded that the vertical coherence length in units of wavelength increases with frequency.

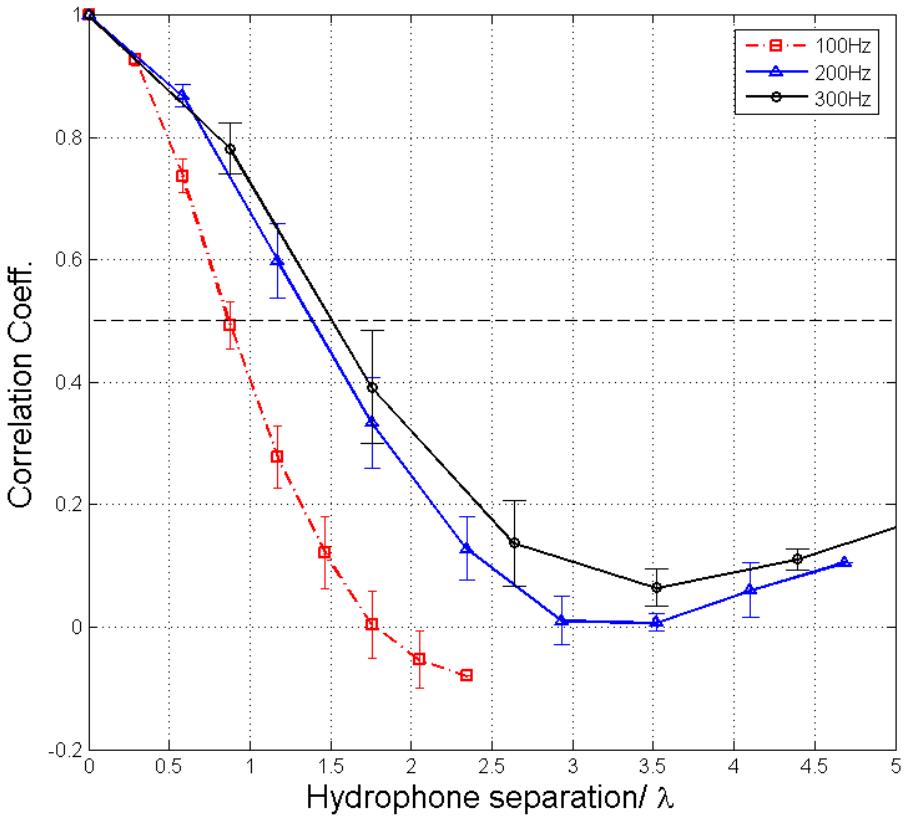

Figure 5.20 Vertical coherence at two different frequencies

(Range=13.5 km and SD=35 m).

5.5.1.2.3 Range dependence of longitudinal horizontal coherence

Figure 5.21 shows the measured longitudinal horizontal correlation coefficient as a function of hydrophone separation (in units of λ) at three different ranges (1.7 km, 4.8km, and 10.8 km). The center frequency was 300 Hz. In Fig. 5.21, the coherence lengths were 9.0 λ at a range of 1.7 km, 11.6 λ at a range of 4.8 km, and 17.4 λ at a range of 10.8 km. The longitudinal horizontal coherence length in units of wavelength increases with range.

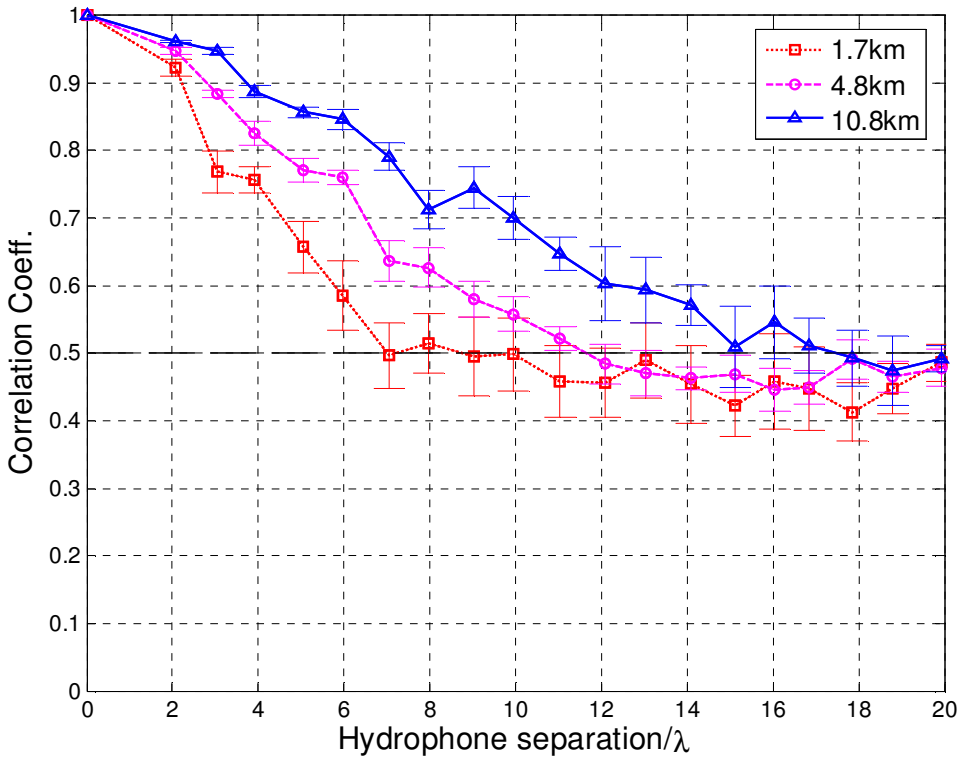

Figure 5.21 Longitudinal horizontal coherence at different ranges

5.5.1.2.4 Frequency dependence of longitudinal horizontal coherence

Figure 5.22 shows the results for longitudinal horizontal correlation coefficient as a function of hydrophone separation (in units of λ) at two different frequencies (100 Hz and 300 Hz). The source depth was 35 m. The source-receiver range was 7.7 km. In Figure 5.22, the coherence lengths were 7.18 λ at 100 Hz, 8.9 λ at 200 Hz and 12 λ at 300 Hz. The longitudinal horizontal coherence length in units of wavelength increases with frequency.

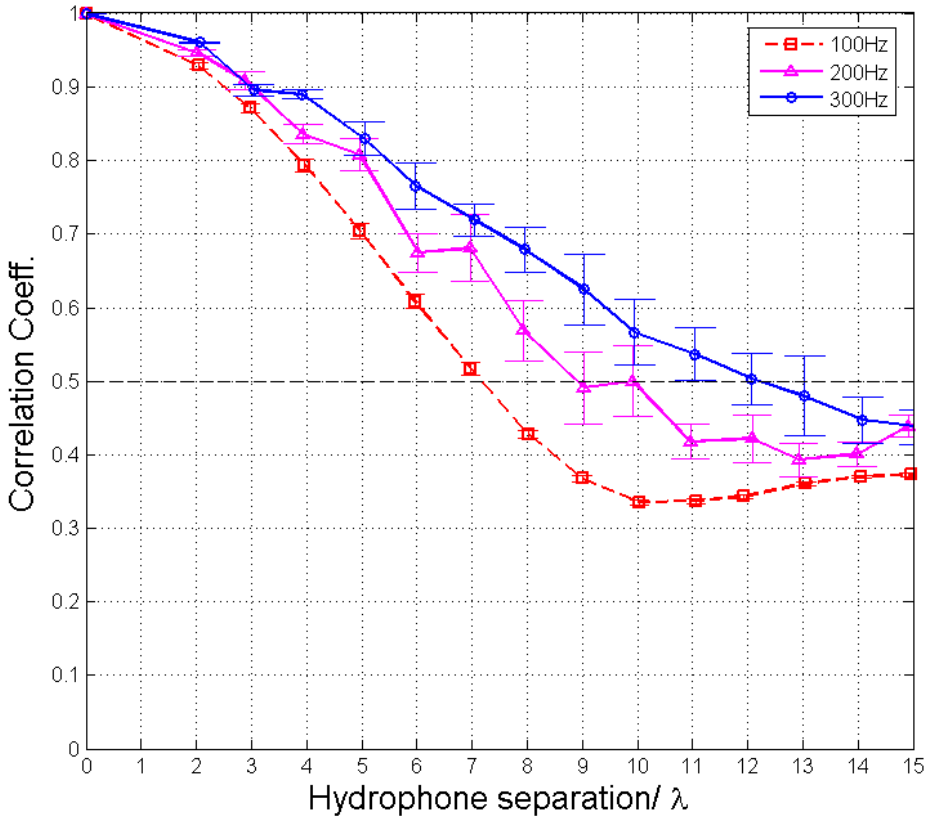

Figure 5.22 Longitudinal horizontal coherence at different frequencies

5.5.1.2.5 Range dependence of transverse horizontal coherence

Figure 5.23 shows the measured transverse horizontal correlation coefficient as a function of hydrophone separation (in units of λ) at four different ranges (5.8 km, 6.4 km, 8.8 km and 9.3 km). The center frequency was 200 Hz. The source depth was 25 m. In Fig. 5.23, the transverse horizontal coherence lengths were much larger than 35 λ. There was no apparent range dependence for the transverse horizontal coherence lengths.

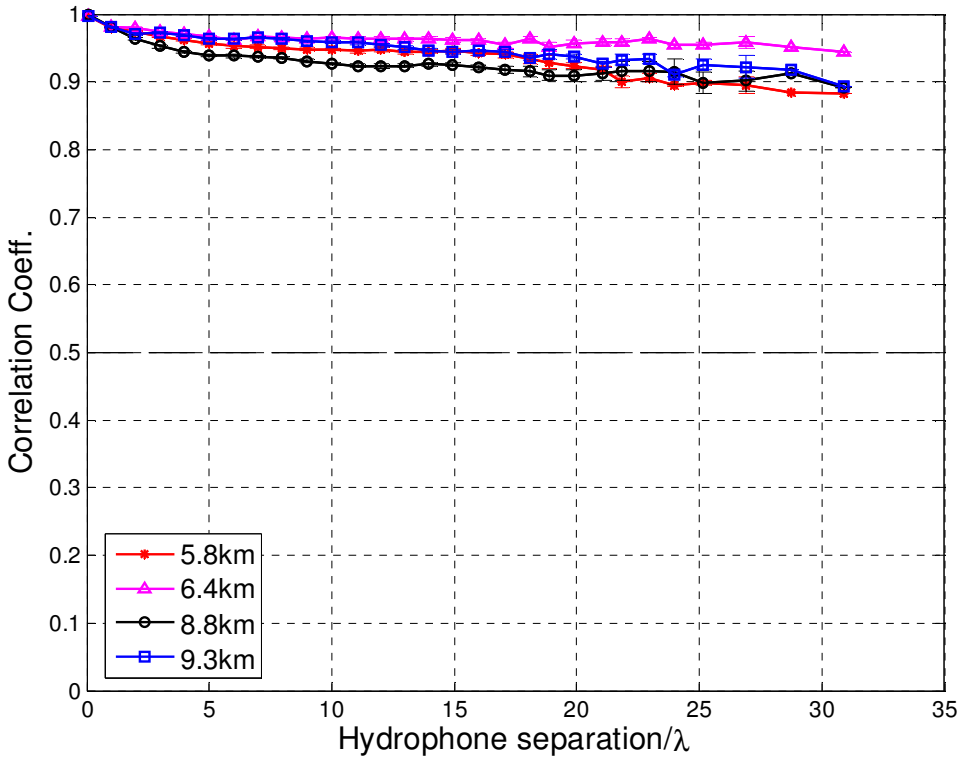

Figure 5.23 Transverse horizontal coherence at different ranges

5.5.1.2.6 Frequency dependence of transverse horizontal coherence

Figure 5.24 shows the results for transverse horizontal correlation coefficient as a function of hydrophone separation (in units of λ) at three different frequencies (100 Hz, 200 Hz and 300 Hz). The source was within the thermocline (SD=25 m). The source-receiver range was 8.8 km. Figure 5.24 shows the transverse horizontal coherence lengths were much larger than 40λ. These results agree with Carey's theoretical calculation (2006), in that they show a similar trend that the transverse horizontal coherence length in units of wavelength decreases with frequency.

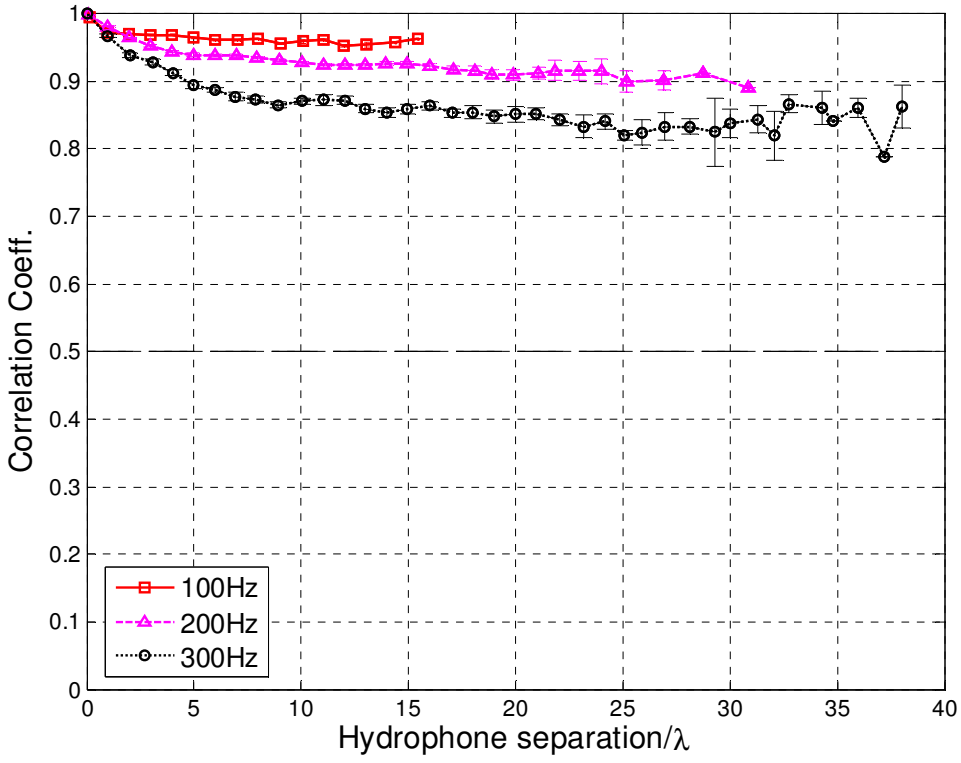

Figure 5.24 Transverse horizontal coherence at different frequencies

5.5.1.3 Physical explanation of observed coherence results

5.5.1.3.1 Vertical and longitudinal horizontal coherence

When both source and receiver are located below the thermocline, the spatial coherence at long-range for higher frequency should be similar to that in a Pekeris shallow water waveguide. According to Smith (1976), the vertical and longitudinal horizontal coherence length respectively can be expressed by

$$\rho_{vertical} = 0.265\lambda / \theta_{eff} \tag{5.4}$$

$$\rho_{longitudinal} = 1.23\lambda / \theta^2{}_{eff} \tag{5.5}$$

where, θ_{eff} is the effective grazing angle of the sound propagation. It can be expressed by

$$\theta_{eff} = \sqrt{\frac{H}{QR}} \tag{5.6}$$

where, H is the water depth, R is the range, Q is the bottom reflection loss factor in neper/rad. Q can be can written in the form (Weston, 1971; Buckingham, 1979)

$$Q = 2\frac{\left(\frac{c_{water}}{c_{bottom}}\right)^2\left(\frac{\rho_{bottom}}{\rho_{water}}\right)}{\left[1-\left(\frac{c_{water}}{c_{bottom}}\right)^2\right]^{3/2}} \times \beta \tag{5.7}$$

where, β is a measure of the seabottom attenuation in neper/rad.

β can be expressed by α_{bottom} in dB/m.kHz

$$\alpha_{bottom} = (20\log e)\left(\frac{2\pi f}{c_b}\beta\right) \tag{5.8}$$

Combining Eqs. (5.7) and (5.8), yields

$$Q = 0.0366 \frac{\left(\frac{c^2{}_{water}}{c_{bottom}}\right)\left(\frac{\rho_{bottom}}{\rho_{water}}\right)}{\left[1-\left(\frac{c_{water}}{c_{bottom}}\right)^2\right]^{3/2}} \times \frac{\alpha_{bottom}}{f} \tag{5.9}$$

In Eqs. (5.7), (5.8) and (5.9), c_{water} and c_{bottom} are the sound speeds in the water and bottom in units of km/s. ρ_{water} and ρ_{bottom} are the densities, α_{bottom} is the sound attenuation in the bottom (dB/m.kHz) and f is the frequency in kHz.

Due to mode stripping (higher modes with larger grazing angles suffer greater loss), the effective grazing angle of sound propagation decreases with increasing range. Using Eqs. (5.4) and (5.5), the vertical and longitudinal horizontal coherence lengths in units of wavelength increase with range at the same frequency.

In general, the bottom loss increases with frequency. For a given distance, the higher the frequency, the smaller the effective grazing angle. Using Eqs. (5.4) and (5.5), the vertical and longitudinal horizontal coherence lengths in units of wavelength increase with increasing frequency at the same distance.

The frequency dependence of the vertical and longitudinal horizontal coherence lengths, obtained when both source and receiver are located below the thermocline at long-range for higher frequency, can also be explained by a non-linear frequency dependence of seabed sound attenuation. If the attenuation has a non-linear frequency dependence and varies as f^n ($n \neq 1$), Q of Eq. (5.9) is frequency dependent and the vertical and longitudinal horizontal coherence lengths (in units of λ) are frequency dependent.

In section 5.5.2, the frequency dependence of vertical coherence lengths is verified by the theoretical calculation results of vertical coherence in SW '06. The theoretical results are calculated using the inverted results obtained in section 5.2, 5.3 and 5.4.

5.5.1.3.2 Transverse horizontal coherence

The transverse horizontal coherence is a measure of angle uncertainty of sound propagation in the horizontal plane, or a measure of signal phase fluctuations. In shallow water, degradation of the transverse horizontal coherence is mainly caused by water column inhomogeneity scattering and random boundary scattering. In contrast to the vertical and longitudinal horizontal coherence, the observed transverse horizontal coherence decreased with increasing frequency (See Fig. 5.24). This may be explained by the likelihood that water column inhomogeneity and random boundary scattering increased with increasing frequency in a 100-300 Hz range at the measurement site. (Wan *et al.*, 2009)

5.5.2 Theoretical calculation of vertical coherence in the sub-experiment one of SW '06

5.5.2.1 Mathematical expression

The mathematical expression for the theoretical vertical coherence is shown in Eq. (5.10)

$$\rho(z,\Delta z,r)=\frac{\left|\overline{p(z,r)p^{*}(z+\Delta z,r)}\right|}{\sqrt{\overline{\left|p(z,r)\right|^{2}}\,\overline{\left|p(z+\Delta z,r)\right|^{2}}}} \tag{5.10}$$

where, z is the receiver depth and Δz is the vertical separation of a pair of hydrophones.

Using the expression for sound pressure,

$$p(r,z) \approx \frac{i}{\rho(z_s)}\sqrt{\frac{1}{8\pi}}e^{(-i\pi/4)}\sum_{n=1}^{M}\Psi_n(z_s)\Psi_n(z)\frac{e^{ik_n r-\beta_n r}}{\sqrt{k_{n,c}r}} \tag{3.16}$$

The numerator in Eq. (5.10) becomes

$$\left|\overline{p(z,r)p^*(z+\Delta z,r)}\right| = \frac{1}{8\pi r\rho(z_s)}\left[\begin{array}{l}\sum_{n=m}\overline{\Psi_n(z_s)^2}\,\overline{\Psi_n(z)\Psi_n^*(z+\Delta z)}\frac{e^{-2\beta_n r}}{k_{n,c}} + \\ \sum_{n\neq m}\overline{\Psi_n(z_s)\Psi_n(z)\Psi_m^*(z_s)\Psi_m^*(z+\Delta z)}\frac{e^{i(k_n-k_m)r-(\beta_n+\beta_m)r}}{\sqrt{k_{n,c}k_{m,c}^*}}\end{array}\right] \tag{5.11}$$

The second term in Eq. (5.11) that describes the interference fine structure is often neglected. Eq. (5.11) becomes

$$\left|\overline{p(z,r)p^*(z+\Delta z,r)}\right| = \frac{1}{8\pi r\rho(z_s)}\left[\sum_{n=m}\overline{\Psi_n(z_s)^2}\,\overline{\Psi_n(z)\Psi_n^*(z+\Delta z)}\frac{e^{-2\beta_n r}}{k_{n,c}}\right] \tag{5.12}$$

where, $\overline{\Psi_n(z)\Psi_n^*(z+\Delta z)} = \overline{\Psi_n(z)^2}\cos[k(z)\Delta z\sin\theta_n(z)]$, $\cos\theta_n(z) = \frac{k_{n,c}}{k(z)}$, $k(z) = \frac{\omega}{c(z)}$.

Substituting Eq. (5.12) into Eq. (5.10), yields,

$$\rho(\Delta z,z,r) = \frac{\sum_n \overline{\left|\Psi_n(z_s)\right|^2}\,\overline{\left|\Psi_n(z)\right|^2}\cos[k(z)\Delta z\sin\theta_n(z)]\exp(-2\beta_n r)/k_{n,c}}{\sum_n \overline{\left|\Psi_n(z_s)\right|^2}\,\overline{\left|\Psi_n(z)\right|^2}\exp(-2\beta_n r)/k_{n,c}} \tag{5.13}$$

According to WKB approximation,

$$\overline{\left|\Psi_n(z)\right|^2} = \frac{2}{S_n\tan\theta_n(z)} \tag{5.14}$$

where S_n is the cycle distance of the nth normal mode.

If a receiver is near a turning point, $\tan\theta_n(z) \approx 0$, Eq. (5.14) can not be used. Instead, Zhang and Jin (1987) proposed the following expression

$$\overline{|\Psi_n(z)|^2} = \frac{1}{S_n[k^2(z)D(z) + k^2(z) - k_n^2]^{1/2}} \tag{5.15}$$

where, $D(z) = 0.875\left|\frac{1}{\pi f}\frac{dc(z)}{dz}\right|^{2/3}$ (5.16)

Therefore, the theoretical vertical coherence as given by Eq. (5.13) can be calculated using KRAKEN.

5.5.2.2 Data-Model comparison

Using the inverted results obtained in sections 5.2, 5.3 and 5.4, the theoretical vertical coherence is evaluated for the ranges and depths where the experimental data were measured. The source was located at a depth of 35 m, which was below the thermocline. The vertical correlation coefficient was averaged over data from six receivers, below the thermoline (the #5 through #10 hydrophones of SWAMI32). Figures 5.25 and 5.26 show the data-model comparison for vertical coherence when source-receiver distance was 3.18 km at 100 Hz and 400 Hz, respectively. The theoretical vertical coherence lengths are 0.54 λ at 100 Hz and 0.98 λ at 400 Hz. Those two figures show good agreement between model and data. This agreement indicates that the frequency dependence of the vertical coherence lengths can be verified by a non-linear frequency dependence of inverted seabed sound attenuation expressed by Eq. (5.2).

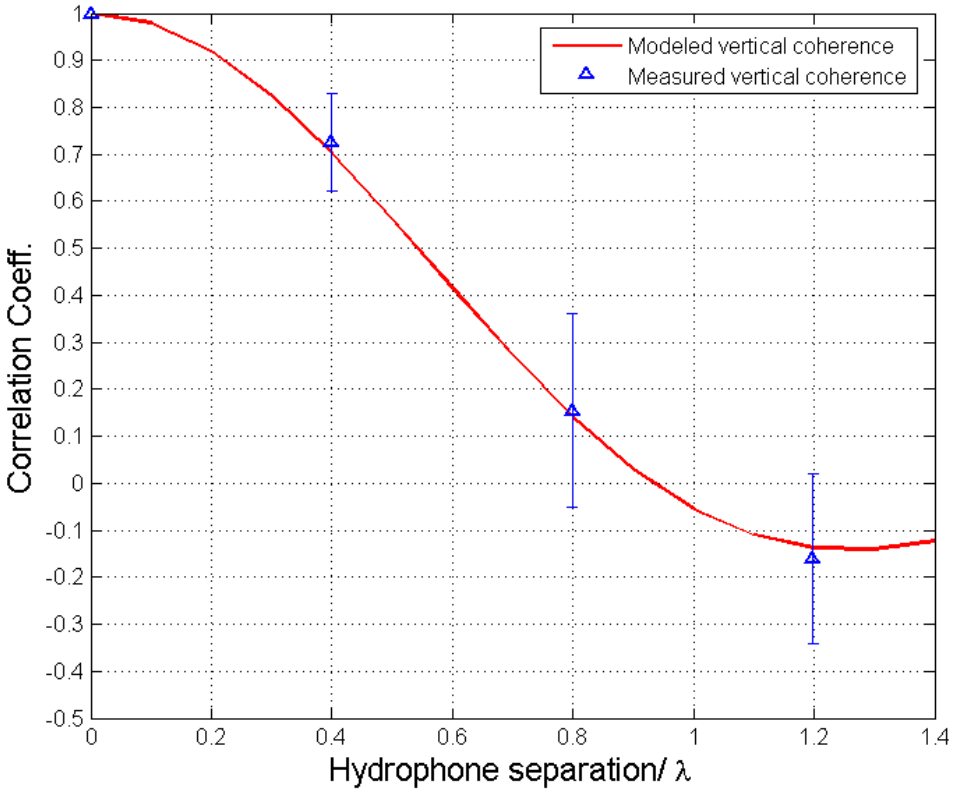

Figure 5.25 Data-model comparison for vertical coherence at 100 Hz (Range=3.18 km)

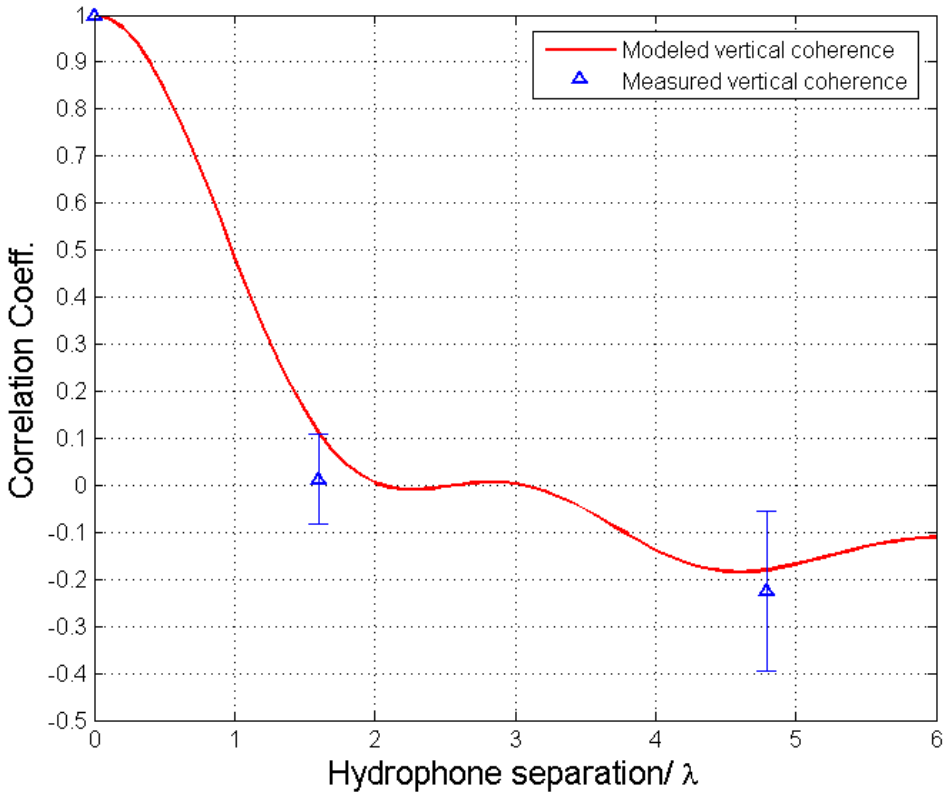

Figure 5.26 Data-model comparison for vertical coherence at 400 Hz (Range=3.18 km)

5.6 Comparison of Transmission Loss Data with Predictions based on Inverted Seabottom Parameters

Seabottom parameters obtained by inversion in sections 5.2, 5.3, and 5.4 are validated by comparing transmission loss data with predictions along track 1 and track 2 for sub-experiment two of Shallow Water '06 experiment (shown in figure 2.16). In sub-experiment two, one L-shaped array (Shark) was deployed. The construction of Shark is shown in figures 2.15 and Table 2.3. Research vessel Sharp deployed a J15 sound source, which transmitted chirp signals, at depth of 43 m along track 1 and track 2 between 21:05 UTC on August 11, 2006 and 05:17 UTC on August 12, 2006. Track 1 passed obliquely across the shelf, and its bathymetry was range dependent. Track 2 was along the shelf with a water depth of 80 m and was range independent.

Transmission loss data at 160 Hz as a function of range along track 2 and track 1 were obtained by averaging the spectrum in a 1/3-octave band and are shown as circles in figure 5.27 and 5.28, respectively. The receiver depth was 24.75 m. The error bars show the standard deviation of the *TL* data obtained from eleven chirp signals at each distance.

The theoretical incoherent *TL* at 160 Hz (solid line in figure 5.27) along track 2 was obtained using a range independent normal mode calculation. The SSP measured at the location of Shark array (see the very left panel in Fig. 3.6) and the inverted seabed parameters were used for the *TL* calculation along this range independent track. The theoretical *TL* at 160 Hz (solid line in figure 5.28) along track 1 with the bathymetric change shown in figure 3.7 was obtained using RAM (Collins, 1997). The SSPs (see Fig. 3.6) and the inverted seabed parameters were used for the *TL* calculation along this range dependent track. Figures 5.27 and 5.28 show good agreement between model and data.

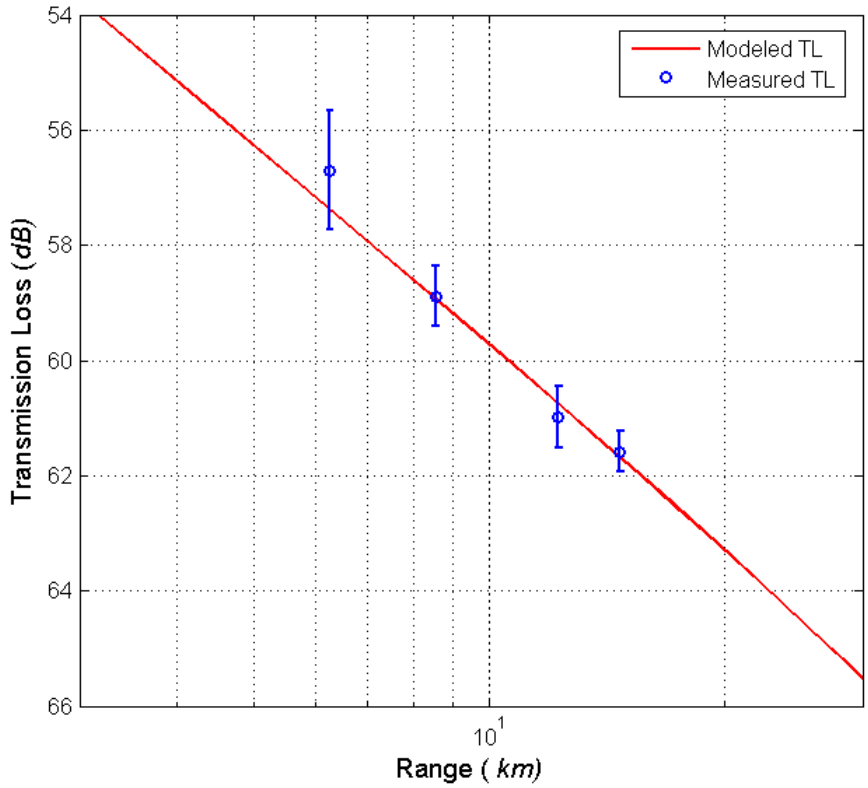

Figure 5.27 Comparison of measured *TL* with predictions as a function of range along the range independent track (track 2) at 160 Hz when SD=43 m and RD=24.75 m

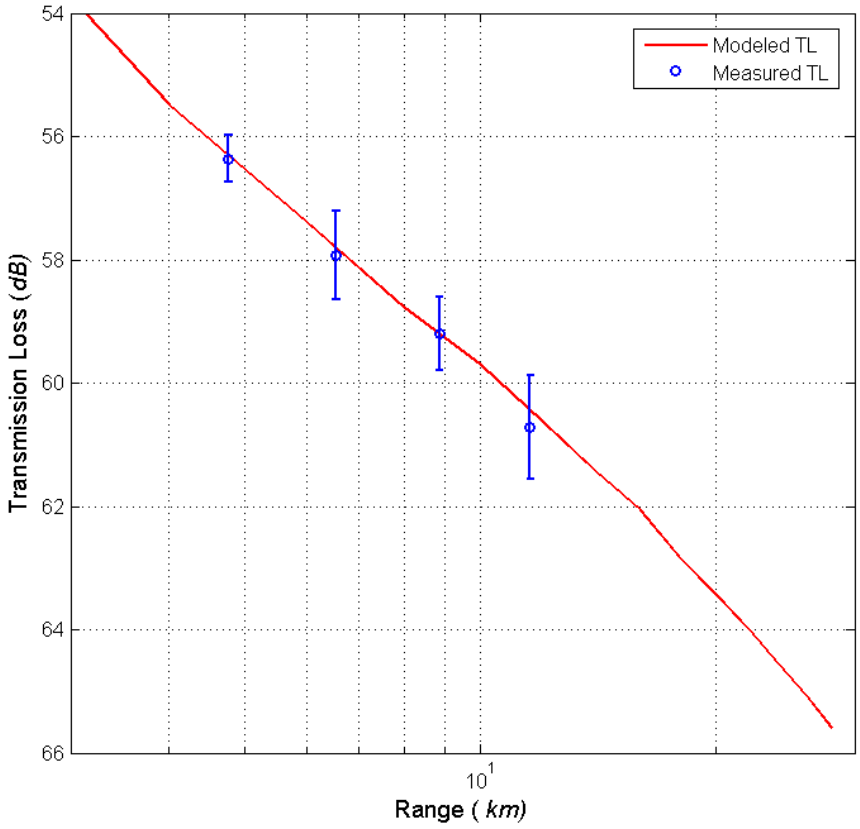

Figure 5.28 Comparison of measured *TL* with predictions as a function of range along the range dependent track (track 1) at 160 Hz when SD=43 m and RD=24.75 m

CHAPTER 6

CONCLUSIONS AND RECOMMENDATIONS

6.1 Summary of this Research

The validity of Hamilton model and Biot-Stoll model in sandy bottoms at low frequencies (LFs) can be tested using convincing experimental data. But the frequency dependence of the seabottom sound attenuation at LFs is still an open question in the ocean acoustics community because of the lack of enough convincing experimental results. In this research, geo-acoustic parameters are inverted by matching different characteristics of the measured sound field with a simulated sound field. More convincing experimental results are obtained from long range broadband acoustic measurements in YS '96 and SW '06 using the data derived mode shape, measured modal attenuation coefficients, measured modal arrival times, measured modal amplitude ratios, measured spatial coherence, and *TL* data.

Two inversion techniques are used to obtain the sound speed in the seabottom at the Yellow Sea '96 experimental site. One method is based on extracting the normal mode depth functions from the CSDM, which is constructed by processing broadband explosive signals measured with a long, densely populated vertical line array in multi-frequency bins at a fixed long range. The CSDM-inverted seabottom sound speed is 1593 m/s at 100 Hz. The other inversion method for seabottom sound speed is to extract the modal arrival times using time-frequency representation. The seabottom sound speed is inverted by matching the calculated dispersion curves with the experimental data. The inverted seabottom sound speed by time-frequency representation is 1587 m/s in a

frequency band (150 Hz-400 Hz). The average seabottom sound speed determined by these two inversions is 1588 m/s and the ratio of the seabottom sound speed to the sound speed in water column near the seabed is 1.073. Using the resultant averaged sound speed of 1588 m/s in the seabottom as a constraint condition, a seabed sound attenuation is obtained by three inversion methods. The first inversion method is used to estimate the seabed sound attenuation by finding the best match between the measured and modeled modal attenuation coefficients of the first three modes over a frequency range of 100Hz to 400Hz. The second inversion approach for attenuation is based on modal amplitude ratios of the 2^{nd}, 3^{rd} and 4^{th} mode relative to the 1^{st} mode. The seabed attenuations as a function of frequency from 160 Hz to 400 Hz are obtained. In the third inversion method, the seabed attenuations are inverted by minimizing the difference between the modeled *TL* and measured *TL* from 80 Hz to 1000 Hz. The resultant sound attenuation in the seabottom clearly exhibits nonlinear frequency dependence shown in Eq. (4.41)

$$\alpha_b = (0.33 \pm 0.02) f^{1.86 \pm 0.04} (dB/m \cdot kHz) \tag{4.41}$$

In the SW '06 experiment, a bottom model with two sediment layers is used. Based on the dispersion characteristics of broadband signals, the multiple unknown parameters (sediment layer depth, seabed sound speed in each sediment layer, and water depth) are inverted by using the hybrid optimization method to minimize the cost function. Both the CSDM-based inversion and the dispersion-based inversion are used to estimate the sound speed right below the interface of water and the first bottom layer (C1U), which is around 1607 m/s. The ratio of C1U to the sound speed in the water column near the seabed is 1.079. Using the resultant parameters as a constraint condition, the seabed sound attenuation over a frequency range of 63Hz to 400Hz is inverted from

measured modal amplitude ratios. The resultant sound attenuation in the seabottom clearly exhibits nonlinear frequency dependence as shown in Eq. (5.2)

$$\alpha_b = (0.41 \pm 0.08) f^{1.82 \pm 0.10} (dB/m \cdot kHz) \qquad (5.2)$$

Experimental vertical and horizontal spatial coherence data were collected by SWAMI52 and SWAMI32 during the Shallow Water '06 acoustic experiment. Based on the experimental results, the following conclusions regarding coherence were reached: When the source is located below the thermocline, the vertical coherence length in units of wavelength increases with range and frequency. The typical vertical coherence length is of the order of one acoustic wavelength. The longitudinal horizontal coherence length in units of wavelength increases with range and frequency. The typical longitudinal horizontal coherence length is approximately 10-20 acoustic wavelengths. The longitudinal horizontal coherence length is much larger than the vertical coherence length. The transverse horizontal coherence length in units of wavelength decreases with frequency. At the Shallow Water '06 site with downward refraction conditions, when the source depth was 25 m, the transverse horizontal coherence length did not exhibit apparent range dependence. The transverse horizontal coherence was larger than 40 wavelengths at both 200 Hz and 300 Hz.

The spatial coherence of the sound field in shallow water can be used to validate the inverted seabed parameters. The experimental results for vertical coherence at the SW '06 site are in good agreement with predictions based on the inverted seabed parameters. TL data as a function of range along the range independent track and the range dependent track are compared with the theoretical results to validate the inverted seabed parameters.

6.2 Contributions

Ocean acoustics is an observationally driven science. Thus, ocean acousticians should not forget the essence of the science, which is discovery-oriented research. Following this principle, much time was spent on comprehensive at-sea data analyses. The contributions of this research to the field can be summarized as follows.

1. The debate on the frequency dependence of the sound attenuation in the seabottom persisted for decades. In this research, the experimental data obtained from long range broadband acoustic measurements support a non-linear frequency dependence of seabed attenuation over a frequency range of 80-1000Hz in YS '96 (Wan *et al*., 2010) and over a frequency range of 63Hz-400Hz in SW '06.

2. The vertical and longitudinal horizontal coherence length (in units of λ) is independent of frequency. This has been the conventional thinking of the underwater acoustics community for many years. However, the experimental data of this research show that the vertical and longitudinal horizontal coherence length (in units of λ) increase with increasing frequency, which can be explained by a seabottom model with a non-linear frequency dependence of attenuation (Wan *et al*., 2009).

3. Spatial coherence measurements obtained during the Shallow Water '06 experiment using light bulb and combustive sound sources are presented. The vertical coherence was obtained as a function of range, frequency, and receiver depth. The longitudinal horizontal coherence and transverse horizontal coherence were obtained as a function of range and frequency. This is the first research to simultaneously report the three dimensional characteristics of spatial coherence at one site in shallow water (Wan *et al*., 2008).

6.3 Future Recommendations

This research has provided additional experimental results to test the validity of seabed geo-acoustic models. The results presented in this research suggest a number of research issues for the continuing work.

1. Most geo-acoustic inversion experiments have been conducted in areas with water depths larger than 70 m, which only allow one to successfully invert for seabed sound speed and attenuation for the lower frequencies (< 1000 Hz). The shallower the water depth, the more reliable the geo-acoustic inversion results (Zhou *et al*., 2009). Therefore, a low-frequency inversion experiment together with mid- to high frequency direct measurements at a shallower area (~20 m) is desirable to obtain quality data on seabed sound speed and attenuation from one site for a frequency band that covers a portion of the low frequency to high frequency.

2. The characteristics of 3D spatial coherence obtained in the SW '06 experiment can be further studied by analytical models and numerical simulations. Zhou *et al.* (2004) derived a mathematical model for shallow water vertical coherence of sound propagation and reverberation. Zhu *et al.* (1992) presented an analytical derivation for the transverse horizontal coherence by using the concept of horizontal rays and vertical modes and by adiabatic approximation. Those models can be used in conjunction with oceanographic models, containing a sea surface roughness model, a stochastic model for internal waves (both time-space varying), and an effective seabed geo-acoustic model, to develop analytical expressions for 3D temporal and spatial coherence.

REFERENCES

Badiey, M., Jaya, I., Pulaski, M. and Cheng, A., "Shallow-water acoustic/geoacoustic experiments at the New Jersy Atlantic Generating Station site," J. Acoust. Soc. Am., V96, 3593-3604, 1994.

Biot, M. A., "Theory of Propagation of Elastic Waves in a Fluid-Saturated Porous Solid. I. Low-Frequency Range". J. Acout. Soc. Am., V28, 168-178, 1956.

Biot, M. A., "Theory of Propagation of Elastic Waves in a Fluid-Saturated Porous Solid. II. High-Frequency Range". J. Acout. Soc. Am., V28, 178-191, 1956.

Biot, M. A., "Generalized Theory of Acoustic Propagation Porous Media". J. Acout. Soc. Am., V34, 1254-1264, 1962.

Boyles, C. A., *Acoustic Waveguides*, Wiley, New York, 1984.

Buckingham, M. J., "Array gain of a broadside vertical line array in shallow water," J. Acoust. Soc. Am. V65, 148-161, 1979.

Carey, W. M., "The determination of signal coherence length based on signal coherence and gain measurements in deep and shallow water," J. Acoust. Soc. Am. V104, 831-837, 1998.

Carey, W. M., Lynch, J. F., Siegmann, W. L., Rozenfeld, I., and Sperry, B. J., "Sound transmission and spatial coherence in selected shallow-water areas: measurement and theory," Journal of Computational Acoustics, V14, No. 2, 265–298, 2006.

Chapman, D. M. F., "what are we inverting for," in *Inversion Problems in Underwater Acoustics*, edited by M. I. Taroudakis and G. N. Makrakis, Spinger, New York, pp. 1-14, 2001.

Collins, M. P., "A split-step Padé solution for the parabolic equation method", J. Acoust. Soc. Am. V93, 1736-1742, 1993.

Collins, M. P., "User's Guide for RAM Versions 1.0 and 1.0P", Naval Research Lab., Washington D. C., 1997.

Cron, B. F. and Sherman, C. H., "Spatial-correlation functions for various noise models," J. Acoust. Soc. Am. V34, 1732-1736, 1962.

Dahl, P. H. and Choi, J. W., "Precursor arrivals in the Yellow Sea, their distinction from first-order head waves, and their geoacoustic inversion," J. Acoust. Soc. Am. V120, 3525-3533, 2006.

Dediu, S. M., Siegmann, W. L., and Carey, W. M., "Statistical analysis of sound transmission results on the New Jersey continental shelf," J. Acoust. Soc. Am. V122, EL23-EL28, 2007.

Efron, B. and Tibshirani, R., "Bootstrap method for standard errors, confidence intervals, and other measurements of statistical accuracy," Stat. Sci. V1, 54-77, 1986.

Evans, R. B., "A coupled mode solution for acoustic propagation in a waveguide with stepwise depth variations of a penetrable bottom," J. Acout. Soc. Am., V74, 188-195, 1983.

Ewing, W. M., Jardetzky, W. S., and Press, F., *Elastic Waves in Layered Media*, McGraw-Hill, New York, 1957.

Fock, V. A., *Electromagneric Diffraction and Propagation Problems*, Pergamon, New York, pp. 213-234, 1965.

Frisk, G. V., "Report on the Office of Naval Research Shallow Water Acoustics Workshop," Woods Hole, Massachusetts, 1991.

Galkin, O. P., Popov, R. Yu., and Simakina, E. V., "Spatial Correlation of Sound Field from Underwater Explosions in the Barents Sea," Acoustical Physics, V50, 37-43, 2004.

Gerstoft, P, "Inversion of seismo-acoustic data using genetic algorithms and a posteriori probability distributions," J. Acoust. Soc. Am. V95, 770—782, 1994.

Gerstoft, P., "Inversion of acoustic data using a combination of genetic algorithms and the Gauss-Newton approach," J. Acoust. Soc. Am. V97, 2181-2191, 1995.

Gerstoft, P, “SAGA user guide 5.0, an inversion software package”, SACKANT Undersea Research Centre, La Spezia, Italy, 1997

Goff, J., Austin, J. A., Christensen, B., and Turgut, A., “Chirp seismic reflection data on the New Jersey middle and outer shelf: The geologic response to 40,000 years of sea level change,” J. Acout. Soc. Am., V122, 2983, 2007.

Goldberg, DE, Genetic Algorithms in Search, *Optimization and Machine Learning* Addison-Wesley, Reading, MA, 1989.

Hamilton, E. L., “Geoacoustic Modeling of the Sea Floor”. J. Acout. Soc. Am., V68, 1313-1339, 1980.

Hamilton, E. L. and Bachman, R. T., “Sound velocity and related properties of marine sediments”, J. Acoust. Soc. Am. V72, 1891-1904, 1982.

Holmes, J. D., Carey, W. M., and Lynch, J. F., “Shallow-water waveguide characterization using an autonomous underwater vehicle-towed hydrophone array,” J. Acoust. Soc. Am. V119, 3346-3346, 2006.

Horn, R. A. and Johnson, C. R., *Matrix analysis*, pp. 169-176, Cambridge University Press, Cambridge, UK, 1991

Huang, C. F., Gerstoft P. and Hodgkiss, W. S., “Effect of ocean sound speed uncertainty on matched-field geoacoustic inversion,” J Acoust. Soc. Am, EL162-168, 2008.

Hursky, P., Kuperman W. A., and Hodgkiss W. S., “Extracting modal structure from vertical array ambient noise data in shallow water,” J. Acoust. Soc. Am. V98, 2971, 1995.

Hursky, P., Hodgkiss W. S. and Kuperman W. A., “Matched field processing with data-derived modes,” J. Acoust. Soc. Am. V109, 1355-1366, 2001.

Ingenito, F., “Measurement of mode attenuation coefficients in shallow water,” J. Acoust. Soc. Am. V53, 858-863, 1973.

Jackson, D. R. and Richardson, M. D., *High-Frequency Seafloor Acoustics*, Table 5.4 Springer, NY, 2006.

Jensen, F. B., Kuperman, W. A., Porter, M. B., Schmidt, H., *Computational Ocean Acoustics*, Springer-Verlag, NY, 2000.

Jones, D. L. and Baraniuk, R. G., "An adaptive optimal-kernal time-frequency representation", IEEE Transactions on Signal Processing, V43, NO.10, 2361-2371 ,1995. http://www-dsp.rice.edu/software/aok_doc.shtml

Katsnelson, B. G. and Petnikov, V. G., Shallow-Water Acoustics, Springer-Verlag, NY, 2002.

Knobles, D. P. and Koch, R. A. , "A time series of sound propagation in a strongly multipath shallow water environment with an adiabatic normal mode approach", Journal of Oceanic Engineering, V21, 1-13, 1996.

Knobles, D. P., Yudichak, T. W., Koch, R. A., Cable, P. G., Miller, J. H., and Potty, G. R., "Inferences on seabed acoustics in the East China Sea from distributed acoustic measurements," IEEE J. Ocean. Eng., V31, 129-144, 2006.

Knobles, D. P., Wilson, P. S., Goff, J. A., and Cho S. E., "Seabed acoustics of a sand ridge on the New Jersey continental shelf," J. Acoust. Soc. Am. V124, EL151-EL156, 2008.

Koch, R. A., Penland, C., Vidmar, P. J., and Hawker, K. E., "On the calculation of normal mode group velocity and attenuation," J. Acoust. Soc. Am. 73, 820-825, 1983.

Kuperman, W. A. and Ingenito, F., "Spatial correlation of surface generated noise in a stratified ocean," J. Acoust. Soc. Am. V67, 1988-1996, 1980.

Kuperman, W. A. and Lynch, J. F., "Shallow-Water Acoustics". Physics Today, V57(10), 55-61, 2004.

Leonotovich, M. A. and Fock, V. A., "Solution of the problem of propagation of electromagenetic waves along the earth's surface by the method of parabolic equation," J. Exp. Theor. Phys. V16, 557-573, 1946.

Li, F., and Zhang R. H., "Bottom sound speed and attenuation inverted by using pulsed waveform and transmission loss," Acta Acoustica, V25, 297-302, 2000.

Li, Q. X., Chen, C. H., Xu, J. S., *Marine atlas of the Bohai Sea, Yellow Sea and East China Sea: Geology and Geophysics Section* ,China Ocean Press, Beijing, 1991.

Li, Z. L., Zhang, R .H., Yan, J., Li, F. H., and Liu, J. J., "Geoacoustic inversion by matched-field processing combined with vertical reflection coefficients and vertical correlation," IEEE J. Ocean. Eng., V29, 973-979, 2004.

Lindsay, C. E. and Chapman, N. R., "Matched field inversion for geoacoustic model parameters using adaptive simulated annealing", IEEE Journal of Oceanic Engineering, V18, 224-231, 1993.

Marple, L., Brotherton, T., Lugo R., and Jones, D., "Travels through the time-frequency zone: advanced Doppler ultrasound processing techniques", in 27th Asilomar Conf. on Signals. Syst. And Computers, 2, 1469-1473, 1993.

Neilsen, T. B. "Normal mode Extraction and environmental inversion from underwater acoustic data," Ph.D. thesis, 2000.

Neilsen, T. B. and Westwood, E. K., "Extraction of acoustic normal mode depth functions using vertical line array data," J. Acoust. Soc. Am. V111, 748-756, 2002.

Newhall, A. E., Duda, T. F., Heydt, K., Irish, J. D., Kemp, J. N., Lerner, S. A., Liberatore, S. P., Lin, Y. T., Lynch, J. F., Maffei, A. R., Morozov, A. K., Shmelev, A., Sellers, C. J., and Witzell, W. E., "Acoustic and Oceanographic Observations and Configurations Information for the WHOI Moorings from the SW06 Experiment," Technical Report, WHOI, Woods Hole, MA, 2007.

Nevala, A. E., and Lippsett, L., "A 3-D underwater soundscape", Oceanus, V45, No.3, 2007

Niethammer, M., Jacobs, L. J., Qu, J. M., and Jarzynski, J., "Time-frequency representations of Lamb waves, " J. Acoust. Soc. Am. V109, 1841-1847, 2001.

Pekeris, C. L., "Theory of Propagation of Explosive Sound in Shallow Water". Geol., Soc. Am. Memo 27, 1948.

Peng, Z. H., Zhou, J. X., Dahl, P. H., and Zhang, R. H., "Sea-bed acoustic parameters from dispersion analysis and transmission loss in the East China Sea", IEEE Journal of Oceanic Engineering, V.29, NO.4, 1038-1045, 2004.

Pierce, A. D., "Extension of the method of normal modes to sound propagation in an almost-stratified mdedium," J. Acoust. Soc. Am., V37, 19-27, 1965.

Porter, M. B. and Reiss, E. L., "A numerical method for ocean acoustic normal modes," J. Acoust. Soc. Am., V76, 244-252, 1984.

Porter, M. B. "The KRAKEN Normal Mode Program," Naval Research Lab., Washington D. C., NRL/MR/5120-92-6920, 1992.

Potty, G. R., Miller, J. H., Lynch, J. F., and Smith, K. F., "Tomographic inversion for sediment parameters in shallow water", J. Acoust. Soc. Am., V108, 973-986, 2000.

Potty, G. R., Miller, J. H. and Lynch, J. F., "Inversion for sediment geoacoustic properties at the New England Bight", J. Acoust. Soc. Am. V114, 1874-1887, 2003 .

Rogers, P. H., Zhou, J. X., Zhang, X. Z., and Li, F., "Seabottom acoustic parameters from inversion of Yellow Sea experimental data," in *Experimental Acoustic Inversion Methods for Exploration of the Shallow Water Environment*, edited by A. Caiti, J-P Hermand, S. M. Jesus, and M. B. Porter, Kluwer Academic Dordrecht, pp. 219-234, 2000.

Rozenfeld, I., Carey, W. M., Cable, P. G., and Siegmann, W. L., "Modeling and analysis of sound transmission in the Strait of Korea," IEEE J. Ocean. Eng. V26, 809-820, 2001.

Sazontov, A. G., Matveyev, A. L., and Vdovicheva, N. K., "Acoustic Coherence in Shallow Water: Theory and Observation," IEEE J. Ocean. Eng. V27**,** 653-664, 2002.

Scholz, R., "Horizontal spatial coherence measurements with explosives and CW sources in shallow water," in *Aspects of Signal Processing*. Part I, ed., G. Tacconi, D. Reidel Publishing Co., Dordrecht-Holland, 95–108, 1977.

Shang, E. C., "Theory of horizontal coherence of a signal field in shallow water," Chi. Phys., V1, 490-493, 1981.

Siderius, M., Gerstoft, P., and Nielsen, P., "Broadband geoacoustic inversion from sparse data using genetic algorithms" J. Comput. Acoust. V6, 117–34, 1998

Smith, G. B., “Through the sensor environmental estimation,” J. Acoust. Soc. Am. V101, 3046, 1997.

Smith, P. W., "Spatial coherence in multipath or multimodal channels” J. Acoust. Soc. Am. V60, 305-310, 1976.

Stoll, R. D., “Acoustic waves in ocean sediments,” Geophysics, V42, 715-725, 1977.

Stoll, R. D., “Theoretical aspects of sound transmission in sediments,” J. Acout. Soc. Am., V68, 1341-1350, 1980.

Stoll, R. D., “Marine Sediment Acoustics” J. Acout. Soc. Am., V77, 1789-1799, 1985.

Stoll, R. D., “Comments on Boit model of sound propagation in water-saturated sand [JASA 97, 199-214 (1995)],” J. Acout. Soc. Am., V103, 2723-2725, 1998.

Tang, K. S., Man, K. F., Kwong, S., and He, Q., “Genetic Algorithms and their applications,” IEEE Signal Processing Magazine, 22-37,1996.

Tappert, F. D., “The parabolic approximation method,” in *Wave Propagation and Underwater Acoustics*, edited by J. B. Keller and J. S. Papadakis, Lecture Notes in Physics, V70, Springer, New York, 1977.

Taroudakis, M. I. and Markaki, M. G., “On the use of matched-field processing and hybrid algorithms for vertical slice tomography,” J. Acoust. Soc. Am., V102, 885-895, 1997.

Taroudakis, M. I. and Markaki, M. G., “Bottom geoacoustic inversion by ‘broadband’ matched field processing,” J. Comput. Acoust. V6, 167–83, 1998.

Taroudakis, M. I. and Markaki, M. G., “Bottom geoacoustic inversion by matched field processing-a sensitivity study,” *Inverse Problem* V16 1679–1692

Tattersall, J. M., Chizhik, D. B., Cole, F., and DiNapoli, F. R., “The effect of frequency-dependent bottom reflectivity on transmission loss in shallow water over a sandy bottom,” J. Acoust. Soc. Am., V93, 2395, 1993.

Tindle, C. T., “Attenuation parameters from normal mode measurements”, J. Acoust. Soc. Am., V71, 1145-1148, 1982.

Tolstoy, A. *Geoacoustic inversion using matched field processing*, 2002

Tolstoy, A. “Applications of match-field processing to inverse problems in underwater acoustics,” Inverse Problems, V16, 1655-1666, 2000

Turgut, A. and Yamamoto, T., “Measurements of acoustic wave velocities and attenuation in marine sediments,” J. Acoust. Soc. Am., V87, 2376-2383, 1990.

Urick, R. J. *Principles of Underwater Sound for Engineers*, McGraw-Hill, New York, 1983.

Vdovicheva, N. K., Matveev, A. L., and Sazontov, A. G., “Experimental and Theoretical Study of the vertical coherence of the sound Field in a Shallow Water,” Acoustical Physics, V48, 263-267, 2002.

Wan, L., Zhou, J. X., and Rogers, P. H., “Comparison of transmission loss data with predictions based on inverted seabed parameters from the Yellow Sea '96 experiment (A)”, J. Acoust. Soc. Am. V119, 3226, 2006.

Wan, L., Zhou, J. X., and Rogers, P. H., “Sound speed and attenuation in the sea bottom from broadband sound propagation in the Yellow Sea (A)”, J. Acoust. Soc. Am., V124, p. 2469, 2008.

Wan, L., Zhou, J. X., Rogers, P. H.,and Knobles, D. P., “Three-dimensional spatial coherence measurements: vertical, longitudinal/transverse horizontal coherence (A)”, J. Acoust. Soc. Am., V124, p. 2585, 2008.

Wan, L., Zhou, J. X., Rogers, P. H., and Knobles, D. P., "Spatial coherence measurements from two L-shape arrays in shallow water", Acoustical Physics, V55, p. 383-392, 2009.

Wan, L., Zhou, J. X., and Rogers, P. H., “Seabed sound speed and attenuation from broadband acoustic measurements in the Shallow Water 2006 experiment (A)”, J. Acoust. Soc. Am., V126, p. 2193, 2009.

Wan, L., Zhou, J. X., and Rogers, P. H., "Low frequency sound speed and attenuation in sandy seabottom from long-range broadband acoustic measurement", J. Acoust. Soc. Am., V128, 578-589, 2010.

Wang, Q. and Zhang, R. H., "Sound spatial correlations in shallow water," J. Acoust. Soc. Am. V92, 932-938, 1992.

Weston, D. E., "Intensity-range relation in oceanographic acoustics," J. Sound Vib. V18, 271-287, 1971.

Wille, P. and Thiele, R., "Transverse horizontal coherence of explosive signals in shallow water," J. Acoust. Soc. Am. V50(1pt.2), 348–353, 1971.

Williams, K. L., Jackson, D. R., Thorsos, E. I., Tang, D. J., and Schock, S. G., "Comparison of sound speed and attenuation measured in a sandy sediment to predictions based on the Biot theory of porous media, " IEEE J. Ocean. Eng., V27, 413-428, 2002.

Wolf, S. N., Cooper, D. K., and Orchard, B. J., "Environmentally adaptive signal processing in shallow water," Oceans '93, Vol (1), I-99-I-104, 1993.

Yang, J., *Spatial coherence in a shallow water waveguide.* Ph.D. thesis, Georgia Institute of Technology, Atlanta, GA, USA, 2007.

Zhang, R. H. and Jin, G. L., "Normal-mode theory of the average reverberation intensity in shallow water," J. Sound Vib., V119, 215-223, 1987.

Zhang, R. H. and Zhou, J. X., *Proceedings of International Conference on Shallow Water Acoustics,* China Ocean Press, Beijing, 1997.

Zhou, J. X., "Vertical coherence of sound field and boundary loss in shallow water," Chi. Phys., V1, 494-504, 1981.

Zhou, J. X., "Normal mode measurements and remote sensing of sea-bottom sound velocity and attenuation in shallow water," J. Acoust. Soc. Am. V78, 1003-1009, 1985.

Zhou, J. X., Zhang, X. Z., Rogers, P. H., and Jarzynski, J., “Geoacoustic parameters in a stratified sea bottom from shallow-water acoustic propagation,” J. Acoust. Soc. Am. V82, 2068-2074, 1987.

Zhou, J. X., Zhang, X. Z., Rogers, P. H., Simmen, J. A., Dahl, P. H., Jin, G. L., and Peng, Z. H., "Reverberation vertical coherence and sea-bottom geoacoustic inversion in shallow water," IEEE J. Ocean. Eng. V29, 988-999, 2004.

Zhou, J. X. and Zhang, X. Z., “Shallow water reverberation level: measurement technique and initial reference values,” IEEE J. Ocean. Eng. V30, 832-842, 2005.

Zhou, J. X., Zhang, X. Z., and Knobles, D. P., “Low-frequency geoacoustic model for the effective properties of sandy seabottoms,” J. Acoust. Soc. Am. V125, 2847-2866, 2009.

Zhu, R. and Guan, D., “Spatial horizontal coherence of sound in shallow water,” J. Acoust. Soc. Am. V92, 956–961, 1992.